2013

Complexity-driven properties of the intermetallic compounds $Gd_{117}Co_{56}Sn_{112}$ and $Ln_{30}Ru_4Sn_{31}$ (Ln = Gd and Tb)

Devin Charles Schmitt
Louisiana State University and Agricultural and Mechanical College, dschmi2@lsu.edu

COMPLEXITY-DRIVEN PROPERTIES OF THE INTERMETALLIC COMPOUNDS $Gd_{117}Co_{56}Sn_{112}$ AND $Ln_{30}Ru_4Sn_{31}$ (*Ln* = Gd AND Tb)

A Dissertation

Submitted to the Graduate Faculty of the
Louisiana State University and
Agricultural and Mechanical College
in partial fulfillment of the
requirements for the degree of
Doctor of Philosophy

in

The Department of Chemistry

by
Devin Charles Schmitt
B.S., Louisiana State University, 2006
May 2013

Acknowledgements

There are many people to whom I owe a great deal of thanks–people who have heavily contributed to my success as a graduate student, and who have contributed to my knowledge and understanding of solid state materials. The first of these people is my advisor, Prof. Julia Chan, who has assisted me from the beginning of my graduate career. She not only convinced me to begin graduate school, but she acted as a mentor both as a scientist and as a writer. I would certainly not be soon graduating with my Doctor of Philosophy without the mentorship of Prof. Chan.

I have had the privilege of working with excellent collaborators and mentors at Louisiana State University. Profs. David Young, Shane Stadler, and Rongying Jin have all greatly helped with my growth as a scientist. They have gone above and beyond what was necessary for collaborators to answer inquiries and explain to me, to the very best of their abilities, the nature of the properties of materials in the solid state. In particular, I have to admire Profs. Young and Stadler for having the courage to allow me full access to measure physical properties on their *very* expensive instruments, and I would like to thank them for the learning opportunity that performing these measurements has afforded.

I would like to thank Prof. George Stanley for helping with my scientific advancement and providing the energy necessary to work at the end of the week (Friday donuts). Dr. Frank Fronczek deserves special thanks, as his guidance, patience, and knowledge facilitated my understanding of crystallography. Gregory Morrison, Bradford Fulfer, Dr. William Phelan, Dr. Gregory McCandless, and Dr. Melissa Menard should be mentioned for their help with editing manuscripts and for general scientific banter. A special thanks also goes to Joseph

Prestigiacomo, since without his collaborative help, I doubt we would have discovered the spin-glass pulse memory effect described in this dissertation.

Finally, I would like to thank my wife, Carolyn, for her support throughout my graduate career, and my two daughters, Kennedy and Penelope, for inspiring me to work harder with more diligence. Exhaustively acknowledging everyone who has helped me in my graduate career or up to this point would require an entire dissertation, so to everyone who has helped me in any way and has not been acknowledged in the aforementioned text, I extend my deepest thanks and appreciation.

Table of Contents

Abstract

Understanding the relationships between the structure of materials and their properties in extended solid systems is a necessity when intuitively designing functional materials. One of the most fundamental properties of a material is its ability to transport heat, which is linked to the lattice complexity of the material. Here, the single crystalline materials $Gd_{117}Co_{56}Sn_{112}$ and $Tb_{30}Ru_4Sn_{31}$ are grown to study the pronounced effect of a complexity-driven reduction of lattice thermal conductivity. The transport and magnetic properties of $Gd_{117}Co_{56}Sn_{112}$ and $Ln_{30}Ru_4Sn_{31}$ (*Ln* = Gd and Tb) are also presented and related to other systems. $Tb_{30}Ru_4Sn_{31}$ is found to be a large magnitude and highly anisotropic spin-glass system with an estimated glassy component comparable to spin-ice systems. It is found that temperature-specific memory effects of the large glassy component can be stored through magnetic field pulses and recovered with very low volatility, creating a potential new application for spin-glasses as functional materials.

Chapter 1. Introduction

1.1 Introduction

Understanding the relationships between the structure of materials and their properties in extended solid systems is a necessity when intuitively designing functional materials. This includes fields such as materials for energy applications, hard materials, and information technology-related materials.[1.1] One of the most fundamental properties of a material is ability to transport heat, thermal conductivity, and this property is linked to the lattice complexity of the material. Herein, the primary focus is to study the effect of lattice complexity on thermal conductivity and other intrinsic properties of extended solid system such as, but not limited to, electrical resistivity, thermopower, and magnetic properties.

The initial goal of the research presented herein was to search for materials with intrinsically low lattice thermal conductivity for potential use in thermoelectric applications. A thermoelectric material's performance is measured by a dimensionless quantity (zT) known as the thermoelectric figure of merit. The figure of merit is defined as $zT = S^2T/(\rho\kappa)$, where S is the Seebeck coefficient, T is the operating temperature, ρ is the electrical resistivity, and κ is the thermal conductivity. Additionally, the κ can be subdivided into a lattice contribution, κ_L, and an electronic contribution, κ_e. It is clear from the above equation that thermal conductivity should be considered a parasitic value in thermoelectrics. The typical paradigm for designing thermoelectric materials is to search for materials with high S, then to optimize the materials' ρ and κ_L. This methodology leads to diminishing returns in overall thermoelectric efficiencies, as the two most common methods used to reduce κ_L are (1) to introduce atomic disorder and (2) to introduce a large number of grain boundaries (nanostructuring); however, both methods tend to increase ρ. In fact, the maximum obtainable zT of thermoelectric materials has only increased by

a factor of ~3[1.2] since the 1970's when the exceptional thermoelectric properties of Bi_2Te_3 (zT ~ 0.8)[1.3] were first discovered, and an estimated zT of 4 is necessary for thermoelectrics to be competitive with current technologies,[1.4] suggesting that a different design approach is needed to further optimize the technology. Finding materials that exhibit intrinsically low lattice thermal conductivity concomitant with relatively low ρ, would change the paradigm to require the optimization of only S and may provide the change necessary to achieve the goal of a $zT > 4$.

It has been shown that thermal conductivity can be reduced using materials with large, complex unit cells that contain heavy atoms. A more detailed explanation of these phenomena can be found in the introduction to Chapter 2. A complex many-atom-containing unit cell can lower the ratio of phonon vibrational modes that carry heat efficiently as $1/V_P$, where V_P is the volume of the the primitive unit cell.[1.5, 6] $Yb_{14}MnSb_{11}$ is a prime example of a heavy atom containing large unit cell compound.[1.7, 8] This high temperature thermoelectric compound is comprised of a tetragonal unit cell (V_P ~ 3000 Å^3)[1.7] with a remarkably low thermal conductivity of ~0.7 W/m-K at room temperature and a zT_{max} of ~1.0 at ~1200 K.[1.8] Thus, the following criteria for selecting a system were set: (1) the system should have a large primitive unit cell volume (V_P > 5000 Å^3) (2) the system should contain heavy atoms (3) the system should not have been fully characterized. In addition to the previous requirements single crystals of the targeted system must be produced in order to ensure measurement of intrinsic lattice thermal conductivity. The $Dy_{117}Co_{57}Sn_{112}$ structure type[1.9] met the abovementioned criteria and the Gd analogue was selected since it had not been previously reported.

A logical step in the synthesis of single crystalline materials is to employ the flux growth method using a low melting and readily available main group element, such as Ga or Sn as an incorporative flux.[1.10, 11] In the case of $Gd_{117}Co_{56}Sn_{112}$, and later $Ln_{30}Ru_4Sn_{31}$ (Ln = Gd–Dy), the use of a Sn flux produced single crystals of binary and ternary Sn-rich compounds. It was

known that the $Dy_{117}Co_{57}Sn_{112}$ structure-type formed in melts near stoichiometry and was the high-temperature thermodynamically stable product, since polycrystalline products formed readily via arc-melting on stoichiometry.[1.9, 12, 13] A different flux growth strategy was necessary, which allowed for both a molten flux for rapid diffusion to facilitate single crystal growth and a higher *Ln* starting content to stabilize the $Dy_{117}Co_{57}Sn_{112}$ structure-type over more Sn-rich phases. Several *Ln*-*M*, where *Ln* is a lanthanide and *M* is Co, Fe or Ru, with eutectic points < 1000 °C occur at an approximate *Ln*:*M* ratio of 2:1. Thus, to access these high *Ln*-containing phases, a starting molar ratio of approximately 2:1:2 (*Ln*:*M*:Sn) was utilized in order to provide a molten growth median at temperatures accessible using typical high-temperature laboratory furnaces.

Once $Gd_{117}Co_{56}Sn_{112}$ had been grown and fully characterized, attempts were made to grow single crystals of the Ru analogue using the same synthetic conditions, since *Ln*-Fe-Ge (*Ln* = Gd–Tm) analogues with a similar structure-type had been reported.[1.14, 15] However, $Ln_{30}Ru_{4+x}Sn_{31-y}$ (*Ln* = Gd–Dy) forms, which adopts a new structure-type in the orthorhombic space group *Pnnm*. Though $Ln_{30}Ru_{4+x}Sn_{31-y}$ has a primitive unit cell volume (V_P) of approximately half the V_P of $Gd_{117}Co_{56}Sn_{112}$, it contains more overall atomic positions and, in particular, more unique *Ln* atomic sites. Additionally, the structure contains local structural perturbations, caused by the presence or absence of a partially occupied Ru atomic site, which has been modeled in two discrete orientations.

Anisotropic properties of intermetallic materials are not typically studied, since high quality, sizeable single crystals are necessary for these measurements. This precludes the use of popular polycrystalline synthetic methods such as arc-melting and ball milling. Single crystals must also be oriented along crystallographic directions using, for example, Laue diffraction before anisotropic physical property measurements can be performed. Moreover, the

macroscopic geometry of the crystals is important in transport property measurements that require absolute magnitudes, such as electrical resistivity, thermopower, and thermal conductivity. Thus, measurement of a well-shaped three dimensional (3-D) crystal, such as a polished bar, is ideal, while lower-dimensional crystal shapes, such as needles and plates, can introduce significant experimental error when measuring along the short axis. Anisotropic magnetic properties, however, are more common, as the macroscopic crystal shape typically has a less pronounced effect on experimental error. The orthorhombic symmetry $Tb_{30}Ru_4Sn_{31}$ enabled the potential for anisotropic physical property behavior which is described in detail in Chapter 3.

Magnetic interactions in crystalline materials can be divided into three broad categories: 1) A non-ordered state, or paramagnetic state, that displays temperature and field-dependence of the magnetization. Paramagnetic spin states change randomly as a function of time, i.e. the spin states at two different times will likely exhibit two completely different configurations.[1.16] 2) A long range ordered magnetic state, such as ferromagnetism and antiferromagnetism, which displays periodic long range ordering of magnetic spins below a specific temperature, or energy, scale. Above the ordering transition temperature, the thermal energy present in the system is sufficient to overcome the magnetic ground state energy of the system, and the spins are again randomized (paramagnetic state).[1.16] 3) In some systems, short range magnetic ordering is more energetically favorable than a long range ordered state. The dominance of short range magnetic ordering has been previously reported to occur from either geometric structural considerations or through atomic disorder.[1.17, 18] The very nature of short range magnetic ordering causes these systems to enter a state of greatly slowed spin dynamics, analogous to the slow atomic mobility of a macroscopic glass, below a specified energy scale known as the glass transition

temperature.[1.19] Because of the slowed spin dynamics, extended solid materials exhibiting dominant short range magnetic ordering are often referred to as spin-glasses.

Spin-glass materials have been a field of intense research over the past several decades, as they behave as non-equilibrium systems below the glassy transition temperature, leading to a multitude of exotic properties including isothermal time-dependent relaxation[1.20] and frequency-dependent spin dynamics.[1.21] Though efforts have been made to exploit the non-equilibrium dynamics to store up to 8-bits of information on a single crystalline spin-glass system, the slow dynamics of these systems have precluded them from being classified as functional materials. Through careful examination of heat capacity and time-dependent magnetization, $Tb_{30}Ru_4Sn_{31}$ was found to be a spin-glass material with a very large spin-glass component below ~17 K of > 1700 emu/mol-Tb.[1.22] In Chapter 4, we find that temperature-specific memory effects of $Tb_{30}Ru_4Sn_{31}$ can be quickly stored through magnetic field pulses while cooling the sample. The imprinted memory is then recoverable upon warming, with very low imprinted memory degradation over time, creating a potential new application for spin-glasses as functional materials.

This introduction was intended to provide an overview of the methodologies, thought processes, and general theoretical concepts used for determining the directions of the research described in the following chapters. As such, it was my intention to chronologically reflect on the reasoning that lead to the discoveries of the materials and properties presented herein. The introductions to Chapters 2, 3 and 4 should be referenced for a more detailed structural description of the materials and theoretical understanding of the observed properties thereof.

1.2 References

1.1. *Frontiers in crystalline matter: from discovery to technology*. The National Academies Press: Washington, D.C., 2009.

1.2. Hsu, K. F.; Loo, S.; Guo, F.; Chen, W.; Dyck, J. S.; Uher, C.; Hogan, T.; Polychroniadis, E. K.; Kanatzidis, M. G., *Science* **2004,** *303*, 818-821.

1.3. Imamuddin, M.; Dupre, A., *Phys. Status Solidi A-Appl. Res.* **1972,** *10*, 415-424.

1.4. Mahan, G. D.; Sofo, J. O., *Proc. Natl. Acad. Sci. U. S. A.* **1996,** *93*, 7436-7439.

1.5. DiSalvo, F. J., *Science* **1999,** *285*, 703-706.

1.6. Tritt, T. M., *Thermal Conductivity Theory, Properties and Applications*. Kluwer Academic: New York, 2004; p 290.

1.7. Chan, J. Y.; Olmstead, M. M.; Kauzlarich, S. M.; Webb, D. J., *Chem. Mater.* **1998,** *10*, 3583-3588.

1.8. Brown, S. R.; Kauzlarich, S. M.; Gascoin, F.; Snyder, G. J., *Chem. Mater.* **2006,** *18*, 1873-1877.

1.9. Salamakha, P.; Sologub, O.; Bocelli, G.; Otani, S.; Takabatake, T., *J. Alloys Comp.* **2001,** *314*, 177-180.

1.10. Canfield, P. C.; Fisk, Z., *Philos. Mag. B* **1992,** *65*, 1117-1123.

1.11. Kanatzidis, M. G.; Pöttgen, R.; Jeitschko, W., *Angew. Chem., Int. Ed.* **2005,** *44*, 6996-7023.

1.12. Cirafici, S.; Canepa, F.; Manfrinetti, P.; Napoletano, M., *J. Alloys Comp.* **2001,** *317-318*, 550-555.

1.13. He, W.; Zhang, J. L.; Yan, J. L.; Fu, Y. C.; Zeng, L. M., *J. Alloys Comp.* **2010,** *491*, 49-52.

1.14. Pecharsky, V. K.; Bodak, O. I.; Belsky, V. K.; Starodub, P. K.; Mokra, I. R.; Gladyshevskii, E. I., *Kristallografiya* **1987,** *32*, 334-338.

1.15. Morozkin, A. V.; Seropegin, Y. D.; Portnoy, V. K.; Sviridov, I. A.; Leonov, A. V., *Mater. Res. Bull.* **1998,** *33*, 903-908.

1.16. Anthony, R. W., *Basic Solid State Chemistry*. 2 ed.; John Wiley and Sons, Ltd.: Chichester, 2008; p 480.

1.17. Ramirez, A. P., *Annu. Rev. Mater. Sci.* **1994,** *24*, 453-480.

1.18. Moessner, R.; Ramirez, A. R., *Physics Today* **2006,** *59*, 24-29.

1.19. Bouchaud, J. P.; Dupuis, V.; Hammann, J.; Vincent, E., *Phys. Rev. B* **2002,** *65*, 1-11.

1.20. Chamberlin, R. V.; Mozurkewich, G.; Orbach, R., *Phys. Rev. Lett.* **1984,** *52*, 867-870.

1.21. Tholence, J. L., *Solid State Commun.* **1980,** *35*, 113-117.

1.22. Prestigiacomo, J.; Schmitt, D. C.; Chan, J. Y.; Young, D. P.; Stadler, S.; Adams, P. W., Observation of a giant spin-glass effect in $Tb_{30}Ru_4Sn_{31}$. Louisiana State University: Baton Rouge, 2013.

Chapter 2.[†] Probing the Lower Limit of Lattice Thermal Conductivity in an Ordered Extended Solid: $Gd_{117}Co_{56}Sn_{112}$ – A Phonon Glass-Electron Crystal System

2.1 Introduction

One of the most fundamental properties of a solid is its thermal conductivity – a measure of a material's ability to transfer heat. The discovery of novel materials with low thermal conductivity is paramount to improving the efficiency of thermoelectric devices.[2.1-3] The structural complexity of a material is fundamentally linked to its lattice thermal conductivity – a correlation which is well documented both theoretically[2.4] and experimentally.[2.5] Thus, exploring materials with high structural complexity provides an avenue for discovering materials with intrinsically low thermal conductivity. Here we present the structure, transport, and magnetic properties of single crystal $Gd_{117}Co_{56}Sn_{112}$, a complex material with a primitive unit cell volume of ~ 6,858 $Å^3$ and ~ 285 atoms per primitive unit cell (1,140 atoms per face-centered cubic unit cell). Since $Gd_{117}Co_{56}Sn_{112}$ is one of the most structurally complex extended solids known, we use the material to probe the limit of lattice thermal conductivity in a non-glassy material with the expectation of glass-like thermal conductivity. Indeed, the room temperature lattice thermal conductivity of this material represents one of the lowest ever reported for a bulk solid. Furthermore, single crystal $Gd_{117}Co_{56}Sn_{112}$ exhibits low electrical resistivity at room temperature. The concomitant low electrical resistivity and exceptionally low lattice thermal conductivity represents a true physical system that approaches the ideal phonon glass–electron crystal.

The total thermal conductivity of a material, κ_T, can be separated into a lattice contribution, κ_L, and an electronic contribution, κ_e, where $\kappa_T = \kappa_L + \kappa_e$. κ_e is often less than 1

[†]Reproduced with permission from Schmitt, D. C.; Haldolaarachchige, N.; Xiong, Y. M.;Young, D. P.; Jin, R. Y.; Chan, J. Y., *J. Am. Chem. Soc.* **2012,** *134*, 5965-5973. Copyright 2012 American Chemical Society.

W/(m·K) in good thermoelectric materials (semiconductors) due to relatively low optimal carrier concentrations.[2.1] κ_L is considered a parasitic parameter in a thermoelectric material, where the dimensionless figure of merit, $ZT = S^2T/[\rho(\kappa_e + \kappa_L)]$, is to be maximized. Here, S is the Seebeck coefficient (μV/K), ρ is the electrical resistivity (Ω·cm), and T is the temperature.[2.1] Furthermore, since the figure of merit is inversely proportional to both ρ and κ; the ideal candidate for a thermoelectric material must exhibit low thermal transfer properties like a glass and simultaneously the electronic properties of a crystalline solid at its operating temperature. A material exhibiting this unusual set of properties was termed a "phonon glass–electron crystal" (PGEC) by Slack.[2.6] A relationship between κ_e and ρ is given by the Wiedemann-Franz Law, $\kappa_e = L_oT/\rho$, where $L_o = 2.45 \times 10^{-8}$ W·Ω/K^2 is the Lorentz number. Substituting this into the figure of merit leads to $ZT = S^2/[L_o(1+\kappa_L/\kappa_e)]$. Notably, as κ_L/κ_e approaches zero, the Seebeck coefficient becomes the only contributing factor in determining ZT.

Although amorphous and glassy materials often have very low thermal conductivities, their electrical resistivities are too large to be useful for thermoelectric applications; thus, the focus here is to discover *ordered* crystalline structures that have very low *intrinsic* lattice thermal conductivity. In crystalline systems, such as Zn_4Sb_3,[2.7] TAGS $[(GeTe)_x(AgSbTe_2)_{100-x}]$,[2.8] and the LAST $(AgPb_mSbTe_{2+m})$[2.9] compounds, their thermal transport is highly dependent on varying degrees of disorder.[2.3] The aforementioned materials exhibit glass-like thermal conductivity stemming from partially amorphous structures (Zn_4Sb_3) or substitutional disorder. While these systems often possess a large Seebeck coefficient, they are likely close to the upper limit of their figure of merit values. The challenge with this "extrinsically complex" model is that the lattice imperfections that effectively scatter thermally conducting phonons also scatter charge carriers. Thus, charge carriers in these systems have relatively low mobilities, resulting in an overall high

magnitude of the electrical resistivity relative to semiconductors with similar carrier concentrations. Doping to higher carrier concentrations (n) would, of course, decrease electrical resistivity, but the carrier mobility also suffers further from increased carrier-carrier scattering. The thermopower would also likely decline, as the ambipolar Seebeck coefficient term is inversely proportional to n.[2.1]

There are three ways to intrinsically reduce the thermal conductivity of a lattice: (1) increase lattice complexity, (2) introduce a non-homogenous harmonic oscillator (a "rattler" atom), and (3) use atoms with a high average atomic mass such as Sn, Te, Yb, Bi, etc. Here we focus on (1) and (3). A complex many-atom unit cell can scatter phonons that carry heat efficiently by a factor of $1/N$, where N is the number of atoms in the primitive unit cell, effectively lowering κ_L.[2.5, 10] With its complex structure containing 285 atoms in the primitive cell, and high atomic mass elements, $Gd_{117}Co_{56}Sn_{112}$ is a promising candidate as an intrinsically low lattice thermal conductivity material.

2.2 Experimental

2.2.1 Synthesis

Starting materials for the preparation of $Gd_{117}Co_{56}Sn_{112}$ were ingots of Gd, Co powder, and Sn shot (all > 99.9 weight % purity, metal basis) and were used as received. Gd, Co, and Sn were loaded (in desired molar ratios discussed below) into an alumina crucible and sealed in an evacuated (~ 1.2×10^{-3} atm) fused silica tube. In growth attempts that exceeded 1200 °C, the tube was filled with ~ 0.2 atm of Ar to prevent silica tube collapse. The initial synthesis employed heating a molar ratio of 2:1:2 (Gd:Co:Sn) to 1200 °C for 8 h, slow-cooling to 1075 °C at 4 °C/h, followed by fast-cooling at 150 °C/h, which lead to a minority formation of $Gd_{117}Co_{56}Sn_{112}$, with majority formation of $GdCoSn_2$ with the $CeNiSi_2$ structure-type.[2.11] The

use of silica wool in attempts to spin the sample resulted in silicon incorporation in the sample, and the exclusive formation of the $GdCo(Sn,Si)_2$ with the $CeNiSi_2$ structure type.[2.11] The highest yield of phase pure $Gd_{117}Co_{56}Sn_{112}$ was achieved by heating a molar ratio of 12:6:11 (Gd:Co:Sn) to 1260 °C, slow-cooling at 1 °C/h to 1200 °C, followed by faster-cooling at 5 °C/h to 1065 °C. The sample was then removed from the oven and allowed to cool to room temperature. Attempts to flux grow $Gd_{117}Co_{56}Sn_{112}$ using a higher Sn:Gd ratio resulted in the exclusive formation of $GdCoSn_2$. This is similar to the appearance of $GdCoSn_2$ when increasing the Sn content (above 44:16:40 of Gd:Co:Sn) in the Gd–Co–Sn ternary phase diagram.[2.12] $Gd_{117}Co_{56}Sn_{112}$ yields increased significantly as both the maximum dwell temperature and the length of time spent above 1200 °C were increased. $Gd_{117}Co_{56}Sn_{112}$ is highly reactive to both HCl and HNO_3; thus, mechanical extraction was necessary to separate the three different flux free crystal morphologies listed below. The $Gd_{117}Co_{56}Sn_{112}$ phase has a markedly different color, very dark grey polyhedrals, as opposed to $GdCoSn_2$, which forms silvery plate-like crystals.[2.11] A third phase, polycrystalline CoAl, was identified through powder X-ray diffraction and formed a thin layer between the sample and alumina crucible. Our experiments show that high temperatures and approximate equimolar Gd:Sn ratios are required to form the $Gd_{117}Co_{56}Sn_{112}$ phase as opposed to the $GdCoSn_2$ phase.

2.2.2 Elemental Analysis

Elemental analysis was performed by two techniques: (1) energy dispersive spectroscopy (EDS) using a standard-free JEOL JSM-5060 scanning electron microscope (SEM) with an accelerating voltage of 15 keV and a crystal-to-detector distance of 20 mm and (2) inductive plasma coupled optical emission spectroscopy (ICP-OES), using a Perkin Elmer Optima 5300 DV with elemental Gd, Co, and Sn as internal standards. Using an average of 12 scans at

different locations on the crystal, stoichiometry of the sample as determined by EDS was $Gd_{117(10)}Co_{45(10)}Sn_{107(10)}$, and by ICP-OES determined stoichiometry as $Gd_{117(3)}Co_{48(3)}Sn_{111(3)}$. Error bars were determined by summing a fixed 3 atomic % instrumental error and the standard deviations of the data collected for the EDS stoichiometry and using a fixed 1 atomic % for the ICP-OES stoichiometry.

2.2.3 X-ray Diffraction

Powder X-ray diffraction was performed to determine phase homogeneity and purity using a Bruker D8 Advance X-ray diffractometer with monochromatic Cu $K_{\alpha 1}$ radiation with λ = 1.540562 Å ($2\theta_{max}$ = 80 °). A single crystal fragment of $Gd_{117}Co_{56}Sn_{112}$ was cleaved to approximate dimensions of 0.03 × 0.08 × 0.08 mm^3 and mounted on a glass fiber using epoxy. Single crystal X-ray diffraction was performed using a Nonius Kappa CCD X-ray diffractometer equipped with a graphite monochromator and Mo K_α radiation (λ = 0.71073 Å). Diffraction data were collected at room temperature up to θ = 30.0 °. Absorption corrections were carried out using multi-scan methods based on

Table 2.1. Crystallographic Parameters for $Gd_{117}Co_{56}Sn_{112}$

Formula	$Gd_{117}Co_{56.3(1)}Sn_{111.5(1)}$
Crystal System	Cubic
Space Group	$Fm\bar{3}m$
a (Å)	30.159(3)
V (Å^3)	27432(5)
Z	4
Crystal dimensions (mm^3)	0.03 x 0.05 x 0.05
Temperature (K)	298(2)
θ range (º)	3.51 - 29.99
μ (mm^{-1})	41.036
Data Collection	
Measured Reflections	96152
Unique Reflections	2013
Reflections with I>2σ(I)	1637
R_{int}	0.0495
h	-42 to 42
k	-29 to 30
l	-28 to 28
Refinement	
$\Delta\rho_{max}$ (eÅ^{-3})/$\Delta\rho_{min}$ (eÅ^{-3})	3.778 / -3.371
GoF	1.492
Extinction coefficient	0.0000006(1)
Reflections/Parameters	2013 / 101
R_1 ($F^2 > 2\sigma F^2$) [a]	0.0318
wR_2 (F^2) [b]	0.0548

[a] $R_1 \sum[|F_o| - |F_c|]/\sum|F_o|$.

[b] $wR_2 = [\sum[w(F - F_c^2)]/\sum[w(F_o^2)^2]]^{1/2}$.

highly redundant data.[2.13] Crystallographic parameters are provided in Table 2.1. Direct methods were used to solve the crystal structure using SIR2002[2.14] and refinement was conducted in SHELXL97.[2.15] Intensity statistics suggested that the space group was centrosymmetric. Systematic absences indicated space groups $Fm\bar{3}m$ and $Fm\bar{3}$, and the final model solution was obtained in $Fm\bar{3}m$. The refined stoichiometry of the crystallographic model is $Gd_{117}Co_{56.3(1)}Sn_{111.5(1)}$, but for simplicity we refer to the stoichiometry as $Gd_{117}Co_{56}Sn_{112}$. Atomic parameters for $Gd_{117}Co_{56}Sn_{112}$ can be found in Table 2.2.

Table 2.2. Atomic positions of $Gd_{117}Co_{56}Sn_{112}$

Atom	Site	*x*	*y*	*z*	Occ.	U_{eq} (Å^2) [a]
Gd1	96*k*	0.067788(14)	0.067788(14)	0.15507(2)	1	0.00966(13)
Gd2	96*k*	0.179230(14)	0.179230(14)	0.40586(2)	1	0.00952(13)
Gd3	96*k*	0.200403(13)	0.200403(13)	0.067189(19)	1	0.00763(13)
Gd4	96*j*	0.253620(19)	0.105016(19)	0	1	0.00806(13)
Gd5	48*i*	0.11773(18)	0.11773(18)	1/2	0.59(3)	0.0080(3)
Gd5’	48*i*	0.1243(2)	0.1243(2)	1/2	0.41(3)	0.0080(3)
Gd6	24*e*	0.3486(2)	0	0	0.555(14)	0.0093(4)
Gd6’	24*e*	0.3356(3)	0	0	0.445(14)	0.0093(4)
Gd7	8*c*	1/4	1/4	1/4	1	0.0085(4)
Gd8	4*a*	0	0	0	1	0.0113(6)
Co1	96*k*	0.16926(4)	0.16926(4)	0.23133(5)	1	0.0099(3)
Co2	96*k*	0.07970(7)	0.07970(7)	0.01525(10)	0.5	0.0107(7)
Co3	32*f*	0.39274(7)	0.39274(7)	0.39274(7)	1	0.0213(7)
Co4	32*f*	0.30774(5)	0.30774(5)	0.30774(5)	1	0.0055(5)
Co5	24*e*	0.4845(9)	0	0	0.088(7)	0.01 [b]
Co6	32*f*	0.05714(12)	0.05714(12)	0.05714(12)	0.417(12)	0.005(2)
Co7	24*e*	0.4223(14)	0	0	0.076(8)	0.01 [b]
Sn1	96*k*	0.072852(19)	0.072852(19)	0.32321(3)	1	0.00783(17)
Sn2	96*k*	0.108378(18)	0.108378(18)	0.24026(3)	1	0.00823(17)
Sn3	48*i*	0.20865(3)	0.20865(3)	1/2	1	0.0101(2)
Sn4	48*h*	0.14535(3)	0.14535(3)	0	1	0.0073(2)
Sn5	48*g*	1/4	1/4	0.14087(4)	1	0.0078(2)
Sn6	32*f*	0.14657(3)	0.14657(3)	0.14657(3)	1	0.0090(3)
Sn7	24*e*	0.10880(6)	0	0	0.917(7)	0.0085(6)
Sn8	24*e*	0.21581(5)	0	0	1	0.0100(3)
Sn9	32*f*	0.4462(3)	0.4462(3)	0.4462(3)	0.89(5)	0.0281(14)
Sn9’	32*f*	0.4374(15)	0.4374(15)	0.4374(15)	0.11(5)	0.0281(14)

[a] U_{eq} is defined as $^1/_3$ of the trace of the orthogonalized U_{ij} tensor.
[b] Atomic displacement parameters fixed for final refinement.

2.2.4 Physical Properties

Physical properties were performed on a large single crystal fragment polished to a bar with dimensions of 1.22 × 1.05 × 1.98 mm^3. Magnetic measurements were conducted using a Quantum Design Physical Property Measurement System (PPMS). Temperature dependent electrical resistivity was measured using a standard four-probe dc-technique using the PPMS. The thermal conductivity and Seebeck coefficient were measured in the PPMS using the thermal transport option. Heat capacity and Hall resistivity were measured using the PPMS heat capacity option and Van der Pauw method, respectively. The Seebeck coefficient was also independently measured using a comparative technique to a constantan standard on an MMR Technologies sample stage.

2.3 Results and Discussion

2.3.1 Structure

$Gd_{117}Co_{56}Sn_{112}$ is isostructural to $Dy_{117}Co_{57}Sn_{112}$[2.16] and exhibits a very complex crystal structure with 24 atomic positions in the asymmetric unit, positional atomic disorder (Table 2.2), and 1,140 atoms in the face-centered cubic (FCC) unit cell (a = 30.159(3) Å). The crystal structure is similar to the $Tb_{117}Fe_{52}Ge_{112}$ structure type,[2.17] which is adopted for Ln = Gd and Dy–Tm for the Fe analogues and $Sm_{117}Cr_{52}Ge_{112}$.[2.18] The $Dy_{117}Co_{57}Sn_{112}$ structure has been reported for Ln = Ce,[2.19] Pr,[2.20] Sm,[2.21] and Gd–Dy,[2.12, 21] as well as a Nd-Ru-Sn analogue.[2.22] Recently, a full topological structural description was reported for $Sm_{117}Co_{55.6}Sn_{116}$.[2.21] Our structural model is similar to that of Ref. [2.21], which uses a multishell approach for the description of $Sm_{117}Co_{55.6}Sn_{116}$. We have chosen to examine an alternate structural model with the recognition of a Co/Sn bonding framework *and* Sn-centered $Sn@Gd_8/Gd_6$ polyhedra, which

are similar to structural motifs found in La_4Ge_3 and $Ca_{31}Sn_{20}$.[2.23, 24] For a more detailed description of modeled disorder, see Ref. [2.21].

The crystal structure of $Gd_{117}Co_{56}Sn_{112}$ is composed of several different structural units consisting of bonded Co—Sn, Sn—Sn, and Co—Co units (Figure 2.1a), as well as Sn-centered polar units (Figure 2.1b). The structural units are conveniently described with respect to Co5, Gd7, and Gd8 with polar units centered at Sn3, Sn4, Sn6, and Sn8 (Figure 2.2). The Sn-centered units form $Sn@Gd_8/Gd_6$ polyhedra surrounding and connecting the FCC arrangement of Gd8 centered structural units. Co5- and Gd7-centered structural units occupy the octahedral and tetrahedral sites of the FCC structure, respectively. Figure 2.1c shows the single crystal X-ray diffraction pattern for a single crystal of $Gd_{117}Co_{56}Sn_{112}$. The sharpness of the spots in the diffraction pattern indicates long range order with crystalline periodicity.

Figure 2.2a shows the Sn3-centered unit, which is coordinated to a bicapped trigonal prism of Gd atoms, $Sn3@Gd_8$, with 4 x Gd3, 2 x Gd2, and 2 x Gd4 atoms at 3.419(1) Å, 3.104(1) Å, and 3.326(1) Å, respectively. Two Sn3-centered units share faces by 4 common Gd3 atoms. The Sn4-centered unit (Figure 2.2b) is coordinated to a bicapped trigonal prism of Gd atoms, Sn4@Gd8, with 2 x Gd3 atoms, 4 x Gd1 atoms, and 2 x Gd4 at 3.101(1) Å 3.121(1) Å and 3.484(1), respectively. The Sn6-centered unit (Figure 2.2c) is coordinated to a highly distorted trigonal antiprismatic environment axially capped by a $Co1_3$ trigonal unit (*vide infra*) with 3 x Gd3 atoms at 3.317(1) Å and 3 x Gd1 atoms at 3.370(1) Å. The centroid of the $Co1_3$ trigonal unit lies at only ~ 2.27 Å from Sn6. The Sn8-centered unit (Figure 2.2d) is coordinated to 4 x Gd4 atoms at 3.366(1) Å and 4 x Gd8 atoms at 3.423(1) Å in a rectangular antiprismatic arrangement. The Sn3, Sn4, Sn6, and Sn8 coordination environments compare well with the

Ge^{4-} isolated anions in the Zintl phase La_4Ge_3, where Ge is coordinated by 8 La atoms, four at 3.057(2) Å and four at 3.437(5) Å.[2.23]

The Gd7-centered structural unit, as shown in Figure 2.3a, consists of an inner cage and an outer tetrahedral coordination of peripheral Co—Sn and Sn—Sn bonded atoms. The inner cage is built of an octahedral coordination of Sn5 atoms and a tetrahedral coordination Co4 atoms and $Co1_3$ trigonal units with Co—Co distances of 2.647(2) Å. Each Co4 atom is bonded to three Co1 atoms at 2.505(2) Å, and each Sn5 atom is bonded to four Co1 atoms at 2.642(2) Å. These values are close to the sum of the covalent radii of Co–Co (2.52 Å) and Co–Sn (2.67 Å).[2.25] The total inner cage coordination is $Gd7@Sn_6Co_{16}$. The inner cages and peripheral atoms are bridged by Co1 and Sn2 atoms with a Co—Sn distances of 2.611(2) Å. The Co—Sn and Sn—Sn network bonded to the peripheral of the inner cage is composed of Sn1, Sn2 and Co3 atoms bonded about the inner cage with tetrahedral symmetry. The arrangement and related bond distances of the atoms are shown in Figure 2.3a. Each tetrahedral coordination of peripherally linked atoms is made up of three arms extending off a central Co3. The arms consist of an outermost Co3—Sn1 bond (2.560(3) Å), followed by a Sn1—Sn2 bond (2.925(1) Å), and finally a Sn2—Co1 bond (2.611(2) Å) linking the outer atoms to the inner cage. The short Sn1—Sn2 bond distance lies between the anionic-like Sn atoms in $Yb_3Rh_4Sn_{13}$ (2.9672(7) Å) and the strongly bonded zigzag chains of Sn in Yb_3CoSn_6 (2.945(2) Å) and $SrNiSn_2$ (2.843(2) Å).[2.26-28] The Co—Sn bond distances are similar to those reported (2.50 – 2.59 Å) for ternary intermetallic compounds, such as $Gd_3Co_4Sn_{13}$, $Ln_4Co_2Sn_5$, and Yb_3CoSn_6.[2.27, 29, 30]

The Gd8-centered structural unit, as shown in Figures 2.3b and 2.3c, can be visualized by a unit cell shift of ½ along a primary axis. Gd8 is surrounded by an inner cage of Co2, Co6, and Sn7 atoms and a shell of Sn4, Sn6, and Sn8-centered units. The inner cage, as shown in

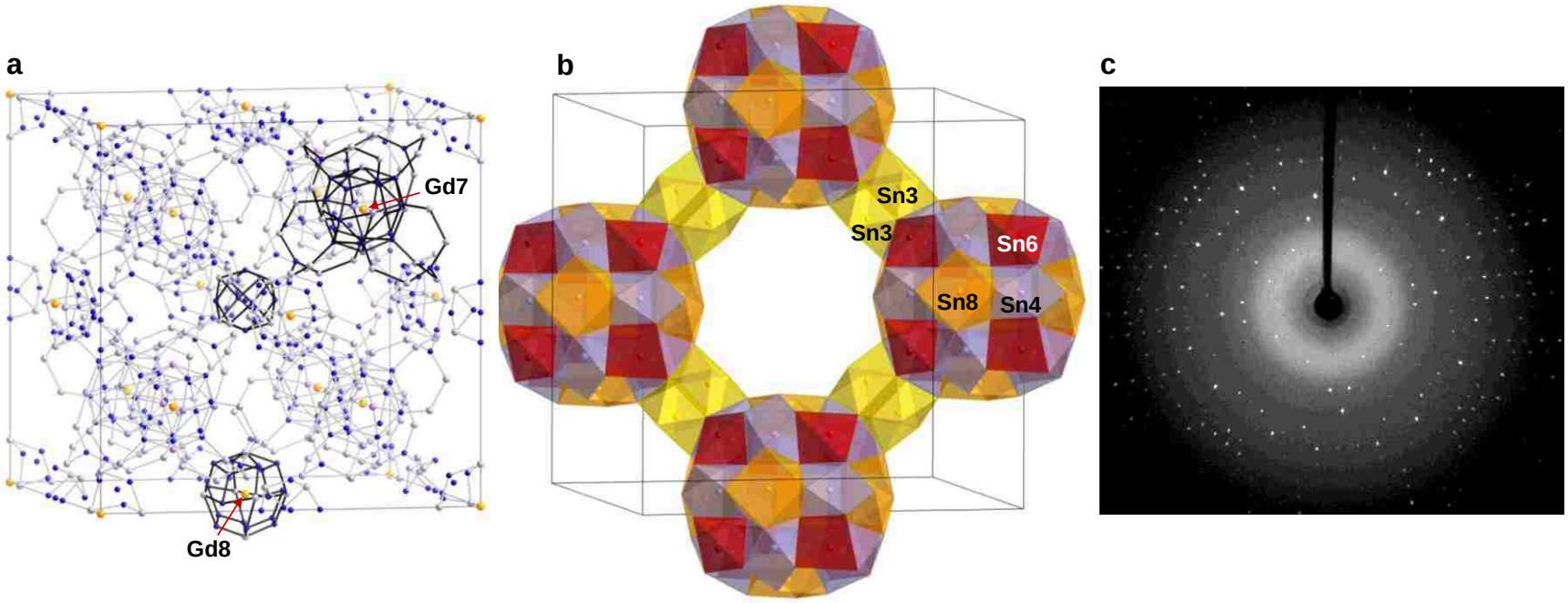

Figure 2.1. Crystal structure of $Gd_{117}Co_{56}Sn_{112}$. **(a)** The bonding Co—Sn, Sn—Sn, and Co—Co network within $Gd_{117}Co_{56}Sn_{112}$. Co5- (central unit), Gd7-, and Gd8-centered structural unit bonds are highlighted in black for clarity. **(b)** Network of Sn3, Sn4, Sn6, and Sn8-centered polyhedra. **(c)** X-ray diffraction pattern oriented in the 100 direction for a single crystal of $Gd_{117}Co_{56}Sn_{112}$ with a crystal to detector distance of 40 mm and a scan width of 2.0 °.

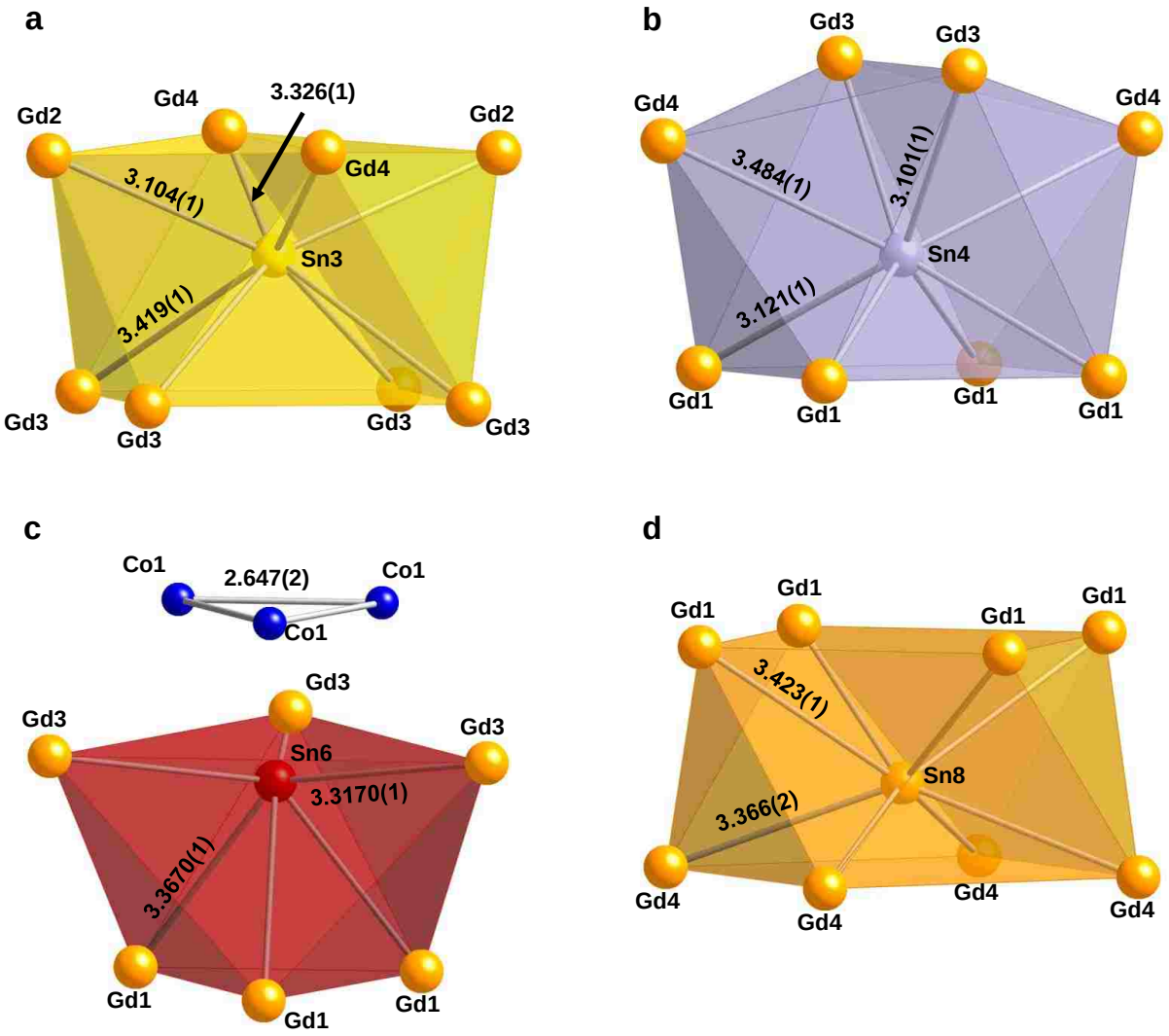

Figure 2.2. Sn-centered units showing **(a)** Sn3@Gd_8 bicapped trigonal prism, (**b**) Sn4@Gd_8 bicapped trigonal prism, (**c**) Sn6@Gd_6Co_3 axially capped distorted octahedron, and (**d**) Sn8@Gd_8 rectangular antiprism environments.

Figure 2.3b, consists of Co2 (50 % occupied) and Co6 (41.8(12) % occupied) atoms bonded to Sn7 at 2.600(3) Å) and Co2 at 2.386(4) Å, respectively. The outer shell, as shown in Figure 2.3c, consists of a cuboctahedral coordination of Sn4 units, a cubic coordination of Sn6 units, and a tetrahedral coordination of Sn8 units. Although Gd8 centered structural units pack in a FCC arrangement, only the four face-centered Gd8 structural units along the (2 0 0) plane are shown in Figure 2.1b for clarity. Gd8-centered structural units are connected by face sharing Sn3 units shown in Figure 2.1b and Figure 2.2a.

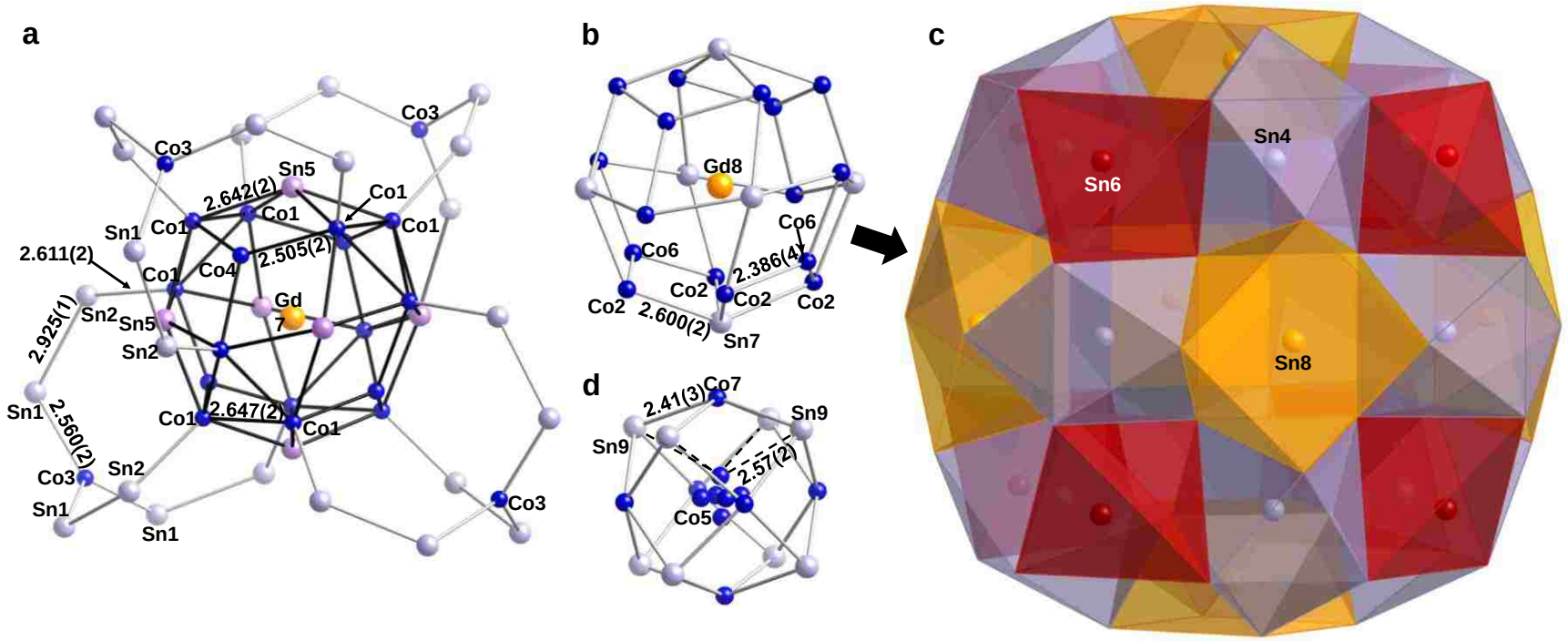

Figure 2.3. Structural units of $Gd_{117}Co_{56}Sn_{11}$. (**a)** Gd7-centered structural unit inner cage (bonds are highlighted in black for clarity) and outer peripheral atoms. (**b)** Inner cage of the Gd8-centered structural unit with ½ of the Co2 (50 % occupied) atoms omitted for clarity. **(c)** Outer coordination of Sn4, Sn6, and Sn8-centered units about Gd8. (**d)** Co6-centered structural unit. The Sn9′ split position is shown as a single position for clarity.

The Co5-centered structural unit, as shown in Figure 2.3d, consists of a cubic orientation of Sn9 atoms capped on each face by partially occupied Co7 atoms, $Co5@Sn_8Co_6$. The Sn9—Sn9 distance (3.245(13) Å) is comparable to $Gd_3Co_4Sn_{13}$ and $SrSn_4$ (3.219 Å and 3.287 Å, respectively), which are considered weakly bonded or non-bonding.[2.31, 32] The Sn9 cubic cage is bonded together by partially occupied Co7 at a distance of 2.40(3) Å, which is shorter than typical Co—Sn bond distances of 2.50 – 2.59 Å for ternary intermetallic compounds, such as $Gd_3Co_4Sn_{13}$, $Ln_4Co_2Sn_5$, and Yb_3CoSn_6.[2.27, 29, 30] Splitting of the Sn9 position allows the Co—Sn bond distance to relax to a distance of 2.71(5) Å (not shown). The partially occupied Co5 position is also split into an octahedral coordination of 6 positions with a Co5—Sn9 bond distance of 4 x 2.56(2) Å. The splitting of the Co5 and Sn9 positions has been previously found for $Sm_{117}Co_{52}Sn_{112}$;[2.21] however, it was not necessary to split the split Co7 position for the Gd analogue. It is worth noting that all atoms are shown in our structural depiction except the Gd5 and Gd6 (split position) atoms (not shown for clarity) which are located about the edges and faces of the Sn9 cages, respectively.

The Co5—Sn9 and Co3—Sn1 bond distances of 2.536(2) Å and 2.560(2) Å, respectively, are less than the sum of the covalent radii of Co (1.26 Å) and Sn (1.41 Å). The bond distances are also far greater than the sum of the largest ionic radii given by Shannon for both Sn and Co.[2.25] Therefore, the Co—Sn bonds appear to have a covalent-ionic character, similar to the Rh—Sn bonds reported for the $Ln_3Rh_4Sn_{13}$ and $Er_5Rh_6Sn_{18}$ compounds.[2.28, 33, 34]

2.3.2 Physical Properties

The temperature dependence of the electrical resistivity of single crystal $Gd_{117}Co_{56}Sn_{112}$ from 2 to 375 K is shown in Figure 2.4a. The resistivity increases with decreasing temperature ($d\rho/dT < 0$) throughout the entire temperature range, with the lowest measured value of 0.510

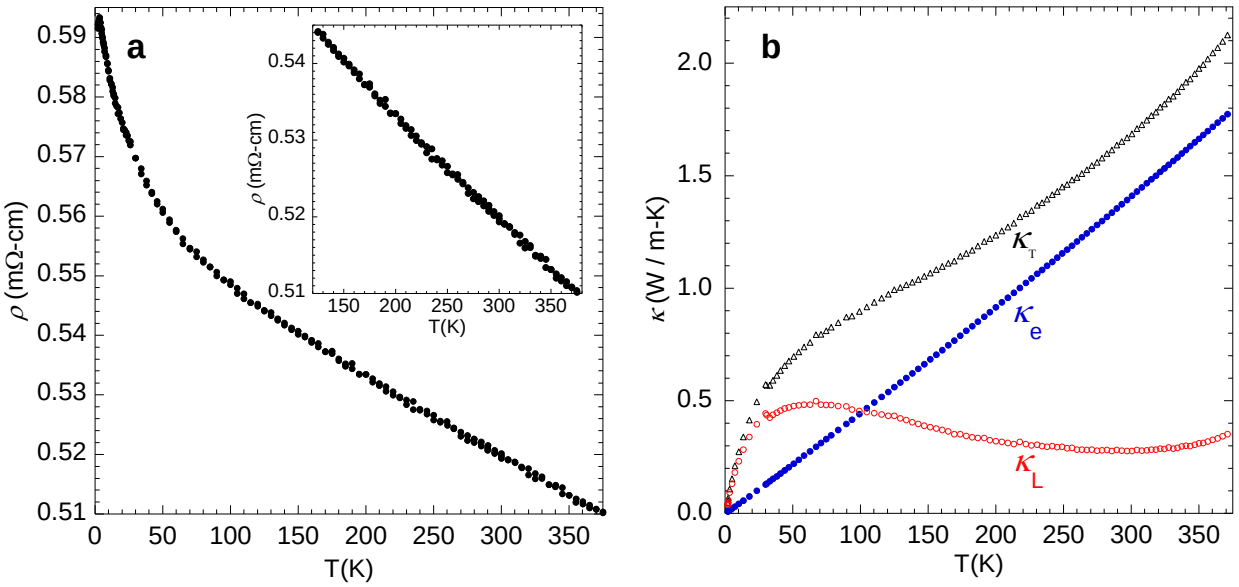

Figure 2.4. **(a)** Resistivity as a function of temperature for $Gd_{117}Co_{56}Sn_{112}$ from 2–375 K. The upper inset shows the linearly decreasing resistivity over the temperature range 125–375 K. **(b)** Thermal conductivity as a function of temperature for $Gd_{117}Co_{56}Sn_{112}$ from 2–375 K. κ_T is the total thermal conductivity, and κ_e and κ_L are the electronic and lattice thermal conductivities, respectively.

mΩ·cm at the highest measured temperature of 375 K. A small kink in the resistivity at low temperature near 3.5 K is due to a small amount of Sn inclusion (residual flux) in the crystal, which is suppressed by the application of a magnetic field (Appendix Figure A2.1, inset). (The superconducting transition temperature of Sn is $T_{c\text{-Sn}}$ = 3.7 K.) The negative slope in the low temperature region (3–50 K) indicates the transport is dominated by thermal activation, where the carrier density varies as $e^{-E_g/2k_BT}$. Thus, the slope of ln(ρ) vs $1/(2k_BT)$ gives a good approximation of the energy gap, E_g. Using this approximation, we find E_g ~ 0.004 eV or ~ 50 K. The very small value for E_g suggests a pseudogap, as opposed to a real energy gap, exists in the density of states at the Fermi level. Similar resistivity trends have been noted in quasicrystalline systems,[2.35, 36] which have been explained by a pseudogap, and in amorphous transition metal alloys.[2.37] $Gd_{117}Co_{56}Sn_{112}$ exhibits negative magnetoresistance, shown in

Appendix Figure A2.1, with maximum values at 14 T of ~ -14 %, -12 %, and -3 % at 3 K, 20 K, and 70 K, respectively.

Figure 2.4b shows the electronic (κ_e), lattice (κ_L), and total (κ_T) thermal conductivity data for $Gd_{117}Co_{56}Sn_{112}$ from 2–375 K. κ_e was estimated using the resistivity data in conjunction with $\kappa_e = L_0T/\rho$, and κ_L was calculated using the relationship $\kappa_L = \kappa_T + \kappa_e$. The total thermal conductivity of $Gd_{117}Co_{56}Sn_{112}$ is small over the entire measured temperature range and comparable to Al-based icosahedral quasicrystals.[2.35] The calculated room temperature value for κ_L is exceptionally low at 0.28 W/m-K. A comparison can be made to thermoelectric materials, which typically have low κ_L values. The κ_L of $Gd_{117}Co_{56}Sn_{112}$ is lower than all the best known thermoelectric materials, including $Yb_{14}MnSb_{11}$, which has an estimated room temperature lattice thermal conductivity of ~ 0.55 W/(m·K).[2.38] κ_L has a maximum value of ~ 0.50 W/(m·K) at 67 K, which is ~ $\Theta_D/5$ (*vide infra*) – the relationship which typically relates Θ_D to the maximum thermal conductivity in metallic systems.[2.4] Other solid materials have lower thermal conductivities, such as bulk silica aerogel[2.39, 40] and WSe_2;[2.41] however, the former is a porous, two-phase insulator, and the latter consists of disordered two-dimensional thin films. (As a comparison, the thermal conductivity of bulk single-crystalline WSe_2 is ~1.5 W/(m·K) near room temperature.)[2.41] In this regard, the lattice thermal conductivity of $Gd_{117}Co_{56}Sn_{112}$ is extremely low for a bulk single crystal.

The low lattice thermal conductivity in $Gd_{117}Co_{56}Sn_{112}$ can be explained by the large number of atoms (N) in the primitive unit cell, its complex structural units, the high atomic masses of its constituent elements, and its large unit cell volume. Phonon scattering processes can be classified as two types N and U, where N-processes (normal) conserve phonon

momentum during the collision process, and *U*-processes (umklapp) do not.[2.4] Thus, umklapp scattering is the dominant mechanism at reducing the thermal conductivity in crystalline solids (at high temperatures). After a *U*-process, the resulting phonon momentum wave vector lies outside the Brillouin zone. The wave vector, however, is equivalent to one in the same zone via a transformation with a reciprocal lattice vector. The large lattice constants of $Gd_{117}Co_{56}Sn_{112}$ give rise to a small Brillouin zone (in momentum or reciprocal space). Thus, for a given phonon momentum, the likelihood of *U*-processes increases.

Unlike other complex unit cell materials with low thermal conductivity,[2.42] the low electrical resistivity of $Gd_{117}Co_{56}Sn_{112}$ results in the total thermal conductivity being dominated by the electronic contribution. In addition, an increase in the slope of the lattice thermal conductivity is observed at high temperatures above 300 K which is unusual, as the lattice thermal conductivity in most bulk solids tends to decrease with increasing temperature. A large enhancement of κ_e relative to κ_L at higher temperature (> 100 K) can occur in small band gap semiconductors and semimetals[2.4] and is indicative of bipolar diffusion effects (conduction of electrons and holes) – an interpretation also supported by the thermopower and Hall coefficient data presented below. This behavior in the thermal conductivity is consistent with the presence of a symmetric pseudogap at the Fermi level. Such a description was used to model the thermal conductivity in structurally complex Al alloys.[2.42]

Figure 2.5a shows the Seebeck coefficient as a function of temperature from 30–375 K. The largest value recorded for the Seebeck coefficient is 2.2 μV/K, which corresponds to the lowest measured temperature. The thermopower has a negative temperature coefficient and crosses zero at ~ 225 K. Hall resistivity (ρ_H) as a function of magnetic field shows an anomalous Hall coefficient (R_H) behavior (Appendix Figure A2.2); thus, the R_H data were fit at low and high

field. R_H as a function of temperature is shown in Figure 2.5b. Typically, the sign of R_H mirrors that of the Seebeck coefficient, signifying the dominant charge carrier as electrons (negative) or holes (positive); however, R_H for $Gd_{117}Co_{56}Sn_{112}$ shows the opposite trend. R_H is negative at low temperatures, and reduces in magnitude as a function of temperature which is opposite to the thermopower behavior. The Hall coefficient approaches zero at ~ 300 K (Figure2.5b), slightly higher in temperature than the zero-crossing of the thermopower ~ 225 K. The zero-crossing in the Hall coefficient and thermopower, as well as their low values, indicate that $Gd_{117}Co_{56}Sn_{112}$ is a partially compensated (bipolar) material throughout the entire measured temperature range.

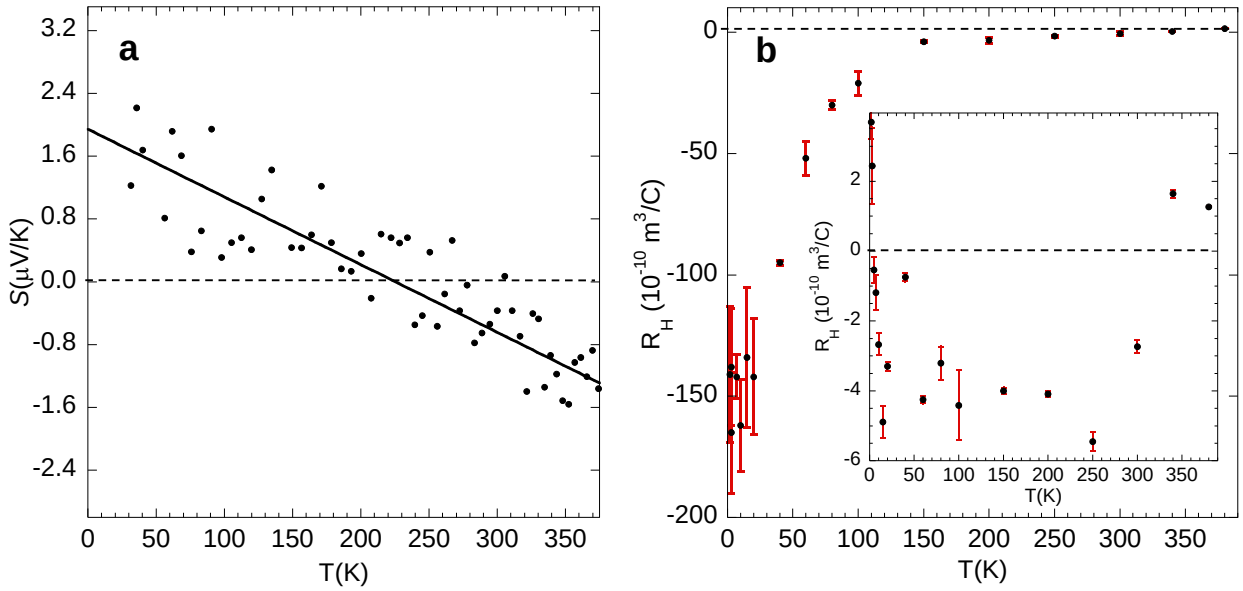

Figure 2.5. (a) Thermopower as a function of temperature for $Gd_{117}Co_{56}Sn_{112}$ from 30–375 K. The solid line is a linear best-fit for all data points, and the dashed line indicates the zero-line of the thermopower. **(b)** Low field and high field (inset) Hall coefficient as a function of temperature for $Gd_{117}Co_{56}Sn_{112}$. The dashed lines indicate the zero-line of the Hall coefficient.

In a bipolar material, the full form of the electronic thermal conductivity is represented by $\kappa_e = \kappa_{e,1} + \kappa_{e,2} + [(\sigma_1\sigma_2)/(\sigma_1 + \sigma_2)](S_1 - S_2)^2T$, where the numbers 1 and 2 denote the types of charge carriers, σ is electrical conductivity, and S is the Seebeck coefficient. Typically, the third term is ignored in κ_e calculations; however, the value becomes significant in bipolar materials,

when S_1 and S_2 are opposite in sign and σ_1 and σ_2 are of equal magnitude. Since $Gd_{117}Co_{56}Sn_{112}$ appears to be a bipolar material, the calculated value of κ_e should be considered as a lower limit, or more importantly, our calculated value of κ_L represents its maximum value.

Further insight into how well $Gd_{117}Co_{56}Sn_{112}$ approximates a PGEC is gained by calculating the value $1/(\rho\kappa_L)$, where the limit of $1/(\rho\kappa_L) \rightarrow \infty$ represents the ideal case. Table 2.3 shows the room temperature values of $1/(\rho\kappa_L)$ for $Gd_{117}Co_{56}Sn_{112}$ and some of the best-known thermoelectrics. As shown in the Table 2.3, single crystalline $Gd_{117}Co_{56}Sn_{112}$ has a value of $1/(\rho\kappa_L) = 6.87 \times 10^5$ K/(Ω·W). This value is well above those for any of the conventional thermoelectric materials, including a factor of 6 better than Bi_2Te_3.

Table 2.3. Estimated lattice thermal conductivity (κ_L), electrical resistivity (ρ), and $1/(\rho\kappa_L)$ values at 300 K of some of the best known bulk thermoelectric materials

Material	κ_L [W/(m·K)]	ρ [10^{-5} Ω·m]	$1/(\rho\kappa_L)$ [10^3 K/(Ω·W)]
[a] $(Bi/Sb)_2Te_3$ [2.44]	0.6	0.794	209.9
[b] $(Bi/Sb)_2Te_3$ [2.44]	0.9	1	111.1
$Si_{0.75}Ge_{0.25}$ [2.45]	3.5	1.1	26.0
[c] $Ba_{0.08}La_{0.05}Yb_{0.04}Co_4Sb_{12}$ [2.46]	1.16	0.417	206.7
$PbTe_{0.5}Se_{0.5}$ [2.47]	0.58	2	86.2
TAGS-75 [2.8]	0.8	1.6	78.1
$MnSi_{1.75}$ [2.48, 49]	2.9	1.4	24.6
$Yb_{14}MnSb_{11}$ [2.38]	0.55	2	90.9
Ag_9TlTe_5 [2.50]	0.23	130	3.3
$Gd_{117}Co_{56}Sn_{112}$	0.28	0.52	686.8

[a] Nanocrystalline sample [b] Zone-melted sample [c] Skutterudite structure

Figure 2.6a shows zero-field cooled (ZFC) and field cooled (FC) magnetic susceptibility data for $Gd_{117}Co_{49}Sn_{116}$ from 3–290 K measured at 0.1 T. The ZFC data are fit using the modified Curie Weiss law $\chi = \chi_0 + C/(T - \theta_{CW})$, where χ_0 is the temperature-independent susceptibility, C is the Curie-Weiss constant, and θ_{CW} is the Curie-Weiss temperature. Our fit in

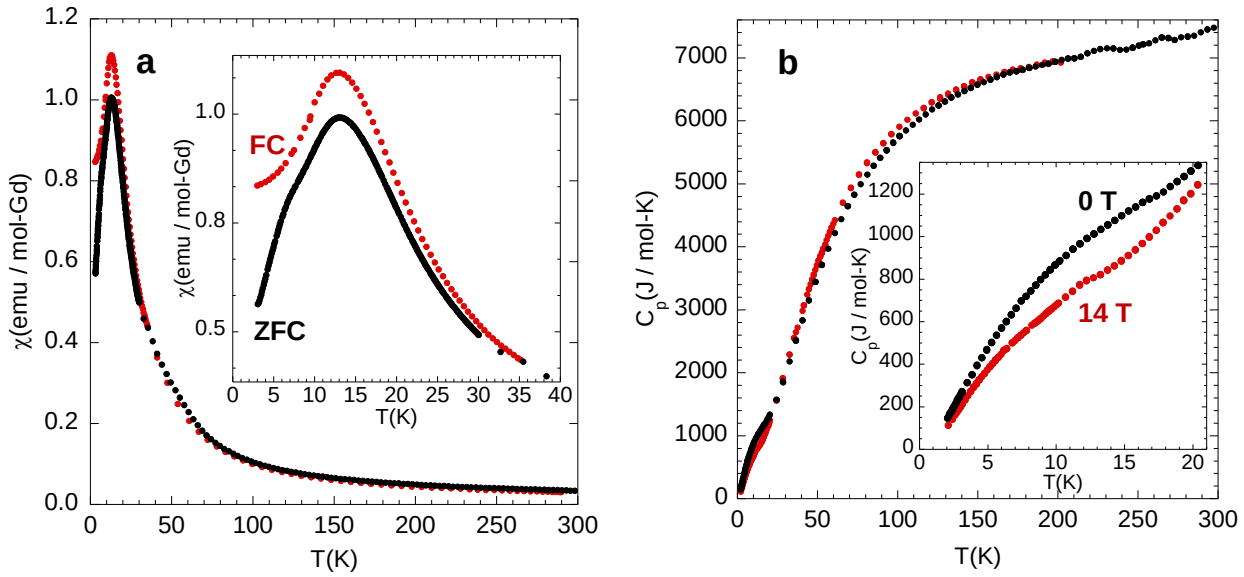

Figure 2.6. **(a)** Magnetic susceptibility as a function of temperature for $Gd_{117}Co_{56}Sn_{112}$ from 3–300 K under ZFC (black circles) and FC (red circles) conditions at 0.1 T. **(b)** Heat capacity (C_p) as a function of temperature for $Gd_{117}Co_{56}Sn_{112}$ from 2–300 K at 0 T (black circles) and 14 T (red circles). The inset shows C_p v T from 2–21 K at 0 and 14 T.

the temperature range 150–292 K gives χ_0 = 0.0066(4) emu/(mol·Gd), θ_{CW} = 16(2) K, and C = 7.89(15) emu/(mol·Gd). The experimentally calculated magnetic moment of μ_{eff} = 7.94(7) μ_B/Gd is in excellent agreement with the theoretical magnetic moment of μ_{calc} = 7.94 μ_B/Gd. The ZFC and FC susceptibility data show an antiferromagnetic transition at 13 K, which is similar in magnitude to the fitted θ_{CW} = 16.2(2) K, but the positive θ_{CW} sign and negative magnetoresistance suggest ferromagnetic interactions. The presence of ferromagnetic interactions is reinforced by a divergence in the ZFC and FC magnetic susceptibility shown in Figure 2.6a, inset. This behavior is similar to the previously reported Tb (θ_{CW} = 59 K) and Dy (θ_{CW} = 18 K) analogues[2.21] which also exhibit antiferromagnetic transitions at 22 and 11 K, respectively. Field dependent magnetization taken at 3 and 12 K (Appendix Figure A2.3) shows a linear dependence of magnetization as a function of field and show no sign of saturation at high

field, consistent with antiferromagnetic interactions; however, the measurement taken at 3 K shows a small hysteresis at low field, which is not present in the 12 K measurement.

Figure 2.6b shows the temperature dependence of the heat capacity at 0 and 14 T. At low temperatures, there are anomalies at ~ 18 K and ~ 14 K for the 0 and 14 T data, respectively. These anomalies (Figure 2.6b, inset), which appear to be suppressed to a lower temperature with the application of a magnetic field, support our observation of an antiferromagnetic transition ~13 K from the magnetic susceptibility data. Prior to the magnetic phase transition, we find that specific heat shows linear behavior from 16 to 33 K at 14 T when plotted as C_p/T vs. T^2 (Appendix Figure A2.4). Thus, we fit data using $C_p/T = \gamma + \beta T^2$, where γ and β are the electronic and phonon contributions to the heat capacity, respectively. The fit gives γ = 55.17(9) J/(mol(F.U.)·K^2) and a Debye temperature Θ_D = 336.3(12) K using the relationship $\beta = 12\pi^4 RN / 5\Theta_D^3$, where R = 8.314 J/(mol·K) and N is the number of atoms per formula unit. A Debye temperature > 300 K is expected since the heat capacity does not saturate up to the maximum measured temperature of 300 K. An additional anomaly at ~ 6 K can be seen in the C_P/T vs T^2 plot, which is likely an additional magnetic transition. This transition corresponds to the shoulder at 6 K in the ZFC susceptibility shown in Figure 2.6a, inset.

2.4 Conclusions

We began our study of $Gd_{117}Co_{56}Sn_{112}$ with the assumption that the lattice thermal conductivity should be exceptionally low due to the complexity of the crystal structure. The results exceeded our expectation with a lattice thermal conductivity of κ_L = 0.28 W/(m·K) at 300 K, which represents one of the lowest values ever measured for a bulk crystalline material. To our surprise, $Gd_{117}Co_{56}Sn_{112}$ also has a low electrical resistivity with semiconducting-like behavior, which gives a $1/(\rho\kappa_L)$ value of 6.87 × 10^5 K/Ω·W. The low Seebeck coefficient

precludes $Gd_{117}Co_{56}Sn_{112}$ from joining the list of viable thermoelectric materials in its pure form; however, doping studies and high temperature transport measurements on $Gd_{117}Co_{56}Sn_{112}$ may prove effective at improving its performance. Tuning the Fermi level by chemically doping through a pseudogap in similar materials, such as Si-doped Al-Re alloys,[2.43] has produced significant enhancements in thermopower. Furthermore, we are compelled to investigate $Gd_{117}Co_{56}Sn_{112}$ as a potential *thermomagnetic* material. A simple explanation for a zero Hall coefficient is to assume equal numbers of electrons and holes with equal mobilities. Of course, the real material is undoubtedly more complex. Nonetheless, thermomagnetic cooling relies on contributions from both types of charge carriers, which are clearly intrinsic to this material. Another potential application is a device that requires electrical conduction but a high degree of thermal shielding, where very few materials meet these criteria. In any case, the extremely low lattice thermal conductivity and large value of $1/(\rho\kappa_L)$ establishes $Gd_{117}Co_{56}Sn_{112}$ as a new class of materials deserving of further exploration.

2.5 References

2.1. Mahan, G. D., *Good Thermoelectrics*. Academic Press Inc: San Diego, 1998; Vol. 51, p 81-157.

2.2. Snyder, G. J.; Toberer, E. S., *Nat. Mater.* **2008,** *7*, 105-114.

2.3. Tritt, T. M., *Annu. Rev. Mater. Res.* **2011,** *41*, 433-448.

2.4. Tritt, T. M., *Thermal Conductivity Theory, Properties and Applications*. Kluwer Academic: New York, 2004; p 290.

2.5. Toberer, E. S.; May, A. F.; Snyder, G. J., *Chem. Mater.* **2009**.

2.6. Slack, G. A., New Materials and Performance Limits for Thermoelectric Cooling. In *CRC Handbook of Thermoelectrics*, Rowe, D. M., Ed. CRC Press: Boca Raton, FL, 1995; pp 407-440.

2.7. Snyder, G. J.; Christensen, M.; Nishibori, E.; Caillat, T.; Iversen, B. B., *Nat. Mater.* **2004,** *3*, 458-463.

2.8. Yang, S. H.; Zhu, T. J.; Sun, T.; Zhang, S. N.; Zhao, X. B.; He, J., *Nanotechnology* **2008,** *19*.

2.9. Hsu, K. F.; Loo, S.; Guo, F.; Chen, W.; Dyck, J. S.; Uher, C.; Hogan, T.; Polychroniadis, E. K.; Kanatzidis, M. G., *Science* **2004,** *303*, 818-821.

2.10. DiSalvo, F. J., *Science* **1999,** *285*, 703-706.

2.11. Bodak, O. P.; Gladyshe.Ei, *Sov. Phys. Crystallogr.* **1970,** *14*, 859-861.

2.12. Yan, J. L.; Xu, Y.; Long, Q. X.; Zhu, J. M.; Zhuang, Y. H., Springer: 2009; pp 435-442.

2.13. Otwinowski, Z.; Minor, W., *Method Enzymol.* **1997,** *276*, 307-326.

2.14. Burla, M. C.; Carrozzini, B.; Cascarano, G. L.; Giacovazzo, C.; Polidori, G., *Z. Kristallogr.* **2002,** *217*, 629-635.

2.15. Sheldrick, G. M., *Acta Crystallogr.* **2008,** *64*, 112-122.

2.16. Salamakha, P.; Sologub, O.; Bocelli, G.; Otani, S.; Takabatake, T., *J. Alloys Comp.* **2001,** *314*, 177-180.

2.17. Pecharsky, V. K.; Bodak, O. I.; Belsky, V. K.; Starodub, P. K.; Mokra, I. R.; Gladyshevskii, E. I., *Kristallografiya* **1987,** *32*, 334-338.

2.18. Morozkin, A. V.; Seropegin, Y. D.; Portnoy, V. K.; Sviridov, I. A.; Leonov, A. V., *Mater. Res. Bull.* **1998,** *33*, 903-908.

2.19. Cirafici, S.; Canepa, F.; Manfrinetti, P.; Napoletano, M., *J. Alloys Comp.* **2001,** *317-318*, 550-555.

2.20. He, W.; Zhang, J. L.; Yan, J. L.; Fu, Y. C.; Zeng, L. M., *J. Alloys Comp.* **2010,** *491*, 49-52.

2.21. Kovnir, K.; Shatruk, M., *Eur. J. Inorg. Chem.* **2011**.

2.22. Salamakha, P.; Demchenko, P.; StepienDamm, J., *J. Alloys Comp.* **1997,** *260*, L1-L3.

2.23. Hohnke, D.; Parthé, E., *Acta Cryst.* **1966,** *21*, 435-437.

2.24. Ganguli, A. K.; Guloy, A. M.; Leonescamilla, E. A.; Corbett, J. D., *Inorg. Chem.* **1993,** *32*, 4349-4353.

2.25. Shannon, R. D., *Acta Crystallogr.* **1976,** *32*, 751-767.

2.26. Hlukhyy, V.; Eck, S.; Fässler, T. F., *Inorg. Chem.* **2006,** *45*, 7408-7416.

2.27. Lei, X. W.; Zhong, G. H.; Li, M. J.; Mao, J. G., *J. Solid State Chem.* **2008,** *181*, 2448-2455.

2.28. Hodeau, J. L.; Chenavas, J.; Marezio, M.; Remeika, J. P., *Solid State Commun.* **1980,** *36*, 839-845.

2.29. Pires, M. A.; Ferreira, L. M.; Duque, J. G. S.; Urbano, R. R.; Aguero, O.; Torriani, I.; Rettori, C.; Bittar, E. M.; Pagliuso, P. G., *J. Appl. Phys.* **2006,** *99*, 1-3.

2.30. Pani, M.; Manfrinetti, P.; Palenzona, A.; Dhar, S. K.; Singh, S., *J. Alloys Comp.* **2000,** *299*, 39-44.

2.31. Zhong, G. H.; Lei, X. W.; Mao, J. G., *Phys. Rev. B* **2009,** *79*, 1-13.

2.32. Hoffmann, S.; Fassler, T. F., *Inorg. Chem.* **2003,** *42*, 8748-8754.

2.33. Miraglia, S.; Hodeau, J. L.; Marezio, M.; Laviron, C.; Ghedira, M.; Espinosa, G. P., *J. Solid State Chem.* **1986,** *63*, 358-368.

2.34. Hodeau, J. L.; Marezio, M.; Remeika, J. P., *Acta Cryst.* **1984,** *40*, 26-38.

2.35. Gianno, K.; Sologubenko, A. V.; Chernikov, M. A.; Ott, H. R.; Fisher, I. R.; Canfield, P. C., *Materials Science and Engineering a-Structural Materials Properties Microstructure and Processing* **2000,** *294*, 715-718.

2.36. Takeuchi, T.; Onogi, T.; Otagiri, T.; Mizutani, U.; Sato, H.; Kato, K.; Kamiyama, T., *Phys. Rev. B* **2003,** *68*.

2.37. Rapp, O.; Jackle, J.; Frobose, K., *J. Phys. F Met. Phys.* **1981,** *11*, 2359-2366.

2.38. Cox, C. A.; Toberer, E. S.; Levchenko, A. A.; Brown, S. R.; Snyder, G. J.; Navrotsky, A.; Kauzlarich, S. M., *Chem. Mater.* **2009,** *21*, 1354-1360.

2.39. Richter, K.; Norris, P. M.; Tien, C.-L., Aerogels: applications, structure and heat transfer phenomena. In *Annual Review of Heat Transfer*, Tien, C.-L., Ed. Begell House, Inc.: New York City, NY, 1995; Vol. VI, pp 61-114.

2.40. Norris, P. M.; Shrinivasan, S., Aerogels: unique material, fascinating properties, and unlimited applications. In *Annual Review of Heat Transfer*, Prasad, B.; Jaluria, Y.; Chen, G., Eds. Begell House, Inc.: New York City, NY, 2005; Vol. XIV, pp 385-408.

2.41. Chiritescu, C.; Cahill, D. G.; Nguyen, N.; Johnson, D.; Bodapati, A.; Keblinski, P.; Zschack, P., *Science* **2007,** *315*, 351-353.

2.42. Takeuchi, T., *J. Electron. Mater.* **2009,** *38*, 1354-1359.

2.43. Takeuchi, T.; Otagiri, T.; Sakagami, H.; Kondo, T.; Mizutani, U.; Sato, H., *Phys. Rev. B* **2004,** *70*.

2.44. Poudel, B.; Hao, Q.; Ma, Y.; Lan, Y. C.; Minnich, A.; Yu, B.; Yan, X. A.; Wang, D. Z.; Muto, A.; Vashaee, D.; Chen, X. Y.; Liu, J. M.; Dresselhaus, M. S.; Chen, G.; Ren, Z. F., *Science* **2008,** *320,* 634-638.

2.45. Meddins, H. R.; Parrott, J. E., *J. Phys. C Solid State* **1976,** *9,* 1263-1276.

2.46. Shi, X.; Yang, J.; Salvador, J. R.; Chi, M. F.; Cho, J. Y.; Wang, H.; Bai, S. Q.; Yang, J. H.; Zhang, W. Q.; Chen, L. D., *J. Am. Chem. Soc.* **2011,** *133,* 7837-7846.

2.47. Li, J. Q.; Li, S. P.; Wang, Q. B.; Wang, L.; Liu, F. S.; Ao, W. Q., *J. Alloys Comp.* **2011,** *509,* 4516-4519.

2.48. Vining, C. B., Thermoelectric properties of silicides. In *CRC Handbook of Thermoelectrics*, Rowe, D. M., Ed. CRC Press: Boca Raton, FL, 1995; pp 277-298.

2.49. Zaitsev, V. K., Thermoelectric properties of anisotropic $MnSi_{1.75}$. In *CRC Handbook of Thermoelectrics*, Rowe, D. M., Ed. CRC Press: Boca Raton, FL, 1995; pp 299-309.

2.50. Kurosaki, K.; Kosuga, A.; Muta, H.; Uno, M.; Yamanaka, S., *Appl. Phys. Lett.* **2005,** *87*.

Chapter 3.[†] Structural Complexity Meets Transport and Magnetic Anisotropy in Single Crystalline $Ln_{30}Ru_4Sn_{31}$ (*Ln* = Gd–Dy)

3.1 Introduction

Intermetallic compounds display a variety of useful bulk properties, including magnetocaloric effects, superconductivity, and thermoelectric behavior. For instance, $Gd_5Si_2Ge_2$ displays a giant magnetocaloric effect near room temperature.[3.1] MgB_2[3.2] and $Ba_{0.6}K_{0.4}Fe_2As_2$[3.3] are oxygen-free materials that have been shown to be superconductors near 40 K, and low-temperature properties such as unconventional superconductivity, heavy fermion behavior, and exotic magnetism have also been observed in a variety of intermetallic compounds.[3.4] Additionally, intermetallic compounds, such as Zn_4Sb_3[3.5] and $Yb_{14}MnSb_{11}$,[3.6] exhibit exemplary physical properties for thermoelectric applications.

Anisotropic properties of intermetallic materials are less studied, since high quality, sizeable single crystals are necessary for these measurements. This precludes the use of popular synthetic methods such as arc-melting and ball milling, which produce polycrystalline products. Single crystals must also be oriented along crystallographic directions using, for example, Laue diffraction before anisotropic physical property measurements can be performed. Moreover, the macroscopic geometry of the crystals is important in transport property measurements that are highly influenced by crystal shape and size, such as electrical resistivity, thermopower, and thermal conductivity. Thus, measurement of a well-shaped crystal, such as a polished bar, is ideal, while crystals with shorter macroscopic axes, such as needles and plates, can introduce significant experimental error when measuring along the short axis. Anisotropic magnetic

[†]Reproduced with permission from Schmitt, D. C.; Haldolaarachchige, N.; Prestigiacomo, J.; Karki, A.; Young, D. P.; Stadler, S.; Jin, R.; Chan, J. Y., *J. Am. Chem. Soc.* **2013,** *135*, 2748-2758.

properties, however, are more common, as the macroscopic crystal shape typically has a less pronounced effect on experimental error.

Despite these difficulties, anisotropic physical properties measurements have been reported for a number of intermetallic systems in an effort to study complex electrical and magnetic phenomena. For example, anisotropic magnetization measurements have been performed for several intermetallic compounds, including Eu_3InP_3[3.7] and $EuGa_2P_2$,[3.8] which show multiple field-direction-dependent magnetic ordering transitions. Polycrystalline $Ce_3Cu_4Sn_4$ exhibits multiple magnetic ordering events in temperature-dependent magnetization data, and fits from neutron data confirm the coexistence of two anisotropic magnetic sublattices corresponding to the two crystallographically unique Ce positions.[3.9] Giant and highly anisotropic magnetocaloric effects have been observed in the magnetocaloric material $EuFe_2As_2$ at T = 20 K.[3.10] Though less common, many examples of anisotropic intermetallic electrical properties exist. $Al_{72.5}Mn_{21.5}Fe_{6.0}$ exhibits anisotropic electrical resistivity but was found to have a nearly isotropic Fermi surface with the resistivity differences caused by anisotropic quenched defect scattering,[3.11] while the origin of the highly electrically anisotropic *d*-Al-Co-Ni decagonal quasicrystalline phase was found to be a highly anisotropic Fermi surface.[3.12] Other notable examples of intermetallics displaying anisotropic electrical properties include the high-temperature Kondo systems URu_2Si_2[3.13] and $CePt_2In_7$,[3.14] and the iron-arsenide superconducting compounds $BaFe_2As_2$[3.15] and $CaFe_4As_3$.[3.16]

We have recently reported on the exceptionally low lattice thermal conductivity (κ_L = 0.28 W/m•K) and unusual semiconducting-like transport behavior of $Gd_{117}Co_{56}Sn_{112}$.[3.17] A similar growth technique was employed, using the self-flux method, in an effort to synthesize a Ru analogue. Instead, we found that single crystals of a highly complex rare earth-rich structure form with a new structure-type, which crystallizes in the orthorhombic space group *Pnnm* with a

total of 24 crystallographically unique atomic sites and 11 magnetic rare earth sites. With the large number of magnetic sites, comes the potential for multiple magnetic sublattices in the structure. Herein, we report on the growth and crystal structure of $Gd_{30}Ru_{4.92}Sn_{30.54}$, $Tb_{30}Ru_6Sn_{29.5}$, and $Dy_{30}Ru_{4.57}Sn_{30.72}$, as well as the magnetic, electronic, and thermal transport properties of single crystal $Gd_{30}Ru_{4.92}Sn_{30.54}$ and $Tb_{30}Ru_6Sn_{29.5}$. We found both magnetic anisotropy *and* highly anisotropic electrical transport behavior. Additionally, we found that the lattice thermal conductivity in $Tb_{30}Ru_6Sn_{29.5}$ is exceptionally low, and we compare our results to other Sn-containing materials.

3.2 Experimental

3.2.1 Synthesis

Ru powder, Sn shot, and ingots of Gd, Tb, and Dy (all $\geq$ 99.9 weight % purity, metal basis) were used for the preparation of $Ln_{30}Ru_{4+x}Sn_{31-y}$ (x = 0.57–2.0, y = 0.28–1.5). Elements were weighed out using a molar ratio of 12:6:11 (*Ln*:Ru:Sn), placed into an alumina crucible, and loaded into a fused silica tube which was evacuated (~ 1.2×10^{-3} atm). The total mass of starting material used in a typical reaction was ~1.5g. The addition of excess Sn results in the formation of $LnRuSn_2$ with the $CeNiSi_2$ structure-type.[3.18] The tubes were subsequently backfilled with ~0.2 atm Ar (to prevent fused silica tube collapse due to high maximum dwell temperatures) and were sealed. The reaction vessels were heated to 1260 °C at 100 °C/h, held at 1260 °C for 36 h, cooled at 1 °C/h to 1200 °C, and cooled at 5 °C/h to 1050 °C. The samples were then removed from the furnace and allowed to cool in air or quenched in water. Single crystals of $Ln_{30}Ru_{4+x}Sn_{31-y}$ were embedded in buttons of polycrystalline material typically consisting of multiple binary phases (including, in the case of the Gd analogue, $RuSn_2$, Gd_5Ru_2, Gd_2Ru, Gd_3Ru, and $GdRu_2$). Reactions were later carried out using a starting molar ratio of 12:4.75–5.25:11, which resulted in higher yields of the title compounds, with identical crystalline

stoichiometries. The title compounds all exhibit a dark grey or black color with metallic luster which is easily distinguishable from the surrounding polycrystalline matrix. Yields for the targeted phases were found to be the highest for the Tb analogue, with Tb > Gd > Dy. The single crystals were highly reactive with HNO_3, HCl, and H_2SO_4; thus, mechanical extraction was necessary to separate the single crystals from the surrounding polycrystalline matrix.

3.2.2 Elemental Analysis

Elemental analysis was performed using energy dispersive X-ray spectroscopy using a FEI Quanta 200 scanning electron microscope with an accelerating voltage of 20 keV. At least six points per sample were averaged together for each stoichiometric determination. Ru concentration showed little deviated (within instrumental error) between data points of individual analogues, indicating high sample homogeneity. The measured compositions of the samples were $Gd_{30(3)}Ru_{6(3)}Sn_{31(2)}$, $Tb_{30(3)}Ru_{7(2)}Sn_{32(3)}$, and $Dy_{30(3)}Ru_{6(2)}Sn_{33(2)}$. Error bars were determined by summing a fixed 3 atomic % instrumental error and the standard deviations of the data collected.

3.2.3 X-ray Diffraction

Powder X-ray diffraction was performed to determine homogeneity and phase purity using a Bruker D8 Advance X-ray diffractometer with monochromatic Cu Kα radiation with an incident beam Ge monochromator. Data were collected from 10–80 2θ with a resolution of 0.01°. Single crystal X-ray diffraction data were collected using a Nonius KappaCCD diffractometer with monochromatic Mo Kα radiation. Single crystals were cut to appropriate sizes (Table 3.1) and mounted to a glass fiber using epoxy. All data were collected with high redundancy, and a multi-scan absorption correction was applied during the scaling process. Overall R_{merge} values during scaling were less than 0.091 for all analogues. Statistics suggested that the structure was centrosymmetric. Systematic absences ($h0l$: $h + l = 2n$; $hk0$: $h + k = 2n$;

Table 3.1. Crystallographic parameters for $Ln_{30}Ru_{4+2x}Sn_{31-x}$ (Ln= Gd, Dy) and $Tb_{30}Ru_{6.0}Sn_{29.5}$

Formula	$Gd_{30}Ru_{4.92(5)}Sn_{30.54(9)}$	$Tb_{30}Ru_{6.0(4)}Sn_{29.5(7)}$	$Dy_{30}Ru_{4.57(5)}Sn_{30.72(9)}$
Crystal System	Orthorhombic	Orthorhombic	Orthorhombic
Space Group	*Pnnm*	*Pnnm*	*Pnnm*
a (Å)	11.784(1)	11.696(1)	11.659(1)
b(Å)	24.717(1)	24.505(1)	24.457(1)
c (Å)	11.651(2)	11.578(2)	11.564(2)
V (Å^3)	3393.5(7)	3318.4(7)	3297.4(7)
Z	2	2	2
Crystal dimensions (mm^3)	0.05 x 0.05 x 0.05	0.03 x 0.03 x 0.05	0.05 x 0.05 x 0.05
Temperature (K)	296(1)	296(1)	296(1)
θ range (º)	4.11 – 31.00	4.15 - 30.99	4.16 - 30.99
μ (mm^{-1})	40.872	43.63	45.872
Data Collection			
Measured Reflections	76592	71549	84140
Unique Reflections	5622	5502	5469
Reflections with I>2σ(I)	4762	4865	4368
R_{int}	0.0248	0.0181	0.0307
h	-17 to 17	-16 to 16	-16 to 16
k	-35 to 35	-35 to 35	-35 to 35
l	-16 to 16	-16 to 16	-16 to 16
Refinement			
$\Delta\rho_{max}$ (eÅ^{-3})/$\Delta\rho_{min}$ (eÅ^{-3})	2.525 / -2.391	2.19 / -1.643	3.407 / -2.339
GoF	1.287	1.29	1.101
Extinction coefficient	0.000111(5)	0.000133(4)	0.000200(6)
Reflections/Parameters	5622 / 183	5502 / 181	5469 / 183
R_1 ($F^2 > 2\sigma F^2$) [a]	0.0288	0.023	0.0291
wR_2 (F^2) [b]	0.0605	0.0436	0.0539

[a] $R_1 = \sum||F_o| - |F_c||/\sum|F_o|$.

[b] $wR_2 = [\sum[w(F_o^2 - F_c^2)]/\sum[w(F_o^2)^2]]^{1/2}$.

*h*00: *h* = 2*n*; 0*k*0: *k* = 2*n*; 00*l*: *l* = 2*n*) allowed for several possible space groups and indicated *n* glide planes in the *b* and *c* directions. Solutions were attempted in direct methods using SIR2002[3.19] in space groups with similar systematic absences (*Pnnn*, *Pnna*, *Pccn*, *Pmmn*, *Pbcn*, and *Pnma*), none of which returned valid solutions. Space groups *P*2*nn* and *Pmnn* were solved using SIR2002[3.19] and refined using SHELXL97.[3.20] An analysis of the refined model in space group *P*2*nn* using Platon[3.21] indicated missing mirror plane symmetry elements; thus, *Pmnn* was

used for all model refinements. Since *Pmnn* corresponded to a non-standard space group setting, the data were transformed to the standard space group setting of *Pnnm*. Crystallographic and atomic parameters are provided in Table 3.1 and Table 3.2, respectively. Atomic parameters for

Table 3.2. Positions, occupancies, and atomic displacement parameters for $Gd_{30}Ru_{4.92}Sn_{30.54}$

Atom	Site	*x*	*y*	*z*	Occ.	U_{eq} (Å^2) [a]
Gd1	4*g*	0.14000(5)	0.65899(2)	0	1	0.00981(11)
Gd2	4*g*	0.59006(5)	0.89950(2)	0	1	0.00920(11)
Gd3	4*g*	0.26447(5)	0.96935(2)	0	1	0.00885(11)
Gd4	4*g*	0.78306(5)	0.80299(2)	0	1	0.01078(12)
Gd5	4*e*	0	0	0.26566(5)	1	0.00854(11)
Gd6	4*g*	0.32790(5)	0.41893(2)	0	1	0.01155(12)
Gd7	8*h*	0.43894(3)	0.652434(16)	0.81903(3)	1	0.00944(8)
Gd8	8*h*	0.82070(3)	0.473690(16)	0.17546(3)	1	0.00894(8)
Gd9	8*h*	0.73377(3)	0.720426(17)	0.26051(3)	1	0.01068(8)
Gd10	8*h*	0.42987(3)	0.884470(17)	0.25974(3)	1	0.00924(8)
Gd11	4*g*	0.93660(14)	0.14080(7)	0	0.770(4)	0.0118(3)
Gd11'	4*g*	0.9328(5)	0.1252(2)	0	0.230(4)	0.0118(3)
Ru1	8*h*	0.51113(5)	0.78813(3)	0.12548(5)	1	0.00885(12)
Ru2'	4*g*	0.1317(4)	0.77393(18)	0	0.230(4)	0.0138(13)
Sn1	4*f*	0	0.5	0.36253(7)	1	0.00877(15)
Sn2	2*a*	0	0	0	1	0.0126(2)
Sn3	4*g*	0.35287(7)	0.84934(3)	0	1	0.01106(16)
Sn4	8*h*	0.83726(4)	0.92164(2)	0.12547(5)	1	0.00891(11)
Sn5	4*g*	0.34431(7)	0.73615(3)	0	1	0.01049(16)
Sn6	4*g*	0.60752(7)	0.70727(3)	0	1	0.01040(15)
Sn7	4*g*	0.62030(7)	0.44466(3)	0	1	0.01017(15)
Sn8	4*g*	0.95965(7)	0.55678(3)	0	1	0.01067(16)
Sn9	8*h*	0.67358(4)	0.59207(2)	0.26393(5)	1	0.01020(11)
Sn10	8*h*	0.67739(4)	0.84521(2)	0.23564(5)	1	0.00810(11)
Sn11	8*h*	0.9851(6)	0.7487(3)	0.8451(7)	0.770(4)	0.0098(5)
Sn11'	8*h*	0.976(2)	0.7442(11)	0.840(3)	0.230(4)	0.0098(5)
Sn12	4*g*	0.8549(6)	0.67532(16)	0	0.770(4)	0.0096(5)
Ru12'	4*g*	0.859(3)	0.6833(8)	0	0.230(4)	0.0096(5)

[a] U_{eq} is defined as 1/3 of the trace of the orthogonalized U_{ij} tensor.

´Positional and/or occupational disorder of Gd11, Sn11, and Sn12 with Gd11′, Sn11′, and Ru12′, respectively. Ru2′ occurs at the same frequency as the disordered atoms.

$Tb_{30}Ru_6Sn_{29.5}$ and $Dy_{30}Ru_{4.57}Sn_{30.72}$ are provided in Appendix Table A3.1. It should be noted that data collected from different crystals from batches (and between batches of the same

analogues) were modeled to stoichiometries within experimental error, indicating high sample homogeneity.

3.2.4 Modeling Structural Disorder

Several positionally disordered atomic sites linked to the occupancy of the Ru2′ atom were found while refining the model. A detailed explanation of the disorder modeling can be found in Appendix A3. The primed (Ru2′, Sn11′, Ru12′, and Gd11′) and non-primed (Sn11, Sn12, and Gd11) atoms listed in Table 3.2 always occur as a group. The two possible configurations of positional disorder, depending upon the existence of Ru2′, are shown in Figure 3.1. The Gd and Dy analogues display the same trend in positional disorder with occupancy

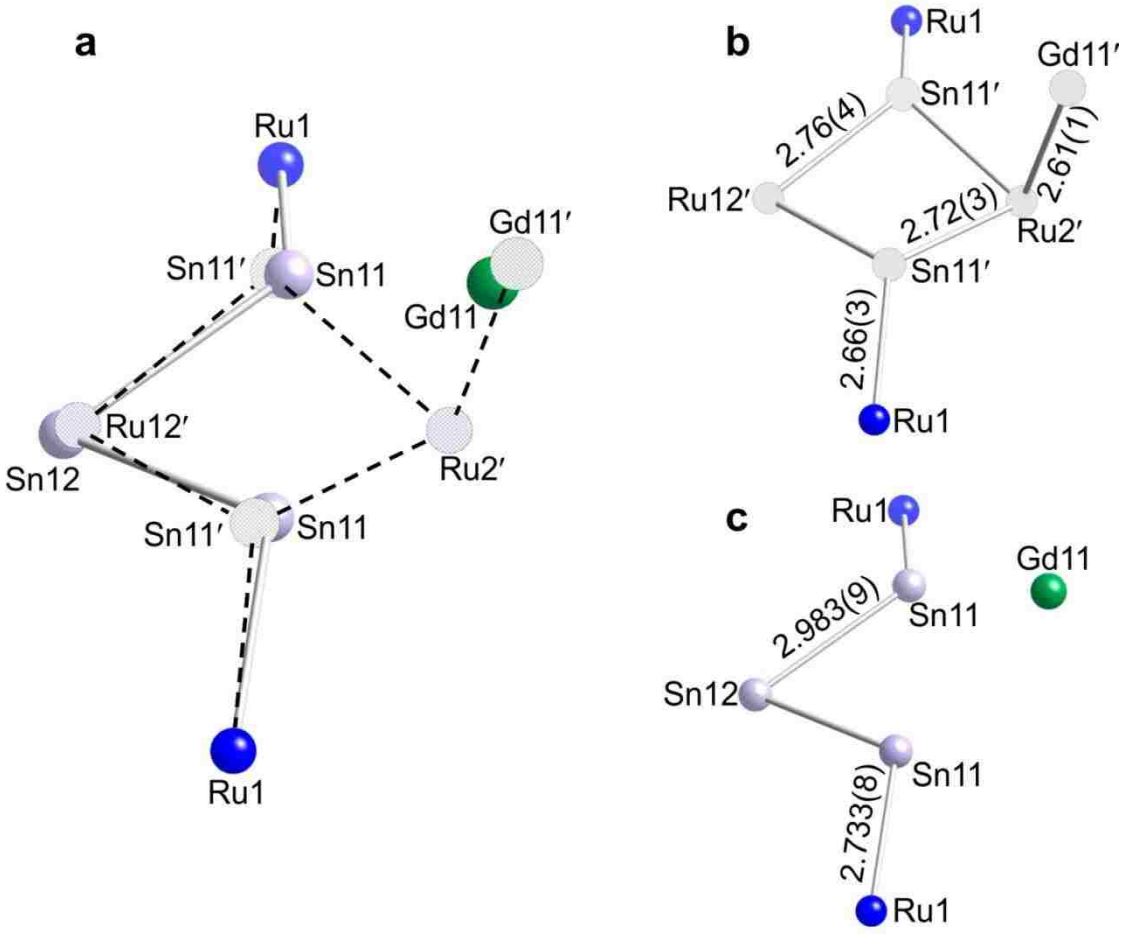

Figure 3.1. Positionally disordered model of $Gd_{30}Ru_{4.92}Sn_{30.54}$ showing (**a**) all disordered atoms, (**b**) lower occupancy disordered atoms, and (**c**) higher occupancy disordered atoms. Additional atoms adjacent to Ru12′/Sn12, Ru1, and Ru2′ have been omitted for clarity.

splitting of 77:23 and 86:14, of Sn12:Ru12′ respectively. However, the Tb analogue shows the opposite mixing ratio with 24:76 of Sn12′:Ru12, which is consistent with our elemental analysis data showing a higher Ru content in the Tb analogue relative to the Gd and Dy analogues. Additionally, there was insufficient evidence to support Sn12′/Ru12 site splitting in the Tb analogue; thus, the Sn12′/Ru12 site was modeled as a single mixed site for the Tb analogue. Atomic positions, occupancies, and atomic displacement parameters are provided in Table 3.2. The higher probability configuration of the 77:23 disordered splitting for the Gd analogue, shown in Figure 3.1c, is used for all structural modeling.

3.2.5 Physical Properties

Single crystals were oriented using single crystal X-ray diffraction prior to physical property measurements. A single crystal of $Tb_{30}Ru_6Sn_{29.5}$ was polished to a bar shape of approximately 1 × 1 × 2.5 mm^3 for resistivity and thermal conductivity measurements. Temperature and field-dependent measurements were performed using either a Quantum Design Physical Property Measurement System (PPMS) or a Quantum Design Magnetic Property Measurement System in using a comparative technique with a constantine standard, respectively. Thermal conductivity from 172–305 K was directly measured in the PPMS using a standard two-probe method.fields of 0–9 T. Temperature-dependent electrical resistivity and Seebeck coefficient were measured in the PPMS using a standard four-probe method and

3.3 Results and Discussion

3.3.1 Crystal Structure

The two basic criteria that were considered when depicting an accurate structural representation of $Gd_{30}Ru_{4.92}Sn_{30.54}$ were (1) that every atom in the structure must be represented and (2) that the bonds and the arrangement of atoms in the structure must be chemically

reasonable. As such, it was found that the interatomic forces present in the crystal structure could not be completely described as ionic (or Zintl) or covalent in nature; rather, the bonding displays both Zintl-like and covalent characteristics.

The crystal structure of $Gd_{30}Ru_{4.92}Sn_{30.54}$ is shown in Figure 3.2 and is composed of Gd-rich slabs and a Gd-poor framework in the *a*-*c* plane that stack in the *b*-direction. The Gd-poor framework shows infinite Ru–Sn and Sn–Sn bonding networks in the *a*-*c* planes and form an interpenetrating Sn net through the Gd-rich slabs. The Gd-rich slabs contain Gd surrounding

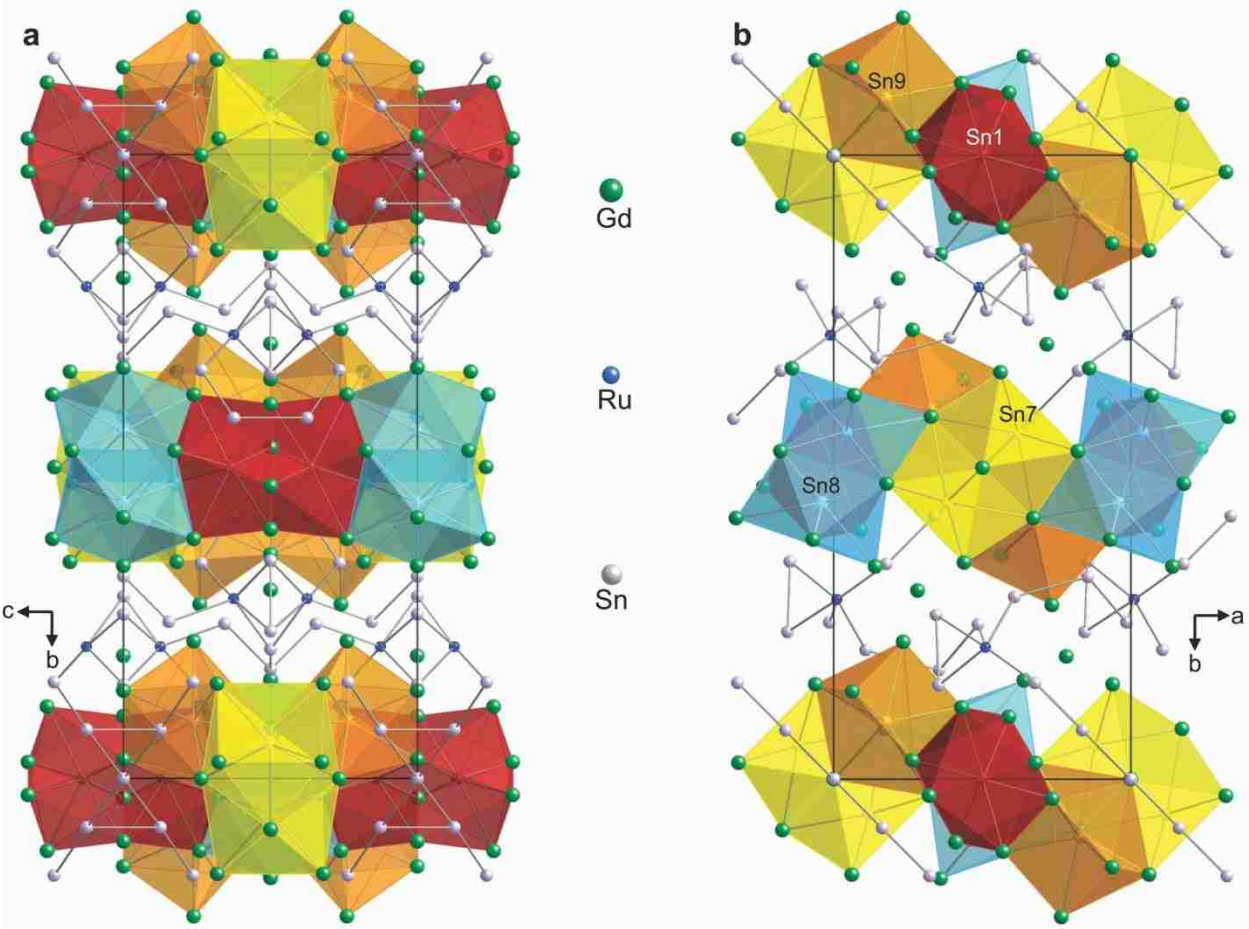

Figure 3.2. Crystal structure of $Gd_{30}Ru_{4.92}Sn_{30.54}$ shown along the (**a**) *a*-axis and (**b**) *c*-axis.

lone Sn or single-bonded dumbell Sn–Sn atoms, similar to that in $Ca_{36}Sn_{23}$[3.22] and the Zintl phases $Yb_{36}Sn_{23}$[3.23] and $Ca_{31}Sn_{20}$.[3.24, 25] We therefore adopt a Sn-centered (Sn@Gd_8) polyhedral model for the Gd-rich slabs, as they show similar features to the Zintl phases listed above. Here,

the shorthand $X@Y_z$ is used, where X is the central atom of the polyhedron, Y is the surrounding atom(s), and Z is the number of Y atoms surrounding X. The slabs and framework can be regenerated by performing a 2_1 screw-axis symmetry operation in the stacking direction (*b*-axis) at ¼ 0 ¼, a 2_1 symmetry operation along the *a*-axis at 0 ¼ ¼, or a mirror in the *c*-direction.

The Gd-poor regions, shown in Figure 3.3, contain a Ru–Sn/Sn–Sn framework. The framework can be conveniently described by a planar Sn–Sn net interpenetrating the $Sn@Gd_8$ slabs in the (120) plane, as shown in Figure 3.3a,b, and Ru1-centered bonding units propagating in the *a*-*c* plane, as shown in Figure 3.3c,d. It should be noted that (120) was the typical cleavage plane in all measured samples. The planar interpenetrating framework (Figure 3.3b) has 2-fold symmetry in the *c*-direction and is centered about Sn2. The central Sn2 is bonded to four Sn4 atoms at 3.093(1) Å, with each Sn4 atom bonded to one Sn10 at 2.961(1) Å and an adjacent Sn4 at 2.924(1) Å, all within the range of typical stannide-containing intermetallic compounds (*vide infra*). The Sn2–Sn4–Sn10 atoms form a planar web bonded to two Ru1 bonding units (one at each end of the web) with a Ru1–Sn10 (× 4) bond distance of 2.734(1) Å. The Ru1 5-coordinate environment, as shown in Figure 3.3c, consists of Sn6, Sn11, Sn10, Sn5, and Sn3 atoms with bond distances in the range of 2.724(1)–2.811(1) Å. A short Sn3–Sn5 bond distance of 2.800(1) Å is present between two Ru1 bonding units. Ru1 environments always appear in pairs parallel to the *c*-axis (Figure 3.3c,d) with a Ru–Ru interatomic distance of 2.924(1) Å. This interatomic distance is longer than typical intermetallic Ru–Ru distances of 2.57–2.79 Å[3.26-28] but similar to the sum of the Ru–Ru covalent radii (2.92 Å),[3.29] suggesting a weak Ru–Ru interaction. A Sn12 atom connects three Ru1-centered pairs, shown in Figure 3.3d, by 1 × Sn12–Sn6 (3.020(7) Å) and 2 × Sn12–Sn11 (2.983(9) Å). There are 4 + 2 nearest neighbor Ru1 pairs to a central Ru1-centered pair, four nearest neighbor Ru1 pairs (shown in

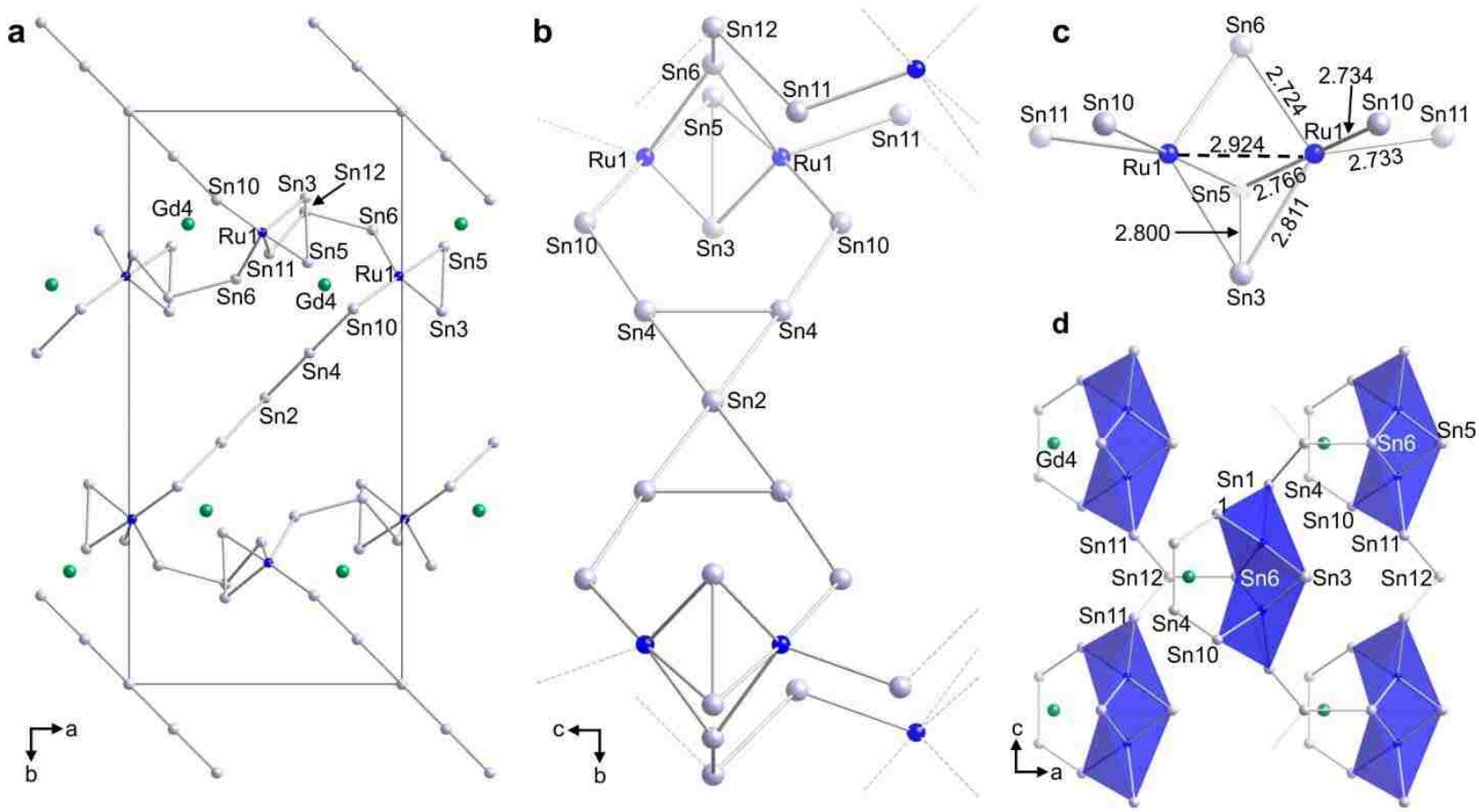

Figure 3.3. (**a**) Ru–Sn/Sn–Sn framework in $Gd_{30}Ru_{4.92}Sn_{30.54}$ shown down the *c*-axis. (**b**) Interpenetrating framework of Sn centered about Sn2. (**c**) A pair of Ru1 bonding units and (**d**) one layer of Ru1 bonding units shown down the *b*-axis. The central Ru1 bonding unit is in-plane and the four flanking bonding units are below the plane.

Figure 3.3d as polyhedra) either above or below the *a*-*c* plane and two next nearest neighbor pairs on the same *a*-*c* plane (not shown), parallel to the *c*-axis. A 14-coordinate Gd4 atom, which is unique in that it is the only rare earth situated within the Ru–Sn/Sn–Sn bonding framework, is situated between three Ru-centered pairs (Figure 3.3d). The Gd4 coordination environment is $Gd@Gd_4Sn_8Ru_2$ (not shown). The symmetry of the Ru–Sn/Sn–Sn framework can be regenerated by translating ½ in both the *a* and *c*-directions and mirroring in the *b*-direction.

The Gd-rich slabs, shown in Figure 3.4f, are composed of face-sharing (confacial) $Sn1@Gd_8$ distorted square antiprisms (Figure 3.4a), confacial $Sn8@Gd_8$ distorted square antiprisms (Figure 3.4b), confacial $Sn7@Gd_8$ square antiprisms (Figure 3.4c), and $Sn9@Gd_8$ bicapped trigonal prisms (Figure 3.4d). A similar Sn-centered confacial square antiprismatic arrangement is found in the Zintl phases $Yb_{36}Sn_{23}$[3.23] and $Ca_{31}Sn_{20}$.[3.24] Select Sn–Gd interatomic distances are provided in Table 3.3. Confacial Sn1, Sn7, and Sn8 polyhedra will herein be described as single units. The polyhedra-containing slabs form sheets from two alternating units when viewed in the *c*-direction, shown in Figure 3.4e, which extend infinitely in the *a*-*c* plane.

The first unit is composed of confacial Sn7 polyhedra which are triangular face sharing with four Sn9 polyhedra in a square planar configuration along the confacial equatorial plane of the two Sn7 polyhedra. These units are connected along the *c*-direction with edge-sharing Sn9 polyhedra (× 4) by two adjacent units which form gaps shown in Figure 3.4f, allowing the Ru–Sn/Sn–Sn framework to penetrate between slabs. The second unit is constructed of confacial Sn1 polyhedra which are triangular face sharing (× 4) with two sets of axially oriented confacial Sn8 polyhedra. The confacial plane of the Sn1 polyhedral units connects these units in the *c*-direction. The two sheets of alternating units are bridged by the Sn1 and Sn8 polyhedra of the second alternating unit. Confacial Sn1 polyhedra link the sheets by triangular face sharing (× 4)

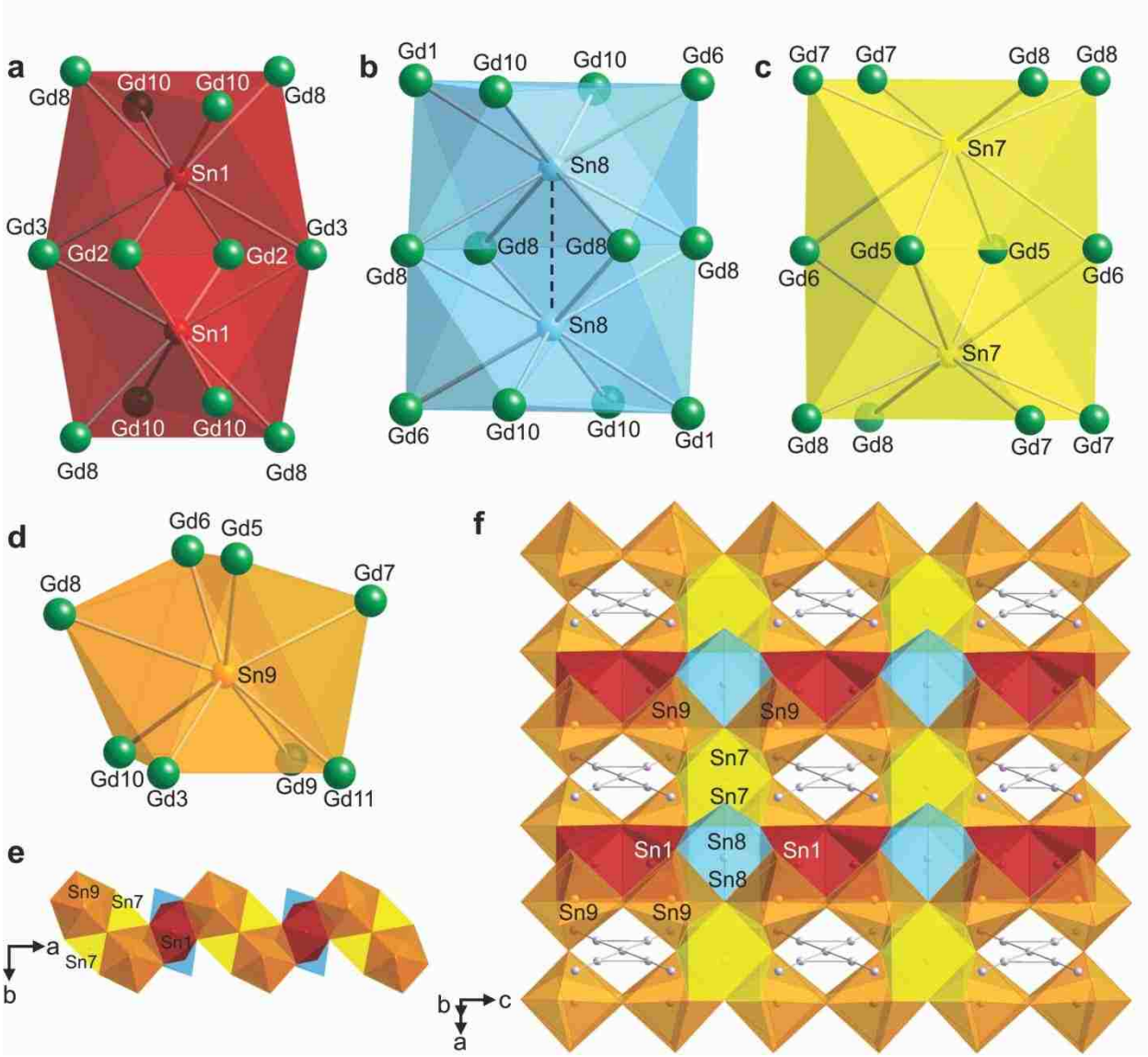

Figure 3.4. Sn@Gd_8 polyhedral units showing (**a**) Sn1@Gd_8 confacial distorted square antiprisms, (**b**) Sn8@Gd_8 confacial distorted square antiprisms, (**c**) Sn7@Gd_8 confacial square antiprisms, and a (**d**) Sn9@Gd_8 bicapped trigonal prism. The Sn12 atoms situated above and below the Sn8 polyhedra are omitted for clarity. (**e**) Zig-zag chain of Sn@Gd_8 polyhedra shown down the *c*-axis. (**f**) Plane of Sn@Gd_8 polyhedra with interpenetrating framework (Gd atoms and Sn–Gd bonds are omitted in **e** and **f** for clarity).

with four Sn9 polyhedra and corner sharing (× 4) with four Sn7 polyhedron. Sn8 confacial polyhedra bridge the sheets by triangular face sharing (× 4) with four Sn9 polyhedra and by triangular face sharing (× 2) with two sets of Sn7 confacial polyhedra. A more detailed description of the polyhedral environments can be found in Appendix A3.

Table 3.3. Interatomic distances of the Sn1, Sn7, Sn8, and Sn9-centered polyhedra

$Gd_{30}Ru_{4.92}Sn_{30.54}$		$Tb_{30}Ru_{6.0}Sn_{29.5}$		$Dy_{30}Ru_{4.57}Sn_{30.7}$	
Sn1 – Gd8 (× 2)	3.104(1)	Sn1 – Tb8 (× 2)	3.087(1)	Sn1 – Dy8 (× 2)	3.068(1)
Sn1 – Gd2 (× 2)	3.140(1)	Sn1 – Tb2 (× 2)	3.141(1)	Sn1 – Dy2 (× 2)	3.115(1)
Sn1 – Gd3 (× 2)	3.293(1)	Sn1 – Tb3 (× 2)	3.259(1)	Sn1 – Dy3 (× 2)	3.265(1)
Sn1 – Gd10 (× 2)	3.296(1)	Sn1 – Tb10 (× 2)	3.316(1)	Sn1 – Dy10 (× 2)	3.247(1)
Sn1 – Sn1	3.203(2)	Sn1 – Sn1	3.168(2)	Sn1 – Sn1	3.211(2)
Sn7 – Gd8 (× 2)	3.205(1)	Sn7 – Tb8 (× 2)	3.184(1)	Sn7 – Dy8 (× 2)	3.168(1)
Sn7 – Gd7 (× 2)	3.270(1)	Sn7 – Tb7 (× 2)	3.253(1)	Sn7 – Dy7 (× 2)	3.235(1)
Sn7 – Gd5 (× 2)	3.367(1)	Sn7 – Tb5 (× 2)	3.337(1)	Sn7 – Dy5 (× 2)	3.333(1)
Sn7 – Gd6	3.427(1)	Sn7 – Tb6	3.426(1)	Sn7 – Dy6	3.370(1)
Sn7 – Gd6	3.504(1)	Sn7 – Tb6	3.516(1)	Sn7 – Dy6	3.456(1)
Sn8 – Gd10 (× 2)	3.173(1)	Sn8 – Tb10 (× 2)	3.123(1)	Sn8 – Dy10 (× 2)	3.149(1)
Sn8 – Gd1	3.301(1)	Sn8 – Tb1	3.231(1)	Sn8 – Dy1	3.257(1)
Sn8 – Gd8 (× 2)	3.328(1)	Sn8 – Tb8 (× 2)	3.317(1)	Sn8 – Dy8 (× 2)	3.281(1)
Sn8 – Gd8 (× 2)	3.383(1)	Sn8 – Tb8 (× 2)	3.390(1)	Sn8 – Dy8 (× 2)	3.353(1)
Sn8 – Gd6	3.441(1)	Sn8 – Tb6	3.347(1)	Sn8 – Dy6	3.411(1)
Sn8 – Sn8	2.964(2)	Sn8 – Sn8	3.038(1)	Sn8 – Sn8	2.930(2)
Sn8 – Sn12	3.179(5)	Sn8 – Ru12	3.100(1)	Sn8 – Sn12	3.174(8)
Sn9 – Gd5	3.079(1)	Sn9 – Tb5	3.0561)	Sn9 – Dy5	3.0521)
Sn9 – Gd6	3.087(1)	Sn9 – Tb6	3.076(1)	Sn9 – Dy6	3.060(1)
Sn9 – Gd10	3.088(1)	Sn9 – Tb10	3.069(1)	Sn9 – Dy10	3.056(1)
Sn9 – Gd9	3.251(1)	Sn9 – Tb9	3.227(1)	Sn9 – Dy9	3.217(1)
Sn9 – Gd11	3.271(2)	Sn9 – Tb11	3.250(1)	Sn9 – Dy11	3.238(1)
Sn9 – Gd7	3.287(1)	Sn9 – Tb7	3.266(1)	Sn9 – Dy7	3.248(1)
Sn9 – Gd3	3.319(1)	Sn9 – Tb3	3.286(2)	Sn9 – Dy3	3.305(1)
Sn9 – Gd8	3.554(1)	Sn9 – Tb8	3.517(1)	Sn9 – Dy8	3.518(1)

3.3.2 Stannide Bonding

Differentiation of the Sn environments in the Ru–Sn/Sn–Sn framework and in the Gd-rich slabs was conducted by carefully examining the Sn–Sn interatomic distances and the general coordination environments of each Sn atom. The Sn–Sn interatomic distances can be grouped into those with shorter interatomic distances (2.800–3.093 Å) and those with interatomic contacts > 3.1 Å. The Sn3–Sn5 bond distance of 2.800(1) represents the shortest Sn–Sn interatomic distance, similar to that of elemental α-Sn (2.810 Å),[3.30] indicating strong Sn–Sn bonding interactions. The additional Sn–Sn bonds (2.924–3.093 Å) fall within the range of 2.819–3.117 Å for Sn–Sn contacts in the polar intermetallic compounds $Yb_4Mn_2Sn_5$ and Yb_3CoSn_6,[3.31] the strongly bonded Sn–Sn zig-zag chains in Gd_4RuSn_8,[3.32] and the short Sn–Sn distances in

Ru_3Sn_7.[3.33] The Sn atoms with Sn–Sn nearest interatomic distances > 3.1 Å (Sn1, Sn7, and Sn9) and those which form singular dimers (Sn8) constitute the second Sn environment. These Sn atoms are all coordinated by 8 Gd atoms. The Sn8–Sn8 interatomic distance of 2.964(2) Å corresponds well to the Sn–Sn dimer distances in the Zintl phases Li_7Sn_2 (2.999(7) Å)[3.34] and $Ca_{31}Sn_{20}$ (3.158(2) Å).[3.24] The nearest Sn–Sn interatomic distances of Sn1, Sn7 and Sn9 are all > 3.17 Å, and the Sn@Gd_8 square antiprismatic environments are similar to those of the isolated Sn atoms in the Zintl phases $Ca_{31}Sn_{20}$[3.24] and $La_4Ge_{3,}$[3.35] where isolated $(Ge/Sn)^{4-}$ and dimer $(Ge/Sn)_2^{6-}$ anions are surrounded by Ca and La cations, respectively. Thus, the Sn1, Sn7, Sn8, and Sn9 atoms of the title compounds likely carry some anionic character. The Sn8 atom, therefore, should be considered as a 1b–Sn^{3-} anion, and the Sn1, Sn7 and Sn9 atoms as 0b–Sn^{4-} anions. An interesting note regarding the confacial Sn-centered polyhedra is that the Sn8–Sn8 and Sn1–Sn1 distances of the Gd and Dy analogues (Table 3.3) are similar to one another, and those of the Tb analogue are longer (by ~0.09 Å) and shorter (by ~0.04 Å) than the Gd and Dy analogues, respectively, suggesting a change in bonding character of the Tb analogue relative to those of Gd and Dy.

3.3.3 Magnetization

Temperature-dependent magnetic susceptibility data with $H \,//\, a$, b, and c-directions are shown in Figures 5 and 6. Zero-field-cooled (ZFC) and field-cooled (FC) data were taken with $H \,//\, a$, b, and c in $Gd_{30}Ru_{4.92}Sn_{30.54}$ (Appendix Figure A3.1) and $H \,//\, a$ in $Tb_{30}Ru_6Sn_{29.5}$ to test for ZFC and FC divergence, indicative of ferromagnetic (FM) ordering, due to the large increase in susceptibility in these directions. Curie temperatures (T_C) are determined by the local minimum in the first derivative of magnetic susceptibility ($d\chi/dT$) as a function of temperature (Appendix Figure A3.1d).

Figure 3.5a shows the temperature-dependent magnetic susceptibility data of single crystal $Gd_{30}Ru_{4.92}Sn_{30.54}$ with H = 0.1 T // a, b, and c. $Gd_{30}Ru_{4.92}Sn_{30.54}$ displays a complex anisotropic magnetic behavior with a minimum of four temperature-dependent magnetic

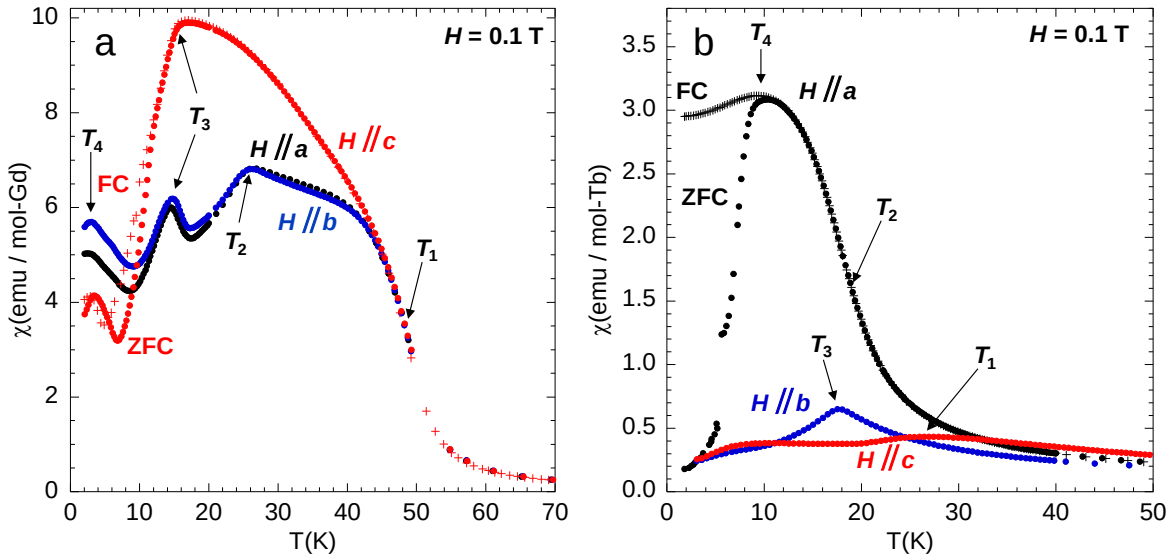

Figure 3.5. Temperature-dependent magnetic susceptibility of (**a**) $Gd_{30}Ru_{4.92}Sn_{30.54}$ from 2–70 K and of (**b**) $Tb_{30}Ru_6Sn_{29.5}$ from 2–50 K in an applied field of 0.1 T with H //a, b, c shown in black, blue, and red, respectively. FC and ZFC data are shown with H //c for $Gd_{30}Ru_{4.92}Sn_{30.54}$ and with H //a for $Tb_{30}Ru_6Sn_{29.5}$. ZFC data are shown in the remaining directions. Arrows highlight the magnetic transition temperatures.

transitions from 49 K to 3.5 K. A large increase in susceptibility is observed starting at 52 K in all three applied field directions. A small divergence in the ZFC and FC data is observed ~42 K with H //a (Appendix Figure A3.1a), indicating ferromagnetic ordering with T_1 = 49 K. However, only ~1 μ_B/Gd is observed at the apparent saturation point at 42 K (calculated by normalizing the temperature-dependent FC magnetization value to μ_B/Gd), suggesting a FM sublattice involving ~15 % of the Gd positions. It is worth noting that a broad feature in susceptibility, which occurs only with H //c beginning at 40 K with a maximum at 17 K, is likely a spin re-orientation. The first antiferromagnetic (AFM) transition is apparent with H //a and b at T_2 = 26 K, and the second AFM transition occurs with H //a, b, and c at T_3 ~ 15 K. At 9

K and 5.5 K, the magnitude of the FC data (Appendix Figure A3.1) drops below that of the ZFC data with H //b and c, respectively. Additionally, in all measured directions the magnitude of the susceptibility drops below that of the FM ordering at T_1, and a thermal hysteresis appears in the ZFC and FC minima, indicating a reorientation of the FM sublattices. The reorientation of the FM sublattices concomitant with the anomalous ZFC/FC behavior in both the Gd and Tb (*vide infra*) analogues may indicate a low-temperature structural transition. Another slope change is apparent with H // b and c, indicating a final AFM transition at T_4 = 3.5 K.

It is interesting that the field-dependent magnetization with H //a, b, and c at 3 K, shown in Appendix Figure A3.2, appears isotropic and displays no hysteretic behavior. In all directions field-dependent magnetization saturates at ~1.9 μ_B/Gd at 0.4 T, followed by a linear field dependence up to 9 T, suggesting an isotropic soft ferromagnetic sublattice and a paramagnetic (PM) sublattice, respectively.

Figure 3.5b shows the temperature-dependent magnetic susceptibility data of single crystal $Tb_{30}Ru_{46}Sn_{29.5}$ with H = 0.1 T // a, b, and c. $Tb_{30}Ru_{46}Sn_{29.5}$ also displays complex anisotropic magnetic ordering with four distinct ordering temperatures. An antiferromagnetic transition occurs with H //c at T_1 = 26.5 K, followed by a second AFM transition with H //b at T_3 = 17.5 K. A large increase in susceptibility occurs with H //a beginning at 24 K, and a divergence occurs in the ZFC and FC data at 11.5 K, indicating ferromagnetic ordering with T_2 = 19 K. A magnetic moment of 0.56 μ_B/Tb is observed at the maximum value of the temperature-dependent FC susceptibility with H //a, suggesting the FM sublattice at T_2 involves only ~6 % of the total Tb moment. A maximum occurs in the ZFC and FC data with H //a, indicating an AFM transition at T_4 = 10 K, accompanied by a sharp drop in the ZFC data, similar to that of the Gd analogue, suggesting a reordering of the FM sublattice. This behavior may be caused by a

low-temperature structural transition, as suggested with the Gd analogue, or a spin-reorientation. Further measurements are in progress to ascertain the origin of this anomaly.

The field-dependent magnetization of $Tb_{30}Ru_6Sn_{29.5}$ at 3 K with H //a, b, and c is shown in Appendix Figure A3.3. All three directions display field-dependent hysteresis; however, the hysteresis loops with H //b and c are elongated in field, whereas the loop with H //a displays hysteresis characteristics of a typical ferromagnetic sublattice with a coercive field of 0.35 T. The remnant magnetization with H //a is 0.55 μ_B/Tb, far from the theoretical saturated magnetization value 9.72 μ_B/Tb. This suggests that ~6 % of the Tb sites are involved in the ferromagnetic sublattice, similar to the value determined from the maximum in the temperature-dependent magnetization. At fields higher than the convergence in the hysteresis loops in all applied field directions, the field-dependent magnetization becomes linear up to 9 T, suggesting the coexistence of ferromagnetic and paramagnetic sublattices at 3 K.

Temperature-dependent magnetic susceptibility data were fit with the modified Curie-Weiss (MCW) equation $\chi = \chi_o + C / (T - \theta_{CW})$, where χ_o is the temperature independent contribution to the susceptibility, C is the Curie constant, and θ_{CW} is the Curie-Weiss temperature. Data were fit according to the criteria below. The inverse susceptibility of the Gd analogue in all directions shows nonlinearity below 173 K (H //a) and ~148 K (H //b, c). Nonlinearity is also present in the inverse susceptibility of the Tb analogue below ~199 K (H //a) and ~92 K (H //b, c); thus, data were fit above these temperatures. FC data were fit where available as the inverse susceptibility of these data deviated less from linearity than the ZFC data. Values of μ_{eff}, χ_o, and θ_{CW}, as well as fit ranges, are shown in Tables 3.4,5.

The μ_{eff} values obtained from the MCW fits are close to the theoretical values of 7.94 μ_B/Gd and 9.72 μ_B/Tb. The χ_o values from the fits are all small and positive, consistent with a

small Pauli paramagnetic contribution from itinerant electrons in a low resistivity material. The θ_{CW} temperatures in the Gd analogue, as determined from the fits, are all positive, suggesting dominant ferromagnetic correlations. Although it is clear that multiple magnetic sublattices are present in $Gd_{30}Ru_{4.92}Sn_{30.54}$, the ferromagnetic sublattice appears to be the most energetically favorable as T_{C1} ~ 49 K with H //a, b, and c. The θ_{CW} temperatures of $Tb_{30}Ru_6Sn_{29.5}$ from the fit show a high degree of anisotropy with field direction. The negative θ_{CW} temperatures with H //a and b are consistent with the antiferromagnetic ordering observed in these directions, though FM characteristics are also observed with H //a in the temperature and field-dependent magnetization but only correspond to a small percentage of the total Tb moment. The fitted θ_{CW} temperature with H //c, however, is positive, while the temperature-dependent magnetization clearly shows AFM ordering with no indication of ferromagnetism. The Tb atoms in $Tb_{30}Ru_4Sn_{29.5}$ all have low site symmetry, and similar anisotropic θ_{CW} behavior has been observed in $Nd_2Ti_2O_7$ and attributed to contributions from crystal electric field effects due to the low Nd site symmetry.[3.36] Thus, the observed anisotropic θ_{CW} temperatures may be CEF mediated.

Table 3.4. Curie Weiss law fit values of μ_{eff}, χ_o, and θ_{CW} and fit ranges for $Gd_{30}Ru_{4.92}Sn_{30.54}$

$Gd_{30}Ru_{4.92}Sn_{30.54}$	H //a	H //b	H //c
χ_0 (10^{-3} emu/mol-Ln)	1.1(8)	0.96(4)	0.26(4)
θ_{CW} (K)	21(4)	26(2)	25(2)
μ_{eff} (μ_B/Ln)	7.9(2)	7.81(7)	7.86(8)
Fit range (K)	174–296	149–290	158–296

Table 3.5. Curie Weiss law fit values of μ_{eff}, χ_o, and θ_{CW} and fit ranges for $Tb_{30}Ru_6Sn_{29.5}$

$Tb_{30}Ru_6Sn_{29.5}$	H //a	H //b	H //c
χ_0 (10^{-3} emu/mol-Ln)	0.7(4)	5.7(3)	4.6(2)
θ_{CW} (K)	-5.7(3)	-9.1(7)	10.3(3)
μ_{eff} (μ_B/Ln)	9.58(1)	9.44(4)	9.88(3)
Fit range (K)	200–390	93–290	96–285

3.3.4 Resistivity

Figure 3.6 shows electrical transport of single crystals of $Gd_{30}Ru_{4.92}Sn_{30.54}$ and $Tb_{30}Ru_6Sn_{29.5}$ as a function of temperature from 2–350 K with the current (*i*) // *b* and *c*. Oriented single crystals of the Gd analogue were irregularly shaped; hence, resistivity normalized to the resistivity at 2 K (ρ/ρ_{2K}) is shown in Figure 3.6a. However, single crystals of the Tb analogue were large enough to polish to a bar shape with an estimated error in the resistivity due to geometric considerations with *i* // *b* and *c* of < 20 % and < 10 %, respectively. The resistivity (ρ) of two crystals of the Tb analogue was measured, which produced similar results; thus, ρ data for the crystal selected for thermal transport measurements are shown in Figure 3.6b. Warming (solid circles) and cooling (crosses) cycles are shown for both analogues.

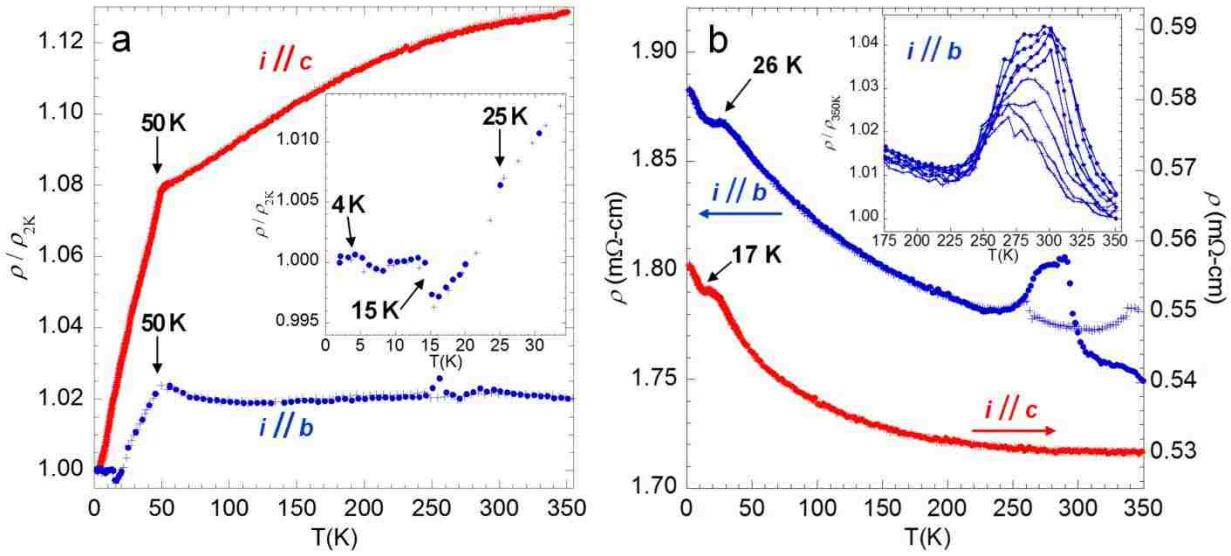

Figure 3.6. Temperature-dependent (**a**) resistivity of $Gd_{30}Ru_{4.92}Sn_{30.54}$ normalized to the resistivity at 2 K and (**b**) electrical resistivity of $Tb_{30}Ru_6Sn_{29.5}$ from 2–350 K with *i* // *b* (blue) and *c* (red). Arrows highlight anomalies in the electrical resistivity. The inset of (**a**) shows the low-temperature electrical resistivity of $Gd_{30}Ru_{4.92}Sn_{30.54}$ with *i* // *b*, and the inset of (**b**) highlights the anomaly centered at ~280 K of a second crystal of $Tb_{30}Ru_6Sn_{29.5}$ with *i* // *b*, normalized to the resistivity at 350 K.

$Gd_{30}Ru_{4.92}Sn_{30.54}$ and $Tb_{30}Ru_6Sn_{29.5}$ display a large degree of electric transport anisotropy in the form of temperature-dependent behavior and absolute magnitude, respectively. Above the

magnetic ordering temperatures, the temperature-dependent curve of $Gd_{30}Ru_{4.92}Sn_{30.54}$ with $i // c$ exhibits characteristics of a poor metal up to ~350 K, while the curve with $i // b$ displays semiconducting-like, nearly temperature independent behavior. While $Tb_{30}Ru_6Sn_{29.5}$ exhibits semiconducting-like behavior in both directions, the change in resistivity from 2 K to 350 K is -7.63 % with $i // b$ and -4.72 % with $i // c$. Therefore, the temperature dependence of both analogues consistently displays more pronounced semiconducting behavior with $i // b$ relative to $i // c$. The low-temperature resistivity data for $Gd_{30}Ru_{4.92}Sn_{30.54}$ (highlighted in Figure 3.6a, inset) shows slope changes at 50 K, 25 K, 15 K, and 4 K, while $Tb_{30}Ru_6Sn_{29.5}$ (highlighted in Figure 3.6b) displays slope changes at 26 K, and 17 K. These data correspond well to the magnetic ordering temperatures found from the temperature-dependent susceptibility data and are likely due to a reduction of spin-disorder scattering from the ordered magnetic moments. An anomaly with $i // b$ is observed in the high temperature resistivity of the Tb analogue centered at ~275 K. It is worth noting that a small anomaly is also present in the electrical resistivity of $Gd_{30}Ru_{4.92}Sn_{30.54}$ with $i // b$, centered at ~255 K. To ascertain whether the anomaly in $Tb_{30}Ru_6Sn_{29.5}$ is intrinsic to the material, the resistance of another single crystal of $Tb_{30}Ru_6Sn_{29.5}$ was swept from low-temperature to high temperature and back several times and is shown in the inset of Figure 3.6b as resistivity normalized to the resistivity at 350 K. The results show that the anomaly is intrinsic. While the origin of this anomaly is still under investigation, it may be linked to the magnetism of the material, as the inverse susceptibility of $Tb_{30}Ru_6Sn_{29.5}$ deviates from linearity at high temperatures (~200 K) relative to the highest magnetic ordering temperature observed at T_1 = 26.5 K.

The temperature-dependent resistivity data of $Tb_{30}Ru_6Sn_{29.5}$ with $i // b$ and c show semiconducting-like behavior with largely different magnitudes. The room temperature

resistivity values are 1.77 mΩ•cm and 0.53 mΩ•cm with $i \parallel b$ and c, respectively; therefore, the resistivity anisotropy (ρ_b/ρ_c) is 3.34 at 300 K. Bulk three dimensional (3-D) solids typically display low resistivity anisotropy of ~1, but some exceptions are present in the literature, such as the high temperature Kondo systems URu_2Si_2 and $CePt_2In_7$ with resistivity anisotropies of ~1.94 and ~3.3, respectively, at 300 K,[3.13, 14] and the open 3-D framework $CaFe_4As_3$ shows a room temperature anisotropic resistivity ~1.3.[3.16] Quasicrystalline approximant phases, such as *T*-$Al_{72.5}Mn_{21.5}Fe_{6.0}$ and *d*-Al-Co-Ni, have been shown to exhibit resistivity anisotropies of 1.23 and 8.4, respectively.[3.11, 12] On the other hand, 2D materials have been shown to exhibit very high resistivity anisotropy, such as the layered superconductor $BaFe_2As_2$ with ρ_c/ρ_{ab} ~ 150.[3.15] Thus, with ρ_b/ρ_c = 3.34, $Tb_{30}Ru_6Sn_{29.5}$ displays one of the highest anisotropic resistivity values ever reported in a 3-D extended solid system.

3.3.5 Thermopower

Figure 3.7a shows the thermopower as a function of temperature of $Tb_{30}Ru_6Sn_{29.5}$ with $\Delta T \parallel b$ and c from 10–350 K. Both directions show positive thermopower at 300 K with a positive temperature dependence. The thermopower with $\Delta T \parallel c$ is slightly negative from 10–60 K with a negative temperature coefficient, and then becomes positive with a positive temperature coefficient above 60 K, indicating a mixture of n- and p-type charge carriers. The thermopower with $\Delta T \parallel b$ is positive across the entire measured temperature range with a positive temperature coefficient, indicating dominant p-type carrier conduction. There is an anomaly with $\Delta T \parallel b$ centered at ~270 K, which corresponds to an anomaly in the electrical resistivity with $i \parallel b$; however, there is no evidence of the anomaly in the thermopower data with $\Delta T \parallel c$, which mirrors the behavior of the electrical resistivity data. The slopes of the temperature dependence of the thermopower are clearly different in the two measured directions, and the two temperature-

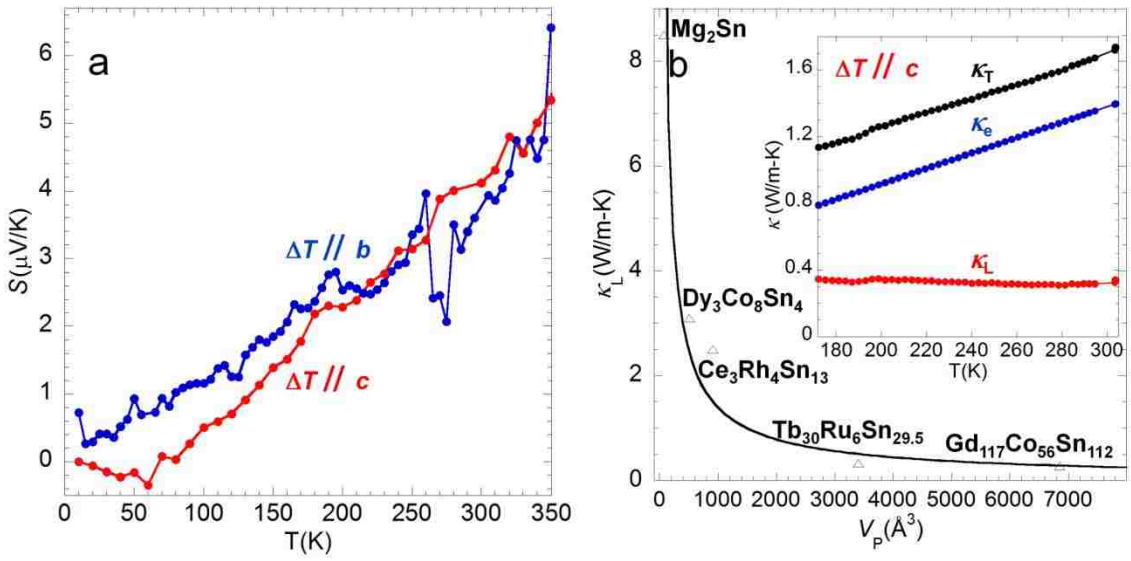

Figure 3.7. (**a**) Temperature-dependent thermopower of $Tb_{30}Ru_6Sn_{29.5}$ from 10–350 K with i // b (blue) and c (red), and (**b**) primitive volume (V_P) dependent lattice thermal conductivity of various stannides fit to a power law. Lattice thermal conductivity data for Mg_2Sn, $Dy_3Co_8Sn_4$, $Ce_3Rh_4Sn_{13}$, and $Gd_{117}Co_{56}Sn_{112}$ are obtained from Ref. [3.37], [3.38], [3.39], and [3.17], respectively. **b, inset** shows temperature-dependent total (black), electronic (blue), and lattice (red) thermal conductivity of $Tb_{30}Ru_6Sn_{29.5}$ from 172–305 K with ΔT // c.

dependent curves cross at ~250 K, indicating that the thermopower also displays anisotropic behavior. This suggests that the electronic structure is highly anisotropic and the difference in magnitude of the electrical resistivity is likely due to a highly anisotropic Fermi surface similar to $PdCoO_2$[3.40] rather than the anisotropic quenched defect scattering mechanism dominant in the quasicrystalline approximant T-$Al_{72.5}Mn_{21.5}Fe_{6.0}$.[3.11]

3.3.6 Thermal Conductivity

The inset of Figure 3.7b shows the total (κ_T), electronic (κ_e), and lattice (κ_L) thermal conductivity as a function of temperature of $Tb_{30}Ru_6Sn_{29.5}$ with ΔT // c from 172–305 K. κ_e is calculated using the Wiedemann-Franz law $\kappa_e = L_o T/\rho$, where $L_o = 2.44 \times 10^{-8}$ W•Ω/K^2 is the Lorenz number and ρ is the electrical resistivity obtained from the same crystal with i // c. The lattice thermal conductivity is calculated using $\kappa_T = \kappa_L + \kappa_e$. κ_T steadily increases over the entire measured temperature range, while κ_L decreases as a function of temperature as expected. The

lattice thermal conductivity of $Tb_{30}Ru_6Sn_{29.5}$ at 300 K is exceptionally low with κ_L = 0.33 W/m•K. The low room temperature κ_L value of $Tb_{30}Ru_6Sn_{29.5}$ can be explained by the sizeable volume of the primitive unit cell. Reduction of lattice thermal conductivity as a function of primitive unit cell volume (V_P) in systems with similar average atomic mass and bonding characteristics is a well-documented phenomenon, both theoretically[3.41] and experimentally,[3.42] which typically scales as ~$1/V_P$. Figure 3.7 shows the room temperature κ_L values of $Tb_{30}Ru_6Sn_{29.5}$ and other stannides as a function of V_P. Similar to a study conducted on complex antimonides,[3.42] the data are fit to a power law of $\kappa_L = 415 \cdot V_P^{-0.82}$. The room temperature κ_L value of $Tb_{30}Ru_6Sn_{29.5}$ is clearly situated below the curve fit. The deviation of $Tb_{30}Ru_6Sn_{29.5}$ from the fit may be due to the large degree of disorder modeled in the system, which has been shown to significantly lower lattice thermal conductivity.[3.41] The observation of such a low lattice thermal conductivity in $Tb_{30}Ru_6Sn_{29.5}$, concomitant with the highly anisotropic nature of the electrical resistivity, introduces the potential of highly anisotropic thermal conductivity. Though our sample was not large enough for anisotropic thermal conductivity measurements, the anisotropic thermal conductivity can be estimated using the anisotropic resistivity values and assuming an isotropic κ_L. At room temperature $\kappa_T \,//\, c$ is 1.7 W/m•K, and a simple calculation yields $\kappa_T \,//\, b$ of 0.74 W/m•K, with a theoretical thermal transport anisotropy of ~2.4.

3.4 Conclusions

$Gd_{30}Ru_{4.92}Sn_{30.54}$, $Tb_{30}Ru_6Sn_{29.5}$, and $Dy_{30}Ru_{4.57}Sn_{30.72}$ adopt a new structure type with 24 atomic positions and a large V_P. The structure of $Gd_{30}Ru_{4.92}Sn_{30.54}$ consists of a unique combination of slabs of $Sn@Gd_8$ polyhedra and an interpenetrating Sn-based framework. The slabs and framework are considered to be more ionic and covalent in nature, respectively. Furthermore, disorder was modeled in the system with two independent scenarios based on the

presence or absence of the Ru2' position. This disorder may affect the physical properties observed in the system.

$Gd_{30}Ru_{4.92}Sn_{30.54}$ and $Tb_{30}Ru_6Sn_{29.5}$ both display highly anisotropic magnetic and transport properties. The temperature-dependent magnetism fits a modified Curie Weiss law with the fit magnetic moments corresponding well to the expected moments for Gd and Tb in all measured directions. The temperature-dependent magnetism also shows anisotropic low-temperature behavior with at least four magnetic transitions in $Gd_{30}Ru_{4.92}Sn_{30.54}$ and four magnetic transitions in $Tb_{30}Ru_6Sn_{29.5}$. Field-dependent magnetism taken at 3 K suggests the presence of a ferromagnetic sublattice in both analogues. The electrical resistivity of $Gd_{30}Ru_{4.92}Sn_{30.54}$ and $Tb_{30}Ru_6Sn_{29.5}$ is highly anisotropic with an anisotropic resistivity ratio of 3.34 in $Tb_{30}Ru_6Sn_{29.5}$, one of the largest ever reported in a 3-D extended solid. It is possible that the 2-D-like $Sn@Gd_8$ slabs contribute to the observed electrical characteristics; further detailed studies of the material will be necessary to determine the nature of the electrical anisotropy. The presence of an anomaly at ~275 K in both the electrical resistivity and thermopower of $Tb_{30}Ru_6Sn_{29.5}$ with i and $S \mathbin{/\!/} b$, and the absence of this anomaly with i and $S \mathbin{/\!/} c$, confirms its intrinsic and highly anisotropic nature. Additionally, the differing slope changes and general features of the thermopower between $S \mathbin{/\!/} b$ and c imply that the anisotropic electrical characteristics are a result of a highly anisotropic Fermi surface; though, a small contribution from anisotropic quenched defect scattering is likely present due to the large degree of disorder present in the system.

The thermal conductivity of $Tb_{30}Ru_6Sn_{29.5}$ is low and dominated by the κ_e in the measured temperature range. The calculated κ_L of 0.33 W/m•K at 300 K is compared to other Sn-containing systems with various primitive lattice volumes. A theoretical anisotropic thermal conductivity ratio of 2.4 is calculated from the electrical resistivity data. This system displays a

rare mixture of highly anisotropic and complex magnetism and transport properties certainly deserving future study. The anisotropic electrical and thermal properties may prove to be useful in technological applications where preferential thermal transport properties are desired, while the low-temperature magnetic phenomena observed may have magnetocaloric applications.

The title compounds exhibit a complex structure with concomitant complex properties, which were only discovered through careful structural characterization, post-growth sample preparation, and a meticulous transfer of the structural orientation information to physical property measurement and analysis. We have presented an overview of $Ln_{30}Ru_{4+x}Sn_{31-x}$ (Ln = Gd and Tb), which crystallizes in a new structure-type and displays anisotropic magnetic and electrical properties, but further detailed magnetic and electrical characterization will be necessary to fully understand these phenomena. Materials displaying exotic properties are paving the way for new technologies such as spintronics and magnetocalorics. Only with a thorough understanding of the structure-property relationships in complex systems will we be able to tune the properties of these materials in order to exploit them for application purposes.

3.5 References

3.1. Giguere, A.; Foldeaki, M.; Gopal, B. R.; Chahine, R.; Bose, T. K.; Frydman, A.; Barclay, J. A., *Phys. Rev. Lett.* **1999,** *83*, 2262-2265.

3.2. Canfield, P. C.; Bud'ko, S. L., *Sci. Am.* **2005,** *292*, 80-87.

3.3. Rotter, M.; Tegel, M.; Johrendt, D., *Phys. Rev. Lett.* **2008,** *101*, 1-4.

3.4. Phelan, W. A.; Menard, M. C.; Kangas, M. J.; McCandless, G. T.; Drake, B. L.; Chan, J. Y., *Chem. Mater.* **2012,** *24*, 409-420.

3.5. Snyder, G. J.; Christensen, M.; Nishibori, E.; Caillat, T.; Iversen, B. B., *Nat. Mater.* **2004,** *3*, 458-463.

3.6. Brown, S. R.; Kauzlarich, S. M.; Gascoin, F.; Snyder, G. J., *Chem. Mater.* **2006,** *18*, 1873-1877.

3.7. Jiang, J.; Payne, A. C.; Olmstead, M. M.; Lee, H. O.; Klavins, P.; Fisk, Z.; Kauzlarich, S. M.; Hermann, R. P.; Grandjean, F.; Long, G. J., *Inorg. Chem.* **2005,** *44*, 2189-2197.

3.8. Goforth, A. M.; Hope, H.; Condron, C. L.; Kauzlarich, S. M.; Jensen, N.; Klavins, P.; MaQuilon, S.; Fisk, Z., *Chem. Mater.* **2009,** *21*, 4480-4489.

3.9. Zaharko, O.; Keller, L.; Ritter, C., *J. Magn. Magn. Mater.* **2002,** *253*, 130-139.

3.10. Kim, M. S.; Sung, N. H.; Son, Y.; Ko, M. S.; Cho, B. K., *Appl. Phys. Lett.* **2011,** *98*, 1-3.

3.11. Heggen, M.; Feuerbacher, M.; Ivkov, J.; Popcevic, P.; Batistic, I.; Smontara, A.; Jagodic, M.; Jaglicic, Z.; Janovec, J.; Wencka, M.; Dolinsek, J., *Phys. Rev. B* **2010,** *81*, 1-11.

3.12. Bobnar, M.; Jeglic, P.; Klanjsek, M.; Jaglicic, Z.; Wencka, M.; Popcevic, P.; Ivkov, J.; Stanic, D.; Smontara, A.; Gille, P.; Dolinsek, J., *Phys. Rev. B* **2012,** *85*, 1-11.

3.13. Palstra, T. T. M.; Menovsky, A. A.; Mydosh, J. A., *Phys. Rev. B* **1986,** *33*, 6527-6530.

3.14. Tobash, P. H.; Ronning, F.; Thompson, J. D.; Scott, B. L.; Moll, P. J. W.; Batlogg, B.; Bauer, E. D., *J. Phys.: Condens. Matter* **2012,** *24*, 1-7.

3.15. Wang, X. F.; Wu, T.; Wu, G.; Chen, H.; Xie, Y. L.; Ying, J. J.; Yan, Y. J.; Liu, R. H.; Chen, X. H., *Phys. Rev. Lett.* **2009,** *102*, 1-4.

3.16. Karki, A. B.; McCandless, G. T.; Stadler, S.; Xiong, Y. M.; Li, J.; Chan, J. Y.; Jin, R., *Phys. Rev. B* **2011,** *84*, 1-6.

3.17. Schmitt, D. C.; Haldolaarachchige, N.; Xiong, Y. M.; Young, D. P.; Jin, R. Y.; Chan, J. Y., *J. Am. Chem. Soc.* **2012,** *134*, 5965-5973.

3.18. Bodak, O. P.; Gladyshe.Ei, *Sov. Phys. Crystallogr.* **1970,** *14*, 859-861.

3.19. Burla, M. C.; Carrozzini, B.; Cascarano, G. L.; Giacovazzo, C.; Polidori, G., *Z. Kristallogr.* **2002,** *217*, 629-635.

3.20. Sheldrick, G. M., *Acta Crystallogr.* **2008,** *64*, 112-122.

3.21. Spek, A. L., *Acta Cryst.* **2009,** *D65*, 148-155.

3.22. Palenzona, A.; Manfrinetti, P.; Fornasini, M. L., *J. Alloys Comp.* **2000,** *312*, 165-171.

3.23. Leon-Escamilla, E. A.; Corbett, J. D., *Inorg. Chem.* **1999,** *38*, 738-743.

3.24. Ganguli, A. K.; Guloy, A. M.; Leonescamilla, E. A.; Corbett, J. D., *Inorg. Chem.* **1993,** *32*, 4349-4353.

3.25. Fornasini, M. L.; Franceschi, E., *Acta Cryst.* **1977,** *33*, 3476-3479.

3.26. Pöttgen, R.; Hoffmann, R. D.; Sampathkumaran, E. V.; Das, I.; Mosel, B. D.; Müllmann, R., *J. Solid State Chem.* **1997,** *134*, 326-331.

3.27. Wu, Z. Y.; Hoffmann, R. D.; Pottgen, R., *Z. Anorg. Allg. Chem.* **2002,** *628*, 1484-1488.

3.28. Riecken, J. F.; Al Alam, A. F.; Chevalier, B.; Matar, S. F.; Pottgen, R., *Z. Naturforsch Pt. B* **2008,** *63*, 1062-1068.

3.29. Cordero, B.; Gomez, V.; Platero-Prats, A. E.; Reves, M.; Echeverria, J.; Cremades, E.; Barragan, F.; Alvarez, S., *Dalton Trans.* **2008**, 2832-2838.

3.30. Emsley, J., *The Elements*. 2 ed.; Oxford University Press: New York, 1991; p 251.

3.31. Lei, X. W.; Zhong, G. H.; Li, M. J.; Mao, J. G., *J. Solid State Chem.* **2008,** *181*, 2448-2455.

3.32. Francois, M.; Venturini, G.; Malaman, B.; Roques, B., *J. Less-Common Met.* **1990,** *160*, 197-213.

3.33. Chakoumakos, B. C.; Mandrus, D., *J. Alloys Comp.* **1998,** *281*, 157-159.

3.34. Frank, U.; Muller, W.; Schafer, H., *Z. Naturforsch Pt. B* **1975,** *B 30*, 6-9.

3.35. Kauzlarich, S. M., *Chemistry, Structure, and Bonding of Zintl Phases and Ions*. 1 ed.; VCH Publishers, Inc.: New York, 1996; p 306.

3.36. Xing, H.; Long, G.; Guo, H. J.; Zou, Y. M.; Feng, C. M.; Cao, G. H.; Zeng, H.; Xu, Z. A., *J. Phys.: Condens. Matter* **2011,** *23*, 1-6.

3.37. Martin, J. J.; Danielson, G. C., *Phys. Rev.* **1968,** *166*, 879-882.

3.38. Schwall, M.; Schoop, L. M.; Ouardi, S.; Balke, B.; Felser, C.; Klaer, P.; Elmers, H. J., *Adv. Funct. Mater.* **2012,** *22*, 1822-1826.

3.39. Köhler, U. Thermoelectric transport in rare-earth compounds. University of Dresden, Dresden, 2007.

3.40. Ong, K. P.; Singh, D. J.; Wu, P., *Phys. Rev. Lett.* **2010,** *104*, 1-4.

3.41. Tritt, T. M., *Thermal Conductivity Theory, Properties and Applications*. Kluwer Academic: New York, 2004; p 290.

3.42. Toberer, E. S.; May, A. F.; Snyder, G. J., *Chem. Mater.* **2010,** *22*, 624-634.

Chapter 4. Field-Pulse Thermal Memory Storage in the Giant Spin-Glass $Tb_{30}Ru_4Sn_{31}$

4.1 Introduction

Spin-glass materials have been a field of intense research over the past several decades.[4.1-4] They behave as non-equilibrium systems below the glassy transition temperature, leading to a multitude of exotic properties including isothermal time-dependent relaxation[4.5] and frequency-dependent spin dynamics.[4.6] The slow dynamics of spin-glass systems have precluded them from being used as functional materials, as spin-glass memory effects typically require hours of waiting time to achieve a partial equilibrium state.[4.7-9] Here, we find that temperature-specific memory effects of $Tb_{30}Ru_4Sn_{31}$, a material with a large glassy component,[4.10] can be quickly imprinted through magnetic field pulses while cooling the sample. The imprinted memory is then recoverable upon warming through examination of the temperature-dependent magnetization and exhibits very low imprinted memory degradation over time. We also find a field-dependence in the initial magnitude of the imprinted glass component, which can be exploited as an analogue-bit in addition to 8 fully recoverable imprinted bits of information per single crystal, creating a potential new application for spin-glasses as functional materials.

4.1.1 Memory Pulse Experiment

In a canonical spin-glass, a memory effect can be observed by taking advantage of non-equilibrium time-dependent glassy spin dynamics.[4.11] Figure 4.1a shows a typical spin glass memory dip experiment. To obtain a reference, the sample is zero-field cooled to the desired temperature below the glass transition temperature (T_g). The sample is then warmed in a small applied field, and the temperature-dependent magnetization is measured. The procedure is repeated, except that upon cooling, the sample is held at a waiting temperature (T_w) below T_g for a specified period of time before the remaining sequence is completed. As shown in Figure 4.1a, a memory dip forms at T_w, relative to the reference, in the temperature-dependent magnetization.

The memory dip at T_w occurs due to the formation of local ordering with energy-specific correlation lengths.[4.2, 8] It is possible to store and read several memory dips by exploiting this phenomenon.[4.7] In fact, a thermal memory cell was designed which is capable of imprinting and recovering 8-bits of data;[4.9] however, the necessary long wait times prohibit the use of this effect as a viable memory storage technology.

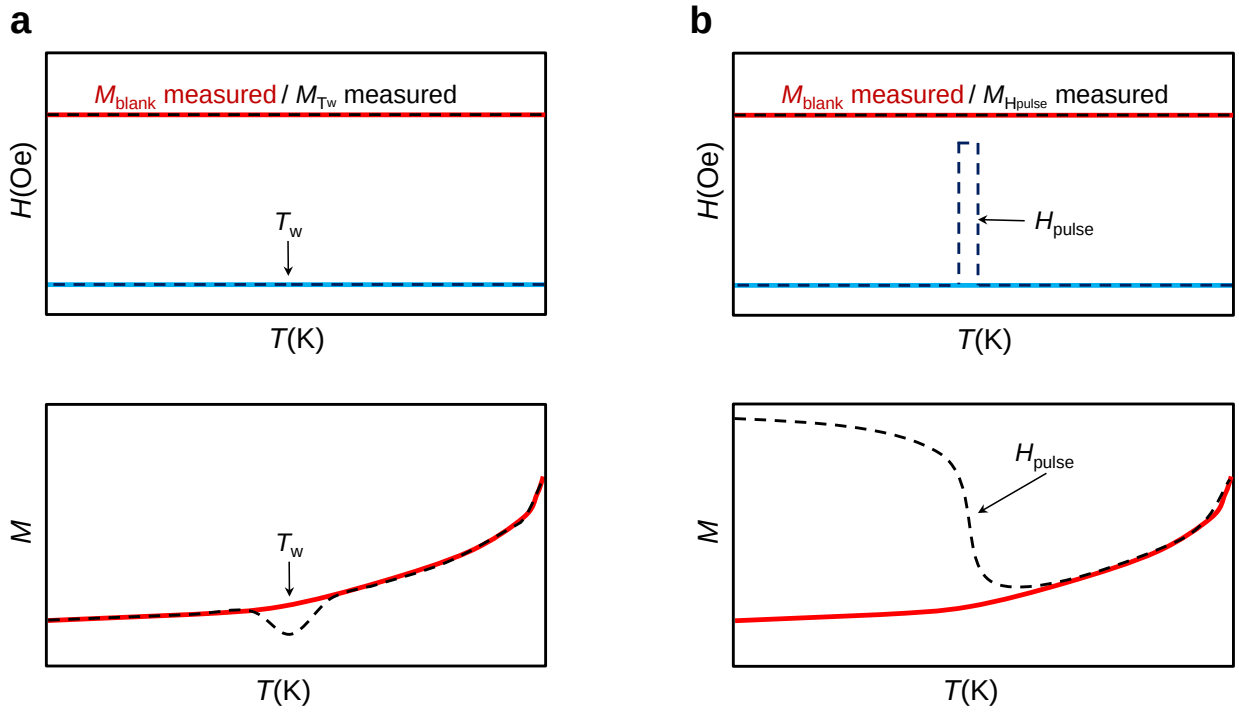

Figure 4.1. Temperature-dependent field (top) and magnetization (bottom) profiles of a typical memory-dip experiment **(a)** and the proposed field-pulse experiment **(b)**. The blue and red lines represent the cooling and warming profiles, respectively, of the blank run, while the dashed lines represent the cooling and warming profiles of a run with a temperature-specific wait (T_w) or a temperature-specific field-pulse (H_{pulse}).

Miyashita and Vincent describe the memory phenomena from previous (higher temperature) length correlations as "frozen impurities," which are capable of melting above the temperatures corresponding to the specific local correlation lengths.[4.8] Mathieu et al. found that the memory from a magnetic field applied at a single elongated wait temperature (T_w = 3000s, H = 0.5 Oe) can be stored by cooling below T_w and recovered by examining the reduction of the magnetization at T_w through the measurement of direct current (DC) magnetization during the

warming process.[4.12] Combining these findings, we surmise that temperature-specific local correlations can be rapidly frozen through a field pulse during the initial cooling cycle, shown in Figure 4.1b. Upon warming, the magnetization should begin (at low *T*) at a maximized value and, as the frozen components approach the temperatures of the corresponding correlation length, a melting should occur, causing an effective magnetization avalanche. Additionally, if the material exhibits a high magnitude of the glassy component, multiple temperature-specific memory avalanches can be stored. Here, the imprinting/recovery rate is limited by the cooling/warming rates and the limitations of the magnetic detector.

4.2 Experimental

Magnetic properties were performed on a single crystal of $Tb_{30}Ru_4Sn_{31}$ oriented in the crystallographic *a*-direction. Crystal growth and structural details can be found in Reference 4.13. Temperature- and field-dependent direct current (DC) magnetization data were collected using a Quantum Design Magnetic Property Measurement System (MPMS) in fields up to 500 Oe. Temperature-dependent alternating current (AC) magnetization data were collected using a Quantum Design Physical Property Measurement System (PPMS) with an AC field of 10 Oe.

4.3 Results and Discussion

4.3.1 Qualitative Spin-Glass Proof

We have grown high quality single crystals of $Tb_{30}Ru_4Sn_{31}$ adopting the $Gd_{30}Ru_4Sn_{31}$ structure-type,[4.13] which exhibit a giant spin-glass effect.[4.10] Figure 4.2a shows a typical thermoremanent magnetization (TRM) measurement conducted on $Tb_{30}Ru_4Sn_{31}$. The maximum glass component of the magnetization of $Tb_{30}Ru_4Sn_{31}$ is estimated to be ~2500 emu/mol-Tb.[4.10] Figure 4.2b shows AC susceptibility measurements of $Tb_{30}Ru_4Sn_{31}$, which show a definitive frequency dependence of the spin dynamics of $Tb_{30}Ru_4Sn_{31}$. The data in Figure 4.2, showing a definitive time-dependence of the DC magnetization (Figure 4.2a) and a shift in the cusp of the

AC susceptibility to higher temperatures as a function of frequency (Figure 4.2b), is presented as qualitative proof that $Tb_{30}Ru_4Sn_{31}$ is a spin-glass system with a large glassy component. Quantitative analysis is beyond the scope of the current report. Nevertheless, the large glassy magnetization component present makes $Tb_{30}Ru_4Sn_{31}$ an ideal candidate to test the field pulse experiment graphically described in Figure 4.1b.

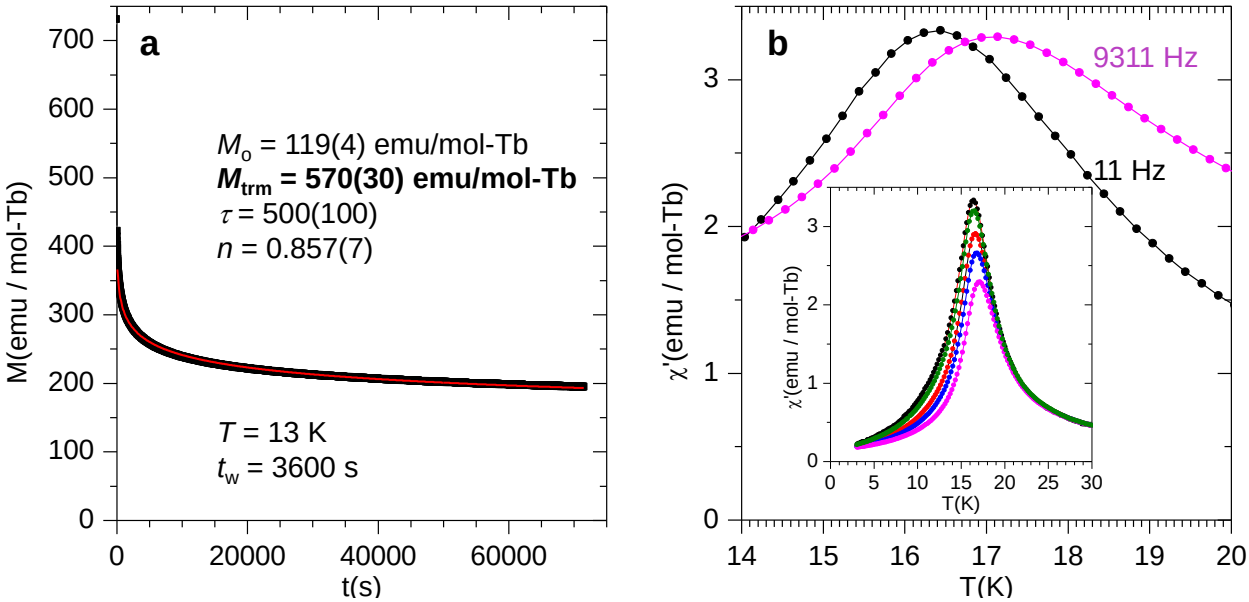

Figure 4.2. (a) Thermoremanent magnetization (time-dependent magnetization) of $Tb_{30}Ru_4Sn_{31}$ collected at T = 13 K with T_w = 3600 s under field cooled conditions of H_i = 100 Oe. Data are fit to the equation $M(t) = M_0 + M_{trm}*e\text{^}[-(t/\tau)\text{^}(1-n)]$, where M_0 is the non-time-dependent remanent magnetic contribution, M_{trm} is the glassy component of the magnetization, t is time, τ is the characteristic time constant, and n is the characteristic stretched exponential exponent. **(b)** Temperature-dependent AC susceptibility of $Tb_{30}Ru_4Sn_{31}$ at 11 Hz (black) and 9311 Hz (purple) normalized to 11 Hz. The inset shows temperature-dependent AC susceptibility collected at frequencies, from left to right, of 11, 57, 579, 2311, and 9311 Hz.

4.3.2 Field-Pulse Experimental Data

Figure 4.3 shows the results of the field pulse experiment with magnetic field pulses applied at 11, 9, 7, 5, and 3 K and field pulse magnitudes of 50, 100, 150, 250, and 400 Oe, respectively. All data are collected using a base field (H_i), during both warming and cooling, of 10 Oe to ensure a positive field bias. Figure 4.3a shows the blank data set (M_b), measured without field pulses, the field pulse data set (M_p), and M_p-M_b, used to subtract the magnetization

induced by the 10 Oe positive field bias. Here, it should be noted that M_b is subtracted in all data for field pulse experiments, unless explicitly noted. A pronounced reduction of the magnetization is observed at temperatures corresponding to each field pulse, shown in Figure 4.3b as $d(M_p\text{-}M_b)/dT$ as a function of temperature. Remarkably, the temperature-dependent correlation lengths at 11, 9, 7, 5 and 3 K are preserved for all field pulses.

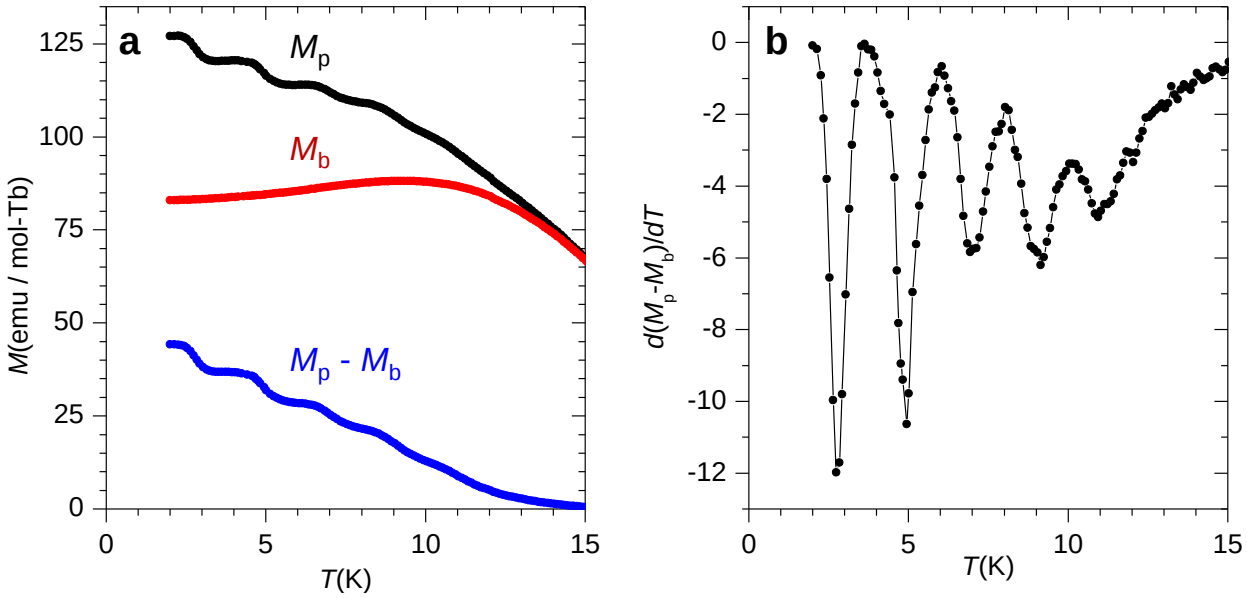

Figure 4.3. **(a)** Temperature-dependent magnetization of $Tb_{30}Ru_4Sn_{31}$ collected upon warming with temperature-specific field-pulses (M_p) at 3, 5, 7, 9, and 11 K (black), the blank run (M_b) without initial field-pulses (red), and $M_p - M_b$ (blue). **(b)** The derivative of $M_p - M_b$ as a function of temperature showing slope minima at temperatures corresponding to the initial field-pulses. The warming and cooling ramp rates were fixed at 0.3 K/min.

4.3.3 Data Density per Single Crystal

The width of the peaks of $d(M_p\text{-}M_b)/dT$ in Figure 4.3b appears to be related to both the pulse duration and the temperature of the pulse, and lower temperatures require higher pulse magnitudes to achieve comparable ΔM values. We have optimized the pulse temperatures and pulse magnitudes, considering the limitations of our instruments, to achieve a magnetically pulsed spin memory density of 8 memory imprints over our measurable temperature and field range with field pulse temperatures of 11, 9.3, 8, 7, 6, 5, 4, and 3 K and field pulse magnitudes of 75, 125, 175, 225, 275, 325, 375, and 425 Oe (50 Oe increases between pulses), respectively.

Additionally, it is apparent in Figure 4.4a (closed circles) that the magnitude of the glass component of the magnetic blank (M_b) scales linearly with initial applied field (H_i) of 2, 4, 6, and 8 Oe. It follows that a threshold bit can be set by exploiting the linear increase in the glass component with H_i to augment the field-imprinted storage capacity of the system. In order to establish an upper limit to the threshold bit, we utilized the aforementioned pulse profile for each H_i and measured the resulting temperature-dependent magnetization curve shown in Figure 4.4a (open circles). The inset of Figure 4.4 shows that the glass magnitudes of each H_i are easily separated at approximately 16 K, allowing for a threshold bit which can linearly augment imprinted memory storage.

Figure 4.4b shows the temperature dependent M_p with field pulses at 9.3, 8, 6, 4, and 3 K collected with H_i = 4 Oe. The inset of Figure 4.4b displays the magnetization ~16 K. The magnetization value at 16 K clearly falls within the H_i = 4 Oe threshold set in Figure 4.4a, inset. Figure 4.4c (red) shows the square of the $d(M_p\text{-}M_b)/dT$ from Figure 4.4b compared to $(d(M_p\text{-}M_b)/dT)^2$ with all field pulses included (offset in black). The locations of the omitted pulses (11.2, 7, and 5 K) in Figure 4.4c are clearly visible with respect to the fully pulsed data. The 8-bits of information generated from the magnetic field-puses, augmented by the 4-fold threshold bit, yields a total memory capacity of 1024 characters (10-bit equivalent) per single crystal given the limitations of our measurement techniques.

4.3.4 Imprinted Memory Volatility

Figure 4.5 highlights the low volatility of imprinted memory when stored at temperatures below the field-pulse temperatures. Spin memory was imprinted in all data sets with field pulses applied at 9 and 5 K, then cooled to 1.8 K, where the sample was held for 120 s (red), 28800 s (black), and 86400 s (blue). The functional forms of the temperature-dependent M_p - M_b curves are nearly identical. Here, it should be noted that the magnitude shifts of the data are the result

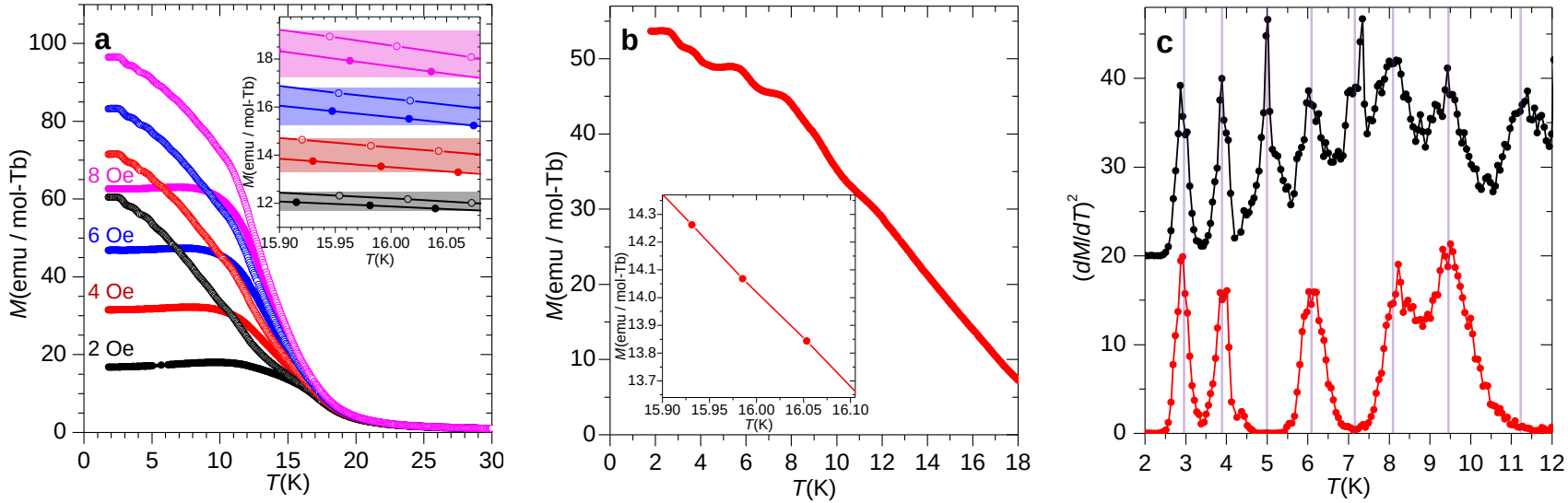

Figure 4.4. **(a)** Temperature-dependent magnetization of $Tb_{30}Ru_4Sn_{31}$ collected upon warming with initial fields (H_i) of 2 (black), 4 (red), 6 (blue), and 8 (purple) Oe with M_p = 3, 4, 5, 6, 7, 8, 9.3, and 11.2 K (open circles) and M_b without initial field-pulses (closed circles). Inset shows the temperature-dependent magnetization between 15.9 and 16.08 K with magnetization threshold values highlighted for clarity. **(b**) Temperature-dependent magnetization collected upon warming with H_i = 4 Oe and M_p = 3, 4, 6, 8, and 9.3 K. Inset shows the temperature-dependent magnetization ~16 K. **(c)** The square of the temperature-dependent derivative of $M_p - M_b$ of data from Figure 4.4b (red) and data from Figure 4.4a (data with all field pulses applied and H_i = 4 Oe) offset by + 20 on the y-axis (black). Vertical lines are added for clarity to highlight the location of the missing field pulse memory at 5, 7, and 11.2 K. The warming and cooling ramp rates were fixed at 0.3 K/min for all collected data.

of a small instrumental variability (+/- 5 Oe) in the magnitude of the field pulses. The decay rate of the higher temperature imprinted spin memory appears sufficiently lowered by cooling through only a few degrees Kelvin, to allow full imprinted memory recovery after being held for an extended time period at lower temperatures.

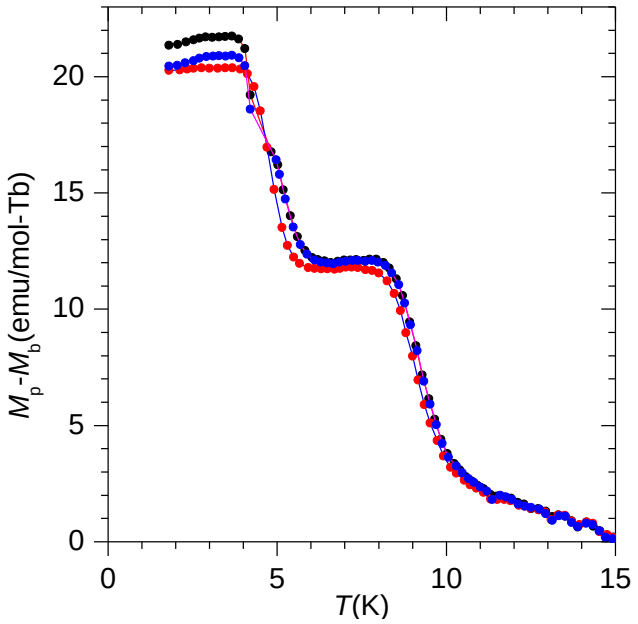

Figure 4.5. Temperature-dependent magnetization (M_p-M_b) of $Tb_{30}Ru_4Sn_{31}$ with H_i = 2 Oe and M_p = 5 and 9 K with the sample held at 1.8 K for 120 s (red), 28,800 s (black), and 86,400 s (blue) prior to data collection upon warming. The warming and cooling ramp rates were fixed at 1 K/min.

4.4 Conclusions

We have successfully created a fast-write thermal memory cell by exploiting the non-equilibrium dynamics in a single crystal of the spin-glass material $Tb_{30}Ru_4Sn_{31}$ to imprint and recover 8-bits of data using magnetic field pulses with a constant temperature ramp rate. One of the main problems with the previous thermal memory cell design was the long time period required to imprint and read data.[4.9] With the spin-glass memory pulse effect, thermal memory read/write rates appear to be limited only by the effective temperature ramp rate limitations of the measurement device. Additionally, we have shown that it is possible to augment the data storage capacity using a four-fold threshold bit by utilizing different initial write fields (H_i). With the 8 written bits and the threshold-bit, a total of 1024 characters per crystal (10-bit word equivalent) can be stored without evidence of memory degradation over a minimum of a 24 hour period. These data were collected within the limitations of our MPMS, which has coarse field control (~0.5 Oe), a limited warming/cooling rate, and the requirement of a relatively long time (several seconds) to change

magnetic fields. To put our instrumental limitations into perspective, we utilized 2 Oe variations for our initial threshold-bit; however, if we utilized an electromagnet with a much finer degree of field control, < 0.5 Oe threshold-bit increments would be feasible, allowing a 16-fold augmentation of storage capacity (with ΔH = 0.5 Oe) using only the threshold-bit and staying within our current H_i = 8 Oe maximum initial field limitation. This alone would yield an effective 12-bit word, and additional parameter tuning would likely increase the storage capacity to 16 bits per crystal or higher. The avalanche nature of the spin-glass memory pulse effect yields another interesting result in that an electric current is not necessary to read imprinted data due to the inductive current generated from the changing magnetic field.

We have shown that spin-glasses, given the correct glass parameter sets, can be useful materials. The two important factors limiting spin-glass functionality in thermal memory storage applications is that the material must exhibit (1) a large glassy magnetization component and (2) a high glass transition temperature. The two aforementioned spin-glass characteristics are not readily obtained using the typical methods for inducing spin-glass behavior, which are the introduction of atomic disorder[4.3] and lattice-induced geometric frustration.[4.4] The ultimate goal, in order to utilize this effect as a viable technology, would be to design a spin-glass material with large glass component and a glass transition temperature > 300 K; however, a material with a glass transition temperature > ~77 K (the boiling point of liquid nitrogen) would enable a device-level application. We believe that a different approach of examining complex materials with competing magnetic interactions, such as our example of $Tb_{30}Ru_4Sn_{31}$[4.13] and the complex intermetallic $Gd_{117}Co_{56}Sn_{112,}$[4.14] which appears to display a significant glassy component as well, may be utilized to discover spin-glasses with large glass components.[4.10] Regardless of the path to achieving the goal, we have shown that the non-equilibrium dynamics of spin-glass systems

are no longer just an interesting academic endeavor; rather, this behavior should be viewed as a parameter to exploit in order to transform spin-glasses into functional materials.

4.5 References

4.1. Fisher, D. S.; Huse, D. A., *Phys. Rev. B* **1988,** *38*, 373-385.

4.2. Fisher, D. S.; Huse, D. A., *Phys. Rev. B* **1988,** *38*, 386-411.

4.3. Ramirez, A. P., *Annu. Rev. Mater. Sci.* **1994,** *24*, 453-480.

4.4. Moessner, R.; Ramirez, A. R., *Physics Today* **2006,** *59*, 24-29.

4.5. Chamberlin, R. V.; Mozurkewich, G.; Orbach, R., *Phys. Rev. Lett.* **1984,** *52*, 867-870.

4.6. Tholence, J. L., *Solid State Commun.* **1980,** *35*, 113-117.

4.7. Bouchaud, J. P.; Dupuis, V.; Hammann, J.; Vincent, E., *Phys. Rev. B* **2002,** *65*, 1-11.

4.8. Miyashita, S.; Vincent, E., *Eur. Phys. J. B* **2001,** *22*, 203-211.

4.9. Dolinsek, J.; Feuerbacher, M.; JagodiC, M.; JagliCic, Z.; Heggen, M.; Urban, K., *J. Appl. Phys.* **2009,** *106*, 043917.

4.10. Prestigiacomo, J.; Schmitt, D. C.; Chan, J. Y.; Young, D. P.; Stadler, S.; Adams, P. W., Observation of a giant spin-glass effect in $Tb_{30}Ru_4Sn_{31}$. Louisiana State University: Baton Rouge, 2013.

4.11. Dupuis, V.; Vincent, E.; Bouchaud, J. P.; Hammann, J.; Ito, A.; Katori, H. A., *Phys. Rev. B* **2001,** *64*, 1-7.

4.12. Mathieu, R.; Hudl, M.; Nordblad, P., *EPL* **2010,** *90*, 1-6.

4.13. Schmitt, D. C.; Haldolaarachchige, N.; Prestigiacomo, J.; Karki, A.; Young, D. P.; Stadler, S.; Jin, R.; Chan, J. Y., *J. Am. Chem. Soc.* **2013,** *135*, 2748-2758.

4.14. Schmitt, D. C.; Haldolaarachchige, N.; Xiong, Y. M.; Young, D. P.; Jin, R. Y.; Chan, J. Y., *J. Am. Chem. Soc.* **2012,** *134*, 5965-5973.

CHAPTER 5. Conclusions and Closing Remarks

5.1 Conclusions

Before drawing four overarching conclusions regarding the work in the previous chapters, I feel that it is necessary to provide a summary of the findings after introducing my dissertation work in Chapter 1. In Chapters 2 and 3, I find that lattice complexity leads to a multitude of interesting physical properties including a large reduction of lattice thermal conductivity, complex magnetic interactions, and exotic behavior in electronic physical properties such as negative temperature coefficient and anisotropic resistivity. I also find that the growth of single crystalline $Ln_{30}Ru_4Sn_{31}$ and $Gd_{117}Co_{56}Sn_{112}$ is possible through the use of a *Ln*–*M* eutectic flux. Additionally, spin-glass behavior is observed in $Ln_{30}Ru_4Sn_{31}$ and is apparent in $Gd_{117}Co_{56}Sn_{112}$ from the bifurcation in temperature-dependent magnetic susceptibility. I find in Chapter 4 that it is possible to exploit the non-equilibrium dynamics present in these spin-glasses for use in functional materials by quickly imprinting memory using magnetic field pulses. The memory can later be recovered with low degradation, and the memory storage capacity per single crystal appears to be very high.

The first conclusion is that examining materials with high structural complexity is a good route to decoupling thermal and electrical properties. Two examples, $Gd_{117}Co_{56}Sn_{112}$ and $Tb_{30}Ru_4Sn_{31}$, are provided to support this argument. It is readily apparent from Figure 5.1, where lattice thermal conductivity of single crystals of these two materials is compared to some of the best known thermoelectric materials, that a complexity-driven reduction of thermal conductivity can provide lower thermal conductivity results than other commonly utilized routes such as nanostructuring and the introduction of atomic disorder. Furthermore, the complexity-driven route should have no effect on carrier mobility. This observation has implications for thermoelectrics, as well as thermal management materials such as thermal barrier coatings.

Additionally, highly anisotropic electrical properties combined with low lattice thermal conductivity may enable the creation of a single crystalline thermal valve, for applications where it may be advantageous to anisotropically direct the flow of thermal energy, while maintaining good electrical contact in all directions.

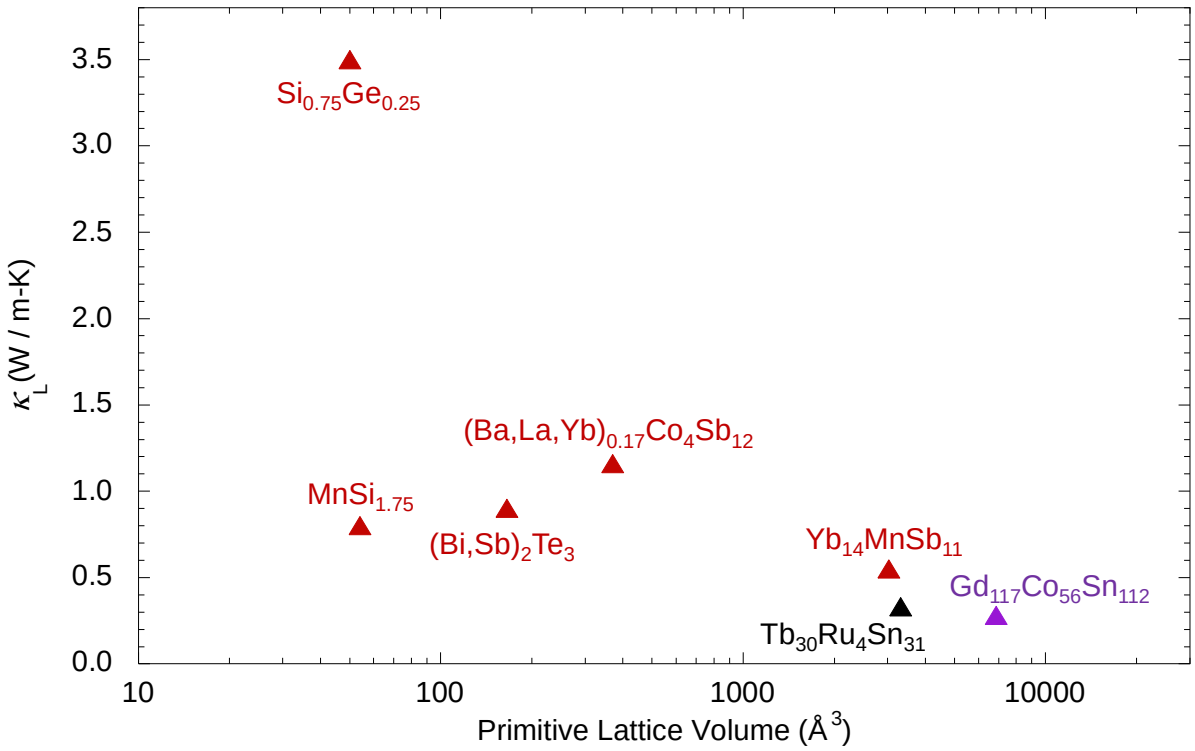

Figure 5.1. Lattice thermal conductivity values as a function of primitive lattice volume for $Gd_{117}Co_{56}Sn_{112}$ (black), $Tb_{30}Ru_4Sn_{31}$ (purple) and some of the best known thermoelectric materials (red). Values obtained from Ref. 5.1.

The second observation, which I concluded by examining the high ratio of *Ln*:*M* and *Ln*:Sn in the studied compounds, is that in order to stabilize these structures over competing Sn-rich phases, a high concentration of *Ln* must be utilized. Single crystals of the compounds $Gd_{117}Co_{56}Sn_{112}$ and $Ln_{30}Ru_4Sn_{31}$ are thought to stabilize from the use of a eutectic *Ln*-*M* flux. It is possible that the technique of using *Ln*-*M* eutectics may stabilize other *Ln*-*M*-*X* compounds, where *X* is a main group element, with high *Ln*:*M* and *Ln*:*X* ratios that were previously unobtainable through conventional flux growth methods.

The third conclusion, which is drawn from Chapter 4, is that spin-glasses can be used as functional materials for thermal memory storage if the material exhibits (1) a large glass component and (2) a high glass transition temperature. The two aforementioned spin-glass characteristics are not readily obtained using the typical methods for inducing spin-glass behavior mentioned previously, which are the introduction of atomic disorder and lattice-induced geometric frustration. However, I believe that a different approach, described below, may be utilized to discover spin-glasses with large glass components.

The fourth, and final, conclusion is that competition between long and short-range magnetic interactions can lead to spin-glass behavior. The conclusion is apparent when examining the possible *Ln–Ln* distances (interactions) that arise from the 8 and 11 different *Ln* sites in $Gd_{117}Co_{56}Sn_{112}$ and $Ln_{30}Ru_4Sn_{31}$ (Appendix Figure A3.4), respectively. Intrinsic spin-glass behavior in complex unit cells is currently being investigated by Prestigiacomo et al.[5.2] This implies that in order to obtain a large glassy component, one should examine materials with a high number of sites which exhibit local magnetic moments, such as rare-earth containing materials. The ultimate goal, in order to utilize this effect as a viable technology, would be to design a spin-glass material with large glass component and a glass transition temperature > 300 K; however, a material with a glass transition temperature > ~77 K (the boiling point of liquid nitrogen) would enable a device-level proof-of-concept. To realize this goal, a combination of short-range-over-long-range-order techniques, such as examining complex materials and introducing atomic disorder, may be needed. An immediately extension of this supposition to produce the desired physical properties is substitution of multiple different *Ln* atoms (i.e. Tb *and* Dy) onto a single atomic position of a complex material. To this effect, I have already identified two potential compounds with the $Dy_{117}Co_{57}Sn_{112}$ structure-type, $Tb_{117}Co_{59}Sn_{111}$ and $Sm_{117}Co_{55.6}Sn_{115}$, which may exhibit large glass components with potential glass transition

temperatures > 40 K and > 80 K, respectively.[5.3] Because of the single read feature, the magnetic pulse memory effect may be advantageous in applications where very high data security is essential, such as corporate or military applications. Regardless of the underlying functional purpose of the materials, it is clear that only with a thorough understanding of the structure-property relationships in complex systems will we be able to tune the properties of these materials in order to exploit them for future applications.

5.2 Closing Remarks

Science in its purest form is about studying the physical laws that govern our universe in an effort to broaden our understanding of these phenomena. Society, however, does not progress through purely academic ventures. Practical knowledge–knowledge that can or will one day be used to further our technological progression and quality of life–is much more valued than knowledge for the sake of itself. Thus, it is important for us, as scientist, to never forget that society is that which enables us the opportunity to study the physical laws of the universe. History shows us that no one really knows what will lead to the next technological revolution, but there it is a certain intuition which allows one to transform a series of seemingly inconsequential and incoherent ideas into applied knowledge. This, I believe, is what it means to be a Doctor of Philosophy, and it is up to each and every one of us to utilize our efforts wisely and for the ultimate benefit of society.

5.3 References

5.1. Schmitt, D. C.; Haldolaarachchige, N.; Xiong, Y. M.; Young, D. P.; Jin, R. Y.; Chan, J. Y., *J. Am. Chem. Soc.* **2012,** *134,* 5965-5973.

5.2. Prestigiacomo, J.; Schmitt, D. C.; Chan, J. Y.; Young, D. P.; Stadler, S.; Adams, P. W., Observation of a giant spin-glass effect in $Tb_{30}Ru_4Sn_{31}$. Louisiana State University: Baton Rouge, 2013.

5.3. Kovnir, K.; Shatruk, M., *Eur. J. Inorg. Chem.* **2011**.

Appendix A1.[†] Crystal Structure and Physical Properties of $Yb_3Co_{4-x}Ru_xSn_{13}$ (x = 0, 0.38)

A1.1 Introduction

The system $Ln_3Rh_4Sn_{13}$ (Ln = Tm – Lu)[A1.1] has generated much interest due to their physical properties, such as the co-existence of magnetism and superconductivity.[A1.2-6] Specifically, $Er_3Rh_4Sn_{13}$ displays re-entrant superconductivity with T_c = 1.2 K followed by a ferromagnetic transition of T_m = 0.34 K.[A1.2] $Ce_3Ir_4Sn_{13}$ was found to exhibit two phase transitions at low temperature: a Fermi surface reconstruction at 2.1 K and an antiferromagnetic (AFM) ordering at 0.6 K.[A1.3, 5] Heavy fermion behavior, an enhancement of the low temperature effective mass of the electrons, was also found in $Ce_3Pt_4In_{13}$[A1.4] and $Ce_3Co_4Sn_{13}$.[A1.6] A review of correlated electron systems, including $Ln_3Co_4Sn_{13}$ (Ln = Pr, Nd, Sm, Gd, Tb), can be found by Thomas *et al.* in Ref [A1.7]. The $Ln_3Rh_4Sn_{13}$ structure-type phases display polar intermetallic behavior,[A1.8] resulting in interesting bonding interactions. It is of interest to determine intrinsic properties via high quality single crystals and to study the effects of doping on the structure and physical properties of these materials.

Yb in polycrystalline $Yb_3Co_4Sn_{13}$ has been previously reported to be intermediate valent,[A1.9] with a valency close to 2 and a small effective momentof 1.1 μ_B/Yb; therefore, doping could be a means to tune the valence of Yb. Additionally, the undoped $Yb_3Co_4Sn_{13}$ showed a superconducting transition with T_c = 3.4 K and a nominal ~ 18 μV/K Seebeck coefficient,[A1.9] which is about an order of magnitude larger than most metals. We were interested in the effect of Ru substitution on the thermopower of $Yb_3Co_4Sn_{13}$ considering that systems with valence instabilities, such as $YbAl_3$[A1.10] and $CePd_3$,[A1.11] show enhancements in their Seebeck coefficients

[†]Schmitt, D. C.; Haldolaarachchige, N.; Young, D. P.; Jin, R. Y.; Chan, J. Y., *Z. Anorg. Allg. Chem.* **2011,** *637,* 2046-2051. DOI: 10.1002/zaac.201100296

and large thermoelectric power factors as a result of valence instability concomitant with metallic conductivity. Though polycrystalline $Yb_3Co_4Sn_{13}$ has been previously characterized, we have synthesized and measured single crystals of undoped $Yb_3Co_4Sn_{13}$ to directly compare the intrinsic properties of Ru doped $Yb_3(Co,Ru)_4Sn_{13}$ single crystals. We also performed temperature dependent single crystal X-ray data collections and refinements at 100 K, 298 K, and 375 K in order to determine the temperature dependence of the crystal structure, and magnetic and transport properties were measured as a function of temperature and magnetic field. The results are then compared with a previously published theoretical model of $Ln_3Co_4Sn_{13}$.[A1.12]

A1.2 Experimental

A1.2.1 Synthesis

Ingots of Yb, Co powder, Ru powder, and Sn shot (all > 99.9 weight % purity, metal basis) were used as received. Single crystals were obtained by the self-flux method.[A1.13] Yb, Co powder, Ru powder, and Sn shot were loaded in a 5:5:1:100 molar ratio (2:1:10 molar ratio of Yb:Co:Sn for $Yb_3Co_4Sn_{13}$) into an alumina crucible, loaded into a fused silica tube, and capped with silica wool. The fused silica tubes were evacuated, filled with ~0.5 atm of ultra high-purity Ar gas (to reduce the effect of high Yb vapor pressure), then sealed. The reactions were heated in a furnace at 75 °C/hr to 1000 °C, at 20 °C/hr to 1125 °C, dwelled for 8 hr, then cooled to 500 °C at 5 °C/hr where the samples were inverted and spun in a centrifuge to decant the excess flux. Silver colored polyhedral shaped single crystals of $Yb_3Co_4Sn_{12.80(1)}$ and $Yb_3Co_{3.62(6)}Ru_{0.38(6)}Sn_{12.84(1)}$ approximately 1 mm in length were extracted. A small amount of residual Sn flux remaining on the crystal surfaces was removed by etching in 2M HCl for several hours.

A1.2.2 X-ray Diffraction

Single crystals of $Yb_3Co_4Sn_{12.80(1)}$ and $Yb_3Co_{3.62(6)}Ru_{0.38(6)}Sn_{12.84(1)}$ were cleaved to appropriate dimensions (Table A1.1) and mounted to a glass fiber. Single crystal X-ray diffraction was performed using a Nonius Kappa CCD X-ray diffractometer equipped with a graphite monochromator and Mo K_α radiation (λ = 0.71073 Å). Diffraction data were collected at 100 K, 298 K, and 375 K up to θ = 31.0 °. Direct methods were used to solve the crystal structure using SIR2002[A1.14] and refinement was conducted in SHELXL97.[A1.15] Statistics suggested that the space group was centrosymmetric. The observed systematic absences for all analogues and temperatures reported ($h00$: $h = 2n$, $0k0$: $k = 2n$, $00l$: $l = 2n$, hhl: $l = 2n$, and $h\bar{h}l$: $l = 2n$) matched the centrosymmetric space groups $Pm\bar{3}n$ and $P4\bar{3}n$, of which only $Pm\bar{3}n$ (SG# 223) resulted in valid solutions using direct methods. Additional crystallographic parameters are shown in Table A1.1. The refined stoichiometry $Yb_3Co_{3.62(6)}Ru_{0.38(6)}Sn_{12.84(1)}$ was obtained by averaging the modeled occupancies for the 100 K and 298 K temperature collections and is consistent with the stoichiometry determined by energy dispersive spectroscopy (EDS). $Yb_3Co_4Sn_{12.80(1)}$ and $Yb_3Co_{3.62(6)}Ru_{0.38(6)}Sn_{12.84(1)}$ will herein be referred to as $Yb_3Co_4Sn_{13}$ and $Yb_3(Co,Ru)_4Sn_{13}$, respectively. Atomic parameters are given in Table A1.2.

Powder X-ray diffraction data were collected using a Bruker D8 Advance Powder X-ray diffractometer with monochromatic Cu $K_{\alpha 1}$ radiation with λ = 1.540562 Å. Powder diffraction data are in good agreement with calculated powder patterns using the single crystal refinement models, indicating high purity.

A1.2.3 EDS Analysis

Elemental analysis was performed using the EDS technique with a JEOL JSM-5060 scanning electron microscope (SEM) with an accelerating voltage of 15 keV and a crystal to detector distance of 20 mm. The EDS determined stoichiometries of the undoped and Ru doped

Table A1.1. Crystallographic parameters for $Yb_3Co_4Sn_{13}$ and $Yb_3(Co,Ru)_4Sn_{13}$

Formula	$Yb_3Co_4Sn_{12.80}$	$Yb_3Co_{3.62}Ru_{0.38}Sn_{12.84}$	$Yb_3Co_{3.62}Ru_{0.38}Sn_{12.84}$	$Yb_3Co_{3.62}Ru_{0.38}Sn_{12.84}$
Crystal System	Cubic	Cubic	Cubic	Cubic
Space Group	$Pm\bar{3}n$	$Pm\bar{3}n$	$Pm\bar{3}n$	$Pm\bar{3}n$
a (Å)	9.535(2)	9.516(2)	9.548(4)	9.558(2)
V (Å)^3	866.9(3)	861.7(3)	870.4(6)	873.2(3)
Z	2	2	2	2
Crystal dimensions (mm^3)	0.05 x 0.05 x 0.05	0.03 x 0.05 x 0.05	0.03 x 0.05 x 0.05	0.03 x 0.05 x 0.05
Temperature (K)	298(2)	100(2)	298(2)	375(2)
θ range (º)	3.02 - 30.91	4.28 - 30.89	3.02 - 30.87	4.26 - 30.83
μ (mm^{-1})	37.732	37.977	37.608	37.48
Data Collection				
Measured Reflections	572	479	485	485
Unique Reflections	272	270	272	271
Reflections with I>2σ(I)	245	246	249	239
R_{int}	0.017	0.0227	0.0148	0.0189
h	1 to 13	2 to 13	1 to 13	2 to 13
k	0 to 9	0 to 9	0 to 9	0 to 9
l	0 to 9	0 to 9	0 to 9	0 to 9
Refinement				
$\Delta\rho_{max}$ (eÅ^{-3})/$\Delta\rho_{min}$ (eÅ^{-3})	1.075 / -1.041	1.362 / -1.19	1.26 / -1.068	1.261 / -0.916
GoF	1.211	1.281	1.157	1.206
Extinction coefficient	0.00320(13)	0.00135(11)	0.00341(17)	0.0042(2)
Reflections/Parameters	272 / 14	270 / 15	272 / 15	271 / 15
R_1 ($F^2 > 2\sigma F^2$) [a]	0.0194	0.023	0.0205	0.0221
wR_2 (F^2) [b]	0.0356	0.0416	0.0437	0.0442

[a] $R1 = \sum|Fo| - |Fc|/\sum|Fo|$.

[b] $wR2 = [\sum[w(F_o^2 - F_c^2)]/\sum[w(F_o^2)^2]]^{1/2}$.

samples using an average of at least 6 scans at different points on the crystal were $Yb_{3.0(1)}Co_{3.7(1)}Sn_{12.1(2)}$ and $Yb_{3.0(3)}Co_{3.5(1)}Ru_{0.6(2)}Sn_{12.4(3)}$, respectively, consistent with the refined composition as determined by X-ray diffraction.

Table A1.2. $Yb_3Co_4Sn_{13}$ and $Yb_3(Co,Ru)_4Sn_{13}$ crystallographic positions, occupancies, and thermal parameters

Atom	Site	*x*	*y*	*z*	Occ.	U_{eq} (Å^2) [a]
$Yb_3Co_4Sn_{13}$ (298 K)						
Yb1	6*d*	1/4	0	1/2	1	0.00946(17)
Co1	8*e*	1/4	1/4	3/4	1	0.0064(3)
Sn1	2*a*	0	0	0	0.800(8)	0.0161(7)
Sn2	24*k*	0	0.15724(5)	0.69671(5)	1	0.01021(16)
$Yb_3(Co,Ru)_4Sn_{13}$ (100 K)						
Yb1	6*d*	1/4	0	1/2	1	0.00316(19)
Co1	8*e*	1/4	1/4	3/4	0.909(14)	0.0039(6)
Ru1	8*e*	1/4	1/4	3/4	0.091(14)	0.0039(6)
Sn1	2*a*	0	0	0	0.833(10)	0.0064(8)
Sn2	24*k*	0	0.15687(5)	0.69681(6)	1	0.00371(18)
$Yb_3(Co,Ru)_4Sn_{13}$ (298 K)						
Yb1	6*d*	1/4	0	1/2	1	0.00713(19)
Co1	8*e*	1/4	1/4	3/4	0.902(13)	0.0050(5)
Ru1	8*e*	1/4	1/4	3/4	0.098(13)	0.0050(5)
Sn1	2*a*	0	0	0	0.844(9)	0.0137(7)
Sn2	24*k*	0	0.15704(5)	0.69688(5)	1	0.00758(18)
$Yb_3(Co,Ru)_4Sn_{13}$ (375 K)						
Yb1	6*d*	1/4	0	1/2	1	0.0127(2)
Co1	8*e*	1/4	1/4	3/4	0.936(14)	0.0086(6)
Ru1	8*e*	1/4	1/4	3/4	0.065(14)	0.0086(6)
Sn1	2*a*	0	0	0	0.827(10)	0.0197(8)
Sn2	24*k*	0	0.15710(6)	0.69691(6)	1	0.0133(2)

[a] U_{eq} is defined as 1/3 of the trace of the orthogonalized U_{ij} tensor.

A1.2.4 Physical Properties

Physical properties measurements of $Yb_3Co_4Sn_{13}$ and $Yb_3(Co,Ru)_4Sn_{13}$ were performed on single crystals. The crystals were not oriented prior to measurement. Magnetic measurements were conducted using a Quantum Design Magnetic Property Measurement System (MPMS). Temperature-dependent magnetization was measured under zero-field cooled

and field-cooled conditions with an applied field of 0.1 T from 2 to 298 K. Temperature-dependent electrical resistivity data were collected using the PPMS with a standard 4-probe dc technique from 1.9 to 350 K for $Yb_3Co_4Sn_{13}$ and a standard 4-probe ac technique with an excitation current of 5.13 mA and a frequency of 27 Hz from 1.9 to 350 K for $Yb_3(Co,Ru)_4Sn_{13}$. The temperature-dependence of the Seebeck coefficient from 40 to 350 K was measured in the PPMS using a comparative technique with a constantan standard.

A1.3 Results and Discussion

A1.3.1 Structure

$Yb_3(Co,Ru)_4Sn_{13}$ crystallizes in the $Yb_3Rh_4Sn_{13}$ structure type,[A1.1] which resembles the perovskite structure $AA'_3B_4O_{12}$. Sn(1) occupies A, Yb occupies a transformed A', M occupies B (M = Co, Ru), and Sn(2) occupies the O site in $Yb_3Co_4Sn_{13}$ and $Yb_3(Co,Ru)_4Sn_{13}$, similar to previously reported $Yb_3Rh_4Sn_{13}$ analogues.[A1.1, 6] The room temperature model of $Yb_3(Co,Ru)_4Sn_{13}$ was used for structural descriptions unless otherwise noted.

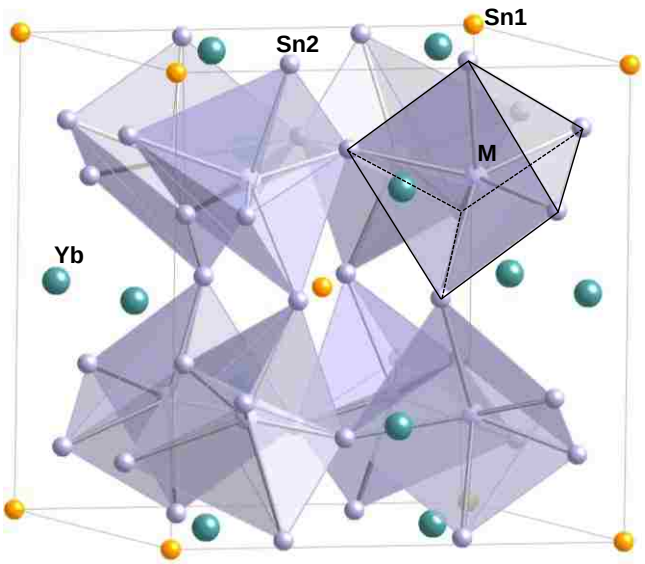

Figure A1.1. Framework of $M@Sn(2)_6$ trigonal prisms (purple), where M = Co,Ru. Yb (green) occupies the interstitial sites at the center and corners of the cell. The $M@Sn(2)_6$ trigonal prism is highlighted for clarity.

The crystal structure of $Yb_3(Co,Ru)_4Sn_{13}$ is shown in Figure A1.1. It is built of an M—Sn framework (M = Co, Ru) with a corner sharing network of slightly distorted $M@Sn(2)_6$ trigonal prisms. The M—Sn(2) bond distance (2.5966(10) Å) is similar to Co—Sn distances of 2.50 – 2.61 Å in the ternary intermetallic compounds $Ln_3Co_4Sn_{13}$ (Ln = Pr, Nd, Sm, Gd, Tb),[A1.7] $Ln_4Co_2Sn_5$,[A1.16] and Yb_3CoSn_6[A1.17]. A strong Sn(2)—Sn(2) bond of 2.9992(14) Å, similar to the

Sn(2)—Sn(2) bond length of $Yb_3Rh_4Sn_{13}$ of 2.9672(7) Å,[A1.1] links corners of the Co-centered trigonal prism. The aforementioned distortion of the M trigonal prisms arises from a slight twisting of the two triangular faces in opposing directions (the D_{3h} *M* symmetry moves toward D_{3d}) and increases as a function of temperature. Table A1.3 shows interatomic distances of $Yb_3(Co,Ru)_4Sn_{13}$ at temperatures of 100 K, 298 K, and 375 K. In the Ru-substituted phase, Ru atoms partially occupy the Co 8*e* site and is consistent with Ru—Sn contacts (2.57 – 2.70 Å) found in the intermetallic compounds Ru_2Sn_3[A1.18] and $CeRu_4Sn_6$.[A1.19]

Table A1.3. Select interatomic distances of $Yb_3Co_4Sn_{13}$ (left) and $Yb_3(Co,Ru)_4Sn_{13}$ (right) and % change in $Yb_3(Co,Ru)_4Sn_{13}$ interatomic distances of from 100—298 K and 100—375 K

$Yb_3Co_4Sn_{13}$	298 K	100 K	298 K	375 K	$\Delta\%_{100—298K}$	$\Delta\%_{100—375K}$
Sn2—Sn2	2.9986(9)	2.9857(8)	2.9992(10)	3.0033(7)	0.452	0.589
Yb cuboctahedron						
Yb – Sn2 (x 4)	3.3075(8)	3.3041(9)	3.3134(14)	3.3164(6)	0.281	0.372
Yb – Sn2 (x 8)	3.3835(6)	3.3758(6)	3.3883(10)	3.3922(5)	0.370	0.486
M trigonal prism						
M – Sn2 (x 6)	2.5928(7)	2.5886(5)	2.5966(9)	2.5991(3)	0.309	0.406
Sn1 icosahedron						
Sn1 – Sn2 (x 12)	3.2574(7)	3.2484(9)	3.2596(12)	3.2629(7)	0.295	0.446

Sn partially occupies the cationic 2*a* distorted icosahedral site. The equilateral triangle and isosceles triangle faces of the Sn(1) icosahedron are formed by faces and edges of $Co@Sn(2)_6$ trigonal prisms, respectively. The Sn(1)—Sn(2) interatomic distance of 3.2596(12) Å is shorter than the $Sn(1)@Sn(2)_{12}$ bond distance of 3.32 – 3.33 Å reported in $A_3Rh_4Sn_{13}$ analogues (A = Ca, Sr, La—Nd, Sm—Gd, Yb, Th)[A1.8] but similar to the $Yb_3Co_4Sn_{13}$ Sn(1)—Sn(2) distance of 3.2574(7) Å.

The Yb environment consists of a distorted cuboctahedral coordination of Sn(2). The Yb—Sn interatomic distances of the $Yb@Sn(2)_{12}$ cuboctahedron, 3.3134(14) Å (×4) and 3.3883(10) Å (×8), are shorter than the Yb—Sn distances of 3.3903(3) and 3.4212(2) Å for $Yb_3Rh_4Sn_{13}$,[A1.8] but longer than the $Yb_3Co_4Sn_{13}$ distances of 3.3075(8) and 3.3835(6) Å determined in this work.

A1.3.2 Magnetization

Figure A1.2a shows magnetic susceptibility data of single crystal $Yb_3Co_4Sn_{13}$ measured at 0.1 Tesla. Susceptibility data of $Yb_3Co_4Sn_{13}$ are fit using the modified Curie-Weiss law $\chi = \chi_0 + C / (T - \theta_{CW})$ between 50 and 350 K, where χ_0 is the temperature-independent susceptibility, C is the Curie-Weiss constant, and θ_{CW} is the Curie-Weiss temperature. The data are well described

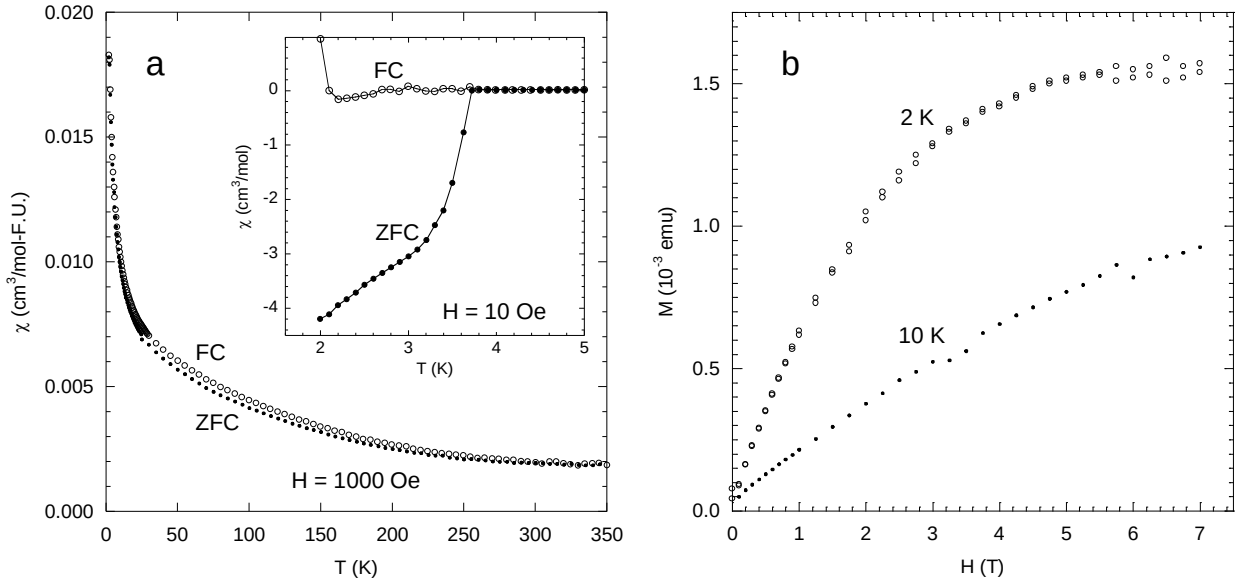

Figure A1.2. **(a)** Field-cooled (FC) and zero-field cooled (ZFC) magnetic susceptibility of $Yb_3Co_4Sn_{13}$ at 1000 Oe. The inset shows FC and ZFC susceptibility data from 2–5 K at 10 Oe. **(b)** Magnetization as a function of field of $Yb_3Co_4Sn_{13}$.

by the Curie-Weiss formula, with $\chi_0 \sim 1.31\times10^{-4}$ cm^3/mol, C = 0.65 K cm^3/mol and $\theta_{CW} \sim -64.2$ K. The constant C gives an effective moment of 2.27μ_B/formula unit or 0.75 μ_B/Yb. The calculated magnetic moment is slightly smaller than that obtained from the polycrystalline sample (1.1 μ_B/Yb),[A1.9] but the absolute magnitude of θ_{CW} for our single crystals is much larger than the value reported for polycrystalline samples (θ_{CW} = −15 K),[A1.9] implying stronger antiferromagnetic (AFM) interactions in $Yb_3Co_4Sn_{13}$ single crystals. Positive magnetoresistance (MR) is expected in AFM systems, as the application of field tends to reduce the AFM interaction, increasing spin scattering. Surprisingly, the temperature dependence of the MR

shown in Figure A1.3a indicates that MR is negative at high temperatures but positive below ~ 80 K. This suggests that the magnetic interactions are more complicated than simple AFM correlation. This is further evident by the low-temperature $M(H)$ of $Yb_3Co_4Sn_{13}$ single crystals shown in Figure A1.2b. The magnetization deviates from linearity, and tends to saturate in high fields with a saturated magnetic moment of 0.019 and 0.011 μ_B/Yb at 2 and 10 K, respectively. This suggests that ferromagnetic (FM) type magnetic interactions are dominant at low temperatures and high fields. The small magnetic moment obtained from Yb, relative to the calculated saturated moment of trivalent Yb of 4.0 μ_B/Yb, may be the result of the itinerancy of the electrons. Magnetic susceptibility data and field dependent magnetization (not shown) of $Yb_3(Co,Ru)_4Sn_{13}$ indicate weak Pauli paramagnetic behavior, contrasting the paramagnetic susceptibility behavior observed in $Yb_3Co_4Sn_{13}$. Doping of Ru onto the Co 8*e* site results in a fully divalent (non-magnetic) Yb oxidation state in $Yb_3(Co,Ru)_4Sn_{13}$.

A1.3.3 Electrical Resistivity

Figure A1.3a shows the temperature dependence of the electrical resistivity of $Yb_3Co_4Sn_{13}$ between 2 and 350 K at both zero field and 8 Tesla. In both cases, the resistivity decreases with decreasing temperature reflecting metallic behavior. At high temperatures, the resistivity varies almost linearly with temperature, while below ~ 150 K, $\rho(T)$ decreases faster than the high-temperature case. While there is small upturn below ~ 10 K at 8 Tesla, a sharp drop occurs in zero-field resistivity at T_c = 3.8 K (see Figure A1.3a, inset). Although the previously reported polycrystalline sample showed similar character in its zero-field resistivity,[A1.9] we note several differences: (1) the residual resistivity ratio $\rho(300K)/\rho(4K)$ ~ 2.78 for our single crystal is considerably larger than that of the polycrystalline sample; (2) there is no sign of saturation of $\rho(T)$ up to 350 K (see Figure A1.3a); (3) the step-like resistivity drop (see Figure A1.3a, inset) suggests filamentary superconductivity, in contrast with the bulk superconductivity observed in

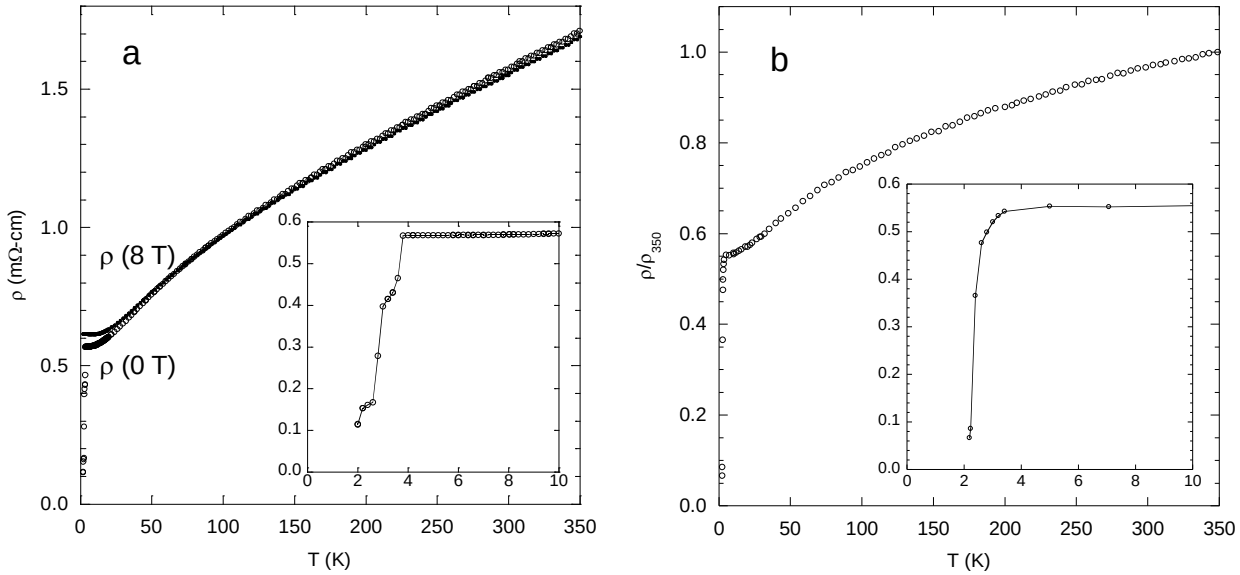

Figure A1.3. (**a)** Resistivity at 0 T and 8 T as a function of temperature of $Yb_3Co_4Sn_{13}$. (**b)** Magnetoresistance (% MR) as a function of temperature of $Yb_3Co_4Sn_{13}$.

the polycrystalline sample.[A1.9] The temperature dependent resistivity of $Yb_3(Co,Ru)_4Sn_{13}$ from 1.9 K to 350 K (Figure A1.3b) varies sublinearly at temperatures above 20 K ($d\rho/dT$ decreases as a function of temperature), in contrast to the almost linear temperature dependence of $Yb_3Co_4Sn_{13}$. The *RRR* ρ(300 K)/ρ(4 K) ~ 1.75 is lower than the *RRR* values of $La_3Co_4Sn_{13}$ (~ 6),[A1.6] $Yb_3Co_{4.3}Sn_{12.7}$ (~ 2.2),[A1.9] and our single crystal $Yb_3Co_4Sn_{13}$ (~ 2.78). In a typical metal, the *RRR* value can be used to determine the purity of the material; thus; the lower *RRR* value relects higher impurity scattering contribution in $Yb_3(Co,Ru)_4Sn_{13}$. The onset of a broad superconducting transition occurs around 3.6 K (Figure A1.3b, inset). Less than 3 % of the sample by volume exhibited a fully diamagnetic Meissner signal (not shown); thus, the superconductivity can be attributed to filamentary Sn inclusions. Similar to undoped $Yb_3Co_4Sn_{13}$, $Yb_3(Co,Ru)_4Sn_{13}$ exhibits a classical positive magnetoresistance at 3 K of ~ 4 % at the highest measured field of 8 Tesla (not shown).

A1.3.4 Thermopower

Figure A1.4 shows thermopower data of $Yb_3Co_4Sn_{13}$ and $Yb_3(Co,Ru)_4Sn_{13}$. The thermopower of $Yb_3Co_4Sn_{13}$ is positive over the entire temperature range measured and increases as a function of temperature until ~ 350 K. A positive sign of the Seebeck coefficient indicates that holes are the dominant charge carrier. The thermopower of $Yb_3(Co,Ru)_4Sn_{13}$ is negative below 150 K and then becomes positive above 250 K. Both thermopower trends are consistent with previously published $Ce_3Rh_4Sn_{13}$[A1.20] but much lower than the 18 μV/K at 250 K reported for $Yb_3Co_{4.3}Sn_{12.7}$[A1.9]. The $Yb_3(Co,Ru)_4Sn_{13}$ thermopower data indicates a shift from predominately electron-type conduction at low temperature to hole-type conduction at high temperature. This agrees well with density functional calculations conducted on $La_3Co_4Sn_{13}$, which show that antibonding bands formed by Co $d_{xz}(d_{yz})$ and Sn(2) 5*p* orbitals are responsible for conduction.[A1.12] A small electron-like Fermi surface at the Fermi level is responsible for low temperature conduction, while a hole-like Fermi surface around the Fermi level leads to hole-type conduction at higher temperatures[A1.12] and, consequently, the positive thermopower observed at room temperature and above.

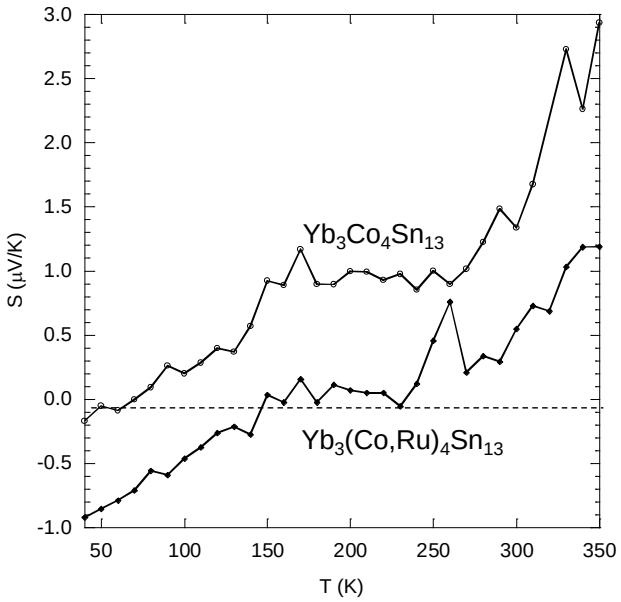

Figure A1.4. Thermopower data as a function of temperature for $Yb_3Co_4Sn_{13}$ and $Yb_3(Co,Ru)_4Sn_{13}$. The dashed line shows the zero-crossing of the thermopower.

Previously reported density functional calculations show that the 24*k* Sn(2) site in $Ln_3Co_4Sn_{13}$ (*Ln* = La, Ce, Sm, Gd, Tb) is not located in the most stable position. In all cases the most stable calculated position allows the Sn(2)—Sn(2) bond to relax to a longer bond length

than the experimental results.[A1.12] This trend can be seen in $Yb_3(Co,Ru)_4Sn_{13}$ with Sn(2)—Sn(2) bond length expansion as a function of temperature at 0.452 % from 100—298 K and 0.589 % from 100—375 K. The Sn(2)—Sn(2) distance expands faster as a function of temperature than any other nearest neighbor atomic distance in the unit cell (Table A1.3), especially considering that the lattice expands by only 0.336 % and 0.441 % for 100—298 K and 10—375 K, respectively .

Maraglia *et al.* conducted a structural analysis of $A_3Rh_4Sn_{13}$ (*A* = Ca, Sr, La – Nd, Sm - Gd, Yb, Th) from a more analytical point of view, indicating that the valences of the cationic Sn (2*a*) and *A* (6*d*) sites are inversely related.[A1.8] They also found, based on bond distance and lattice constant analysis, that Yb in $Yb_3Rh_4Sn_{13}$ should be between a divalent and trivalent state.[A1.8] The longer Yb—Sn(2) distances in $Yb_3(Co,Ru)_4Sn_{13}$ compared to $Yb_3Co_4Sn_{13}$ indicates that Yb has a more divalent character in $Yb_3(Co,Ru)_4Sn_{13}$ relative to $Yb_3Co_4Sn_{13}$. Magnetic susceptibility data shows that Ru substitution on the Co 8*e* site of $Yb_3(Co,Ru)_4Sn_{13}$ results in a fully divalent Yb cation and Pauli paramagnetic behavior, similar to the magnetic behavior observed in $La_3Rh_4Sn_{13}$[A1.21] and $La_3Co_4Sn_{13}$.[A1.6]

A1.4 Conclusions

In summary, we have successfully grown single crystals of $Yb_3Co_{4-x}Ru_xSn_{13}$ with Ru substituted onto the Co 8*e* site and compared physical properties relative to single crystals of the undoped $Yb_3Co_4Sn_{13}$ sample. Ru substitution enhanced the *n*-type conduction of $Yb_3(Co,Ru)_4Sn_{13}$ single crystals and reduced the *RRR* value relative to $Yb_3Co_4Sn_{13}$. A clear zero-crossing in the thermopower was seen in $Yb_3(Co,Ru)_4Sn_{13}$, indicating a change of the dominant charge carriers from electrons to holes, which is explained by previously published density functional calculations.[A1.12] As shown by magnetization data, Ru substitution reduces the localized valent state of Yb in $Yb_3Co_4Sn_{13}$. The negative chemical pressure created by lattice

expansion from the Ru doping may induce the *f*-electron delocalization, leading to the non-magnetic divalent state of Yb in $Yb_3(Co,Ru)_4Sn_{13}$.

A1.5 References

A1.1. Hodeau, J. L.; Chenavas, J.; Marezio, M.; Remeika, J. P., *Solid State Commun.* **1980,** *36*, 839-845.

A1.2. Hodeau, J. L.; Marezio, M.; Remeika, J. P., *Acta Cryst.* **1984,** *40*, 26-38.

A1.3. Sato, H.; Fukuhara, T.; Iwakawa, S.; Aoki, Y.; Sakamoto, I.; Takayanagi, S.; Wada, N., *Physica B* **1993,** *188*, 630-632.

A1.4. Hundley, M. F.; Sarrao, J. L.; Thompson, J. D.; Movshovich, R.; Jaime, M.; Petrovic, C.; Fisk, Z., *Phys. Rev. B* **2002,** *65*.

A1.5. Nagoshi, C.; Sugawara, H.; Aoki, Y.; Sakai, S.; Kohgi, M.; Sato, H.; Onimaru, T.; Sakakibara, T., *Physica B* **2005,** *359*, 248-250.

A1.6. Thomas, E. L.; Lee, H.-O.; Bankston, A. N.; MaQuilon, S.; Klavins, P.; Moldovan, M.; Young, D. P.; Fisk, Z.; Chan, J. Y., *J. Solid State Chem.* **2006,** *179*, 1642-1649.

A1.7. Thomas, E. L.; Millican, J. N.; Okudzeto, E. K.; Chan, J. Y., *Comments Inorg. Chem.* **2006,** *27*, 1-39.

A1.8. Miraglia, S.; Hodeau, J. L.; Marezio, M.; Laviron, C.; Ghedira, M.; Espinosa, G. P., *J. Solid State Chem.* **1986,** *63*, 358-368.

A1.9. Mudryk, Y.; Grytsiv, A.; Rogl, P.; Dusek, C.; Galatanu, A.; Idl, E.; Michor, H.; Bauer, E.; Godart, C.; Kaczorowski, D.; Romaka, L.; Bodak, O., *J. Phys.: Condens. Matter* **2001,** *13*, 7391-7402.

A1.10. Rowe, D. M.; Kuznetsov, V. L.; Kuznetsova, L. A.; Min, G., *J. Phys. D: Appl. Phys.* **2002,** *35*, 2183-2186.

A1.11. Mahan, G. D., *Good Thermoelectrics*. Academic Press Inc: San Diego, 1998; Vol. 51, p 81-157.

A1.12. Zhong, G. H.; Lei, X. W.; Mao, J. G., *Phys. Rev. B* **2009,** *79*, 1-13.

A1.13. Canfield, P. C.; Fisk, Z., *Philos. Mag. B* **1992,** *65*, 1117-1123.

A1.14. Burla, M. C.; Carrozzini, B.; Cascarano, G. L.; Giacovazzo, C.; Polidori, G., *Z. Kristallogr.* **2002,** *217*, 629-635.

A1.15. Sheldrick, G. M., *Acta Crystallogr.* **2008,** *64*, 112-122.

A1.16. Pani, M.; Manfrinetti, P.; Palenzona, A.; Dhar, S. K.; Singh, S., *J. Alloys Comp.* **2000,** *299*, 39-44.

A1.17. Lei, X. W.; Zhong, G. H.; Li, M. J.; Mao, J. G., *J. Solid State Chem.* **2008,** *181*, 2448-2455.

A1.18. Schwomma, O.; Nowotny, H.; Wittmann, A., *Monatsh. Chem. Verw. TL* **1964,** *95*, 1538-1541.

A1.19. Pöttgen, R.; Hoffmann, R. D.; Sampathkumaran, E. V.; Das, I.; Mosel, B. D.; Müllmann, R., *J. Solid State Chem.* **1997,** *134*, 326-331.

A1.20. Niepmann, D.; Pöttgen, R.; Poduska, K. M.; DiSalvo, F. J.; Trill, H.; Mosel, B. D., *Z. Naturforsch., B: Chem. Sci.* **2001,** *56*, 1-8.

A1.21. Gamza, M.; Schnelle, W.; Slebarski, A.; Burkhardt, U.; Gumeniuk, R.; Rosner, H., *J. Phys.: Condens. Matter* **2008,** *20*, 13.

Appendix A2.[†] Supporting Information for Chapter 2: Probing the Lower Limit of Lattice Thermal Conductivity in an Ordered Extended Solid: $Gd_{117}Co_{56}Sn_{112}$ – A Phonon Glass-Electron Crystal System

A2.1 Supporting Figures

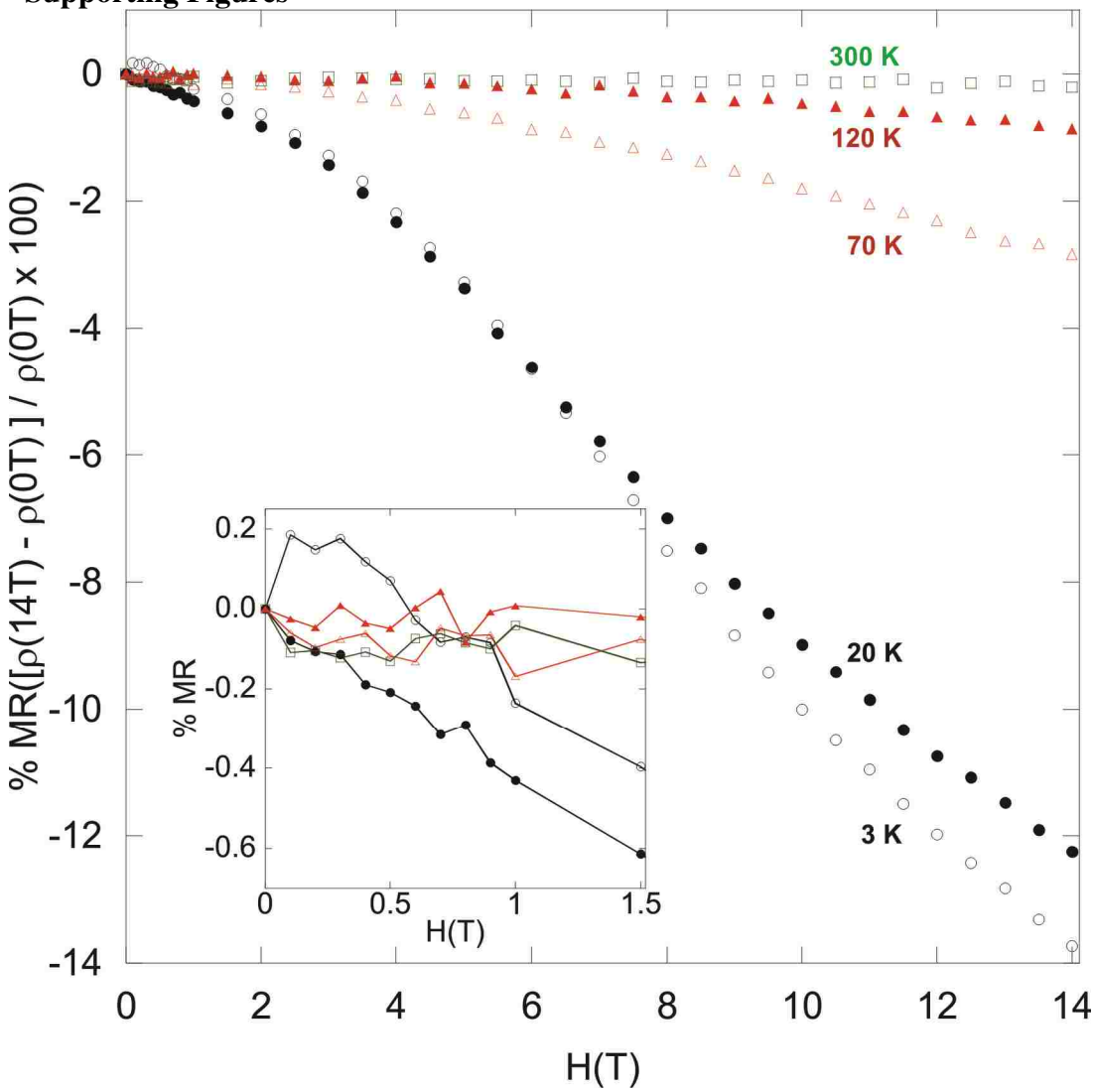

Appendix Figure A2.1. Resistivity as a function of magnetic field (% MR) for $Gd_{117}Co_{56}Sn_{112}$ from 0–14 T at 3, 20, 70, 120, and 300 K. The inset shows % MR from 0–1.5 T.

[†]Reproduced with permission from Schmitt, D. C.; Haldolaarachchige, N.; Xiong, Y. M.;Young, D. P.; Jin, R. Y.; Chan, J. Y., *J. Am. Chem. Soc.* **2012,** *134*, 5965-5973. Copyright 2012 American Chemical Society.

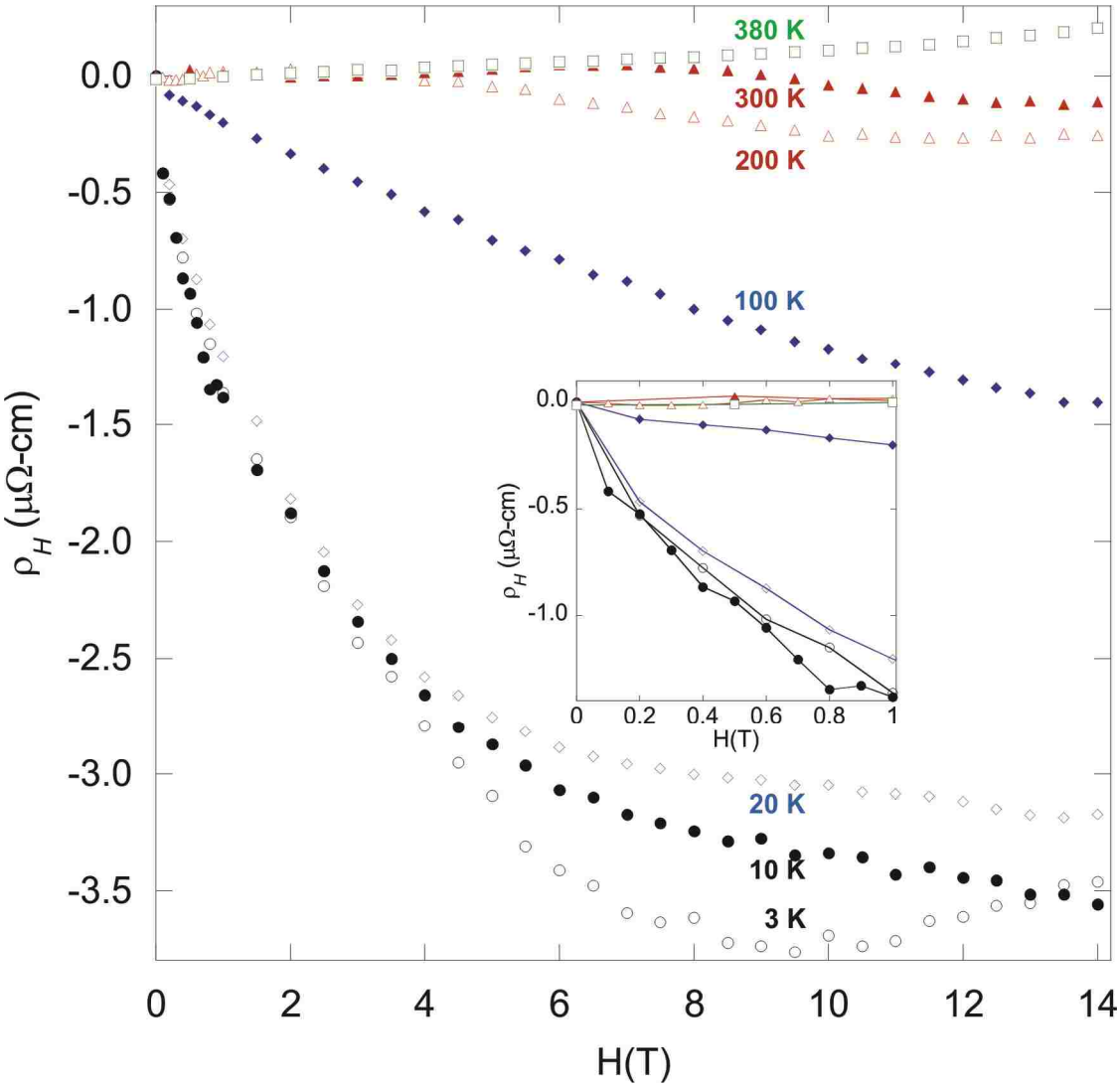

Appendix Figure A2.2. Select Hall resistivity (ρ_H) as a function of magnetic field for $Gd_{117}Co_{56}Sn_{112}$. The inset shows ρ_H as a function of magnetic field from 0–1 T.

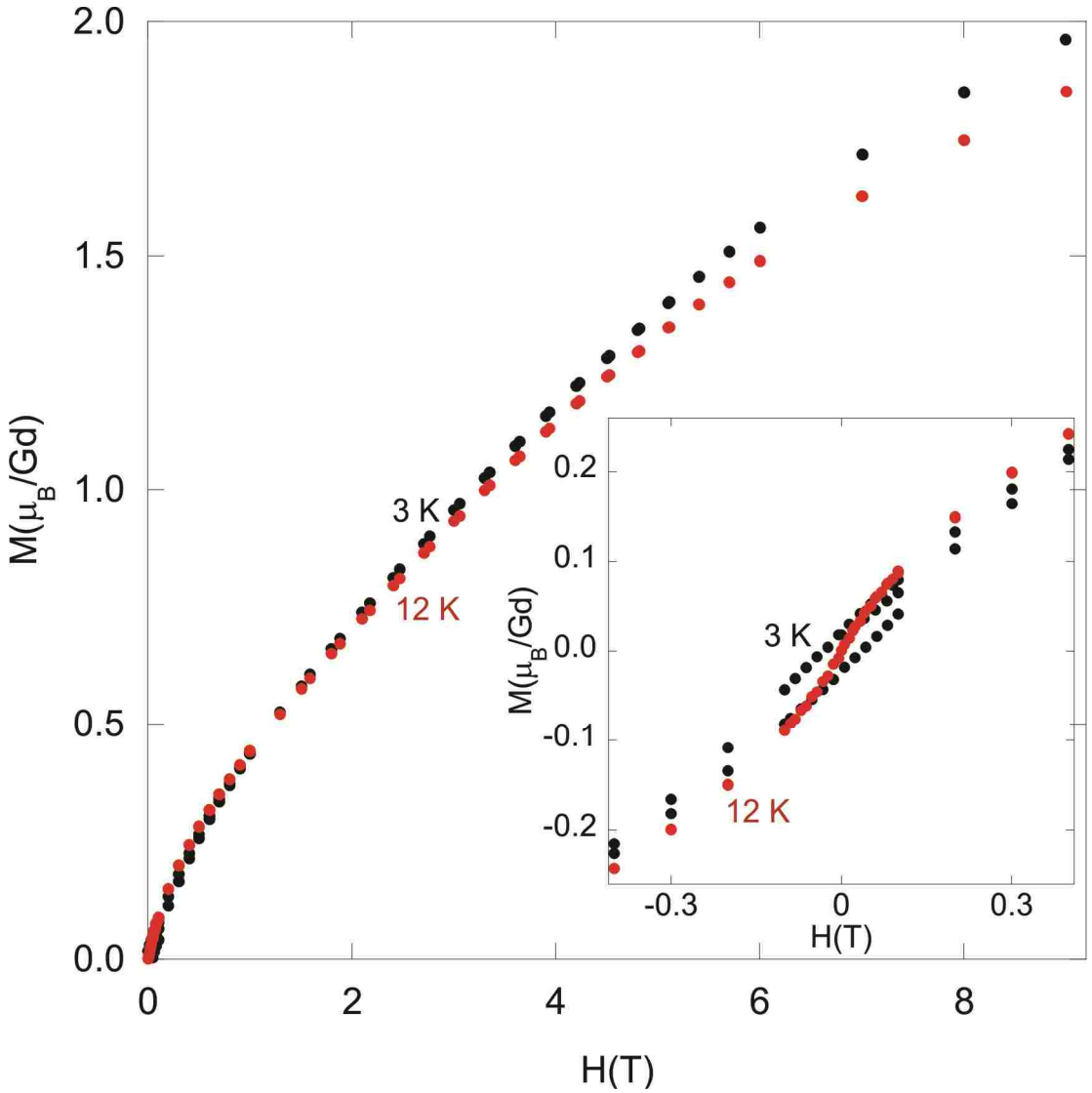

Appendix Figure A2.3. Magnetization (M) as a function of magnetic field (H) for $Gd_{117}Co_{56}Sn_{112}$ at 3 K (black circles) and 12 K red circles). The inset shows M v H from -0.4–0.4 T.

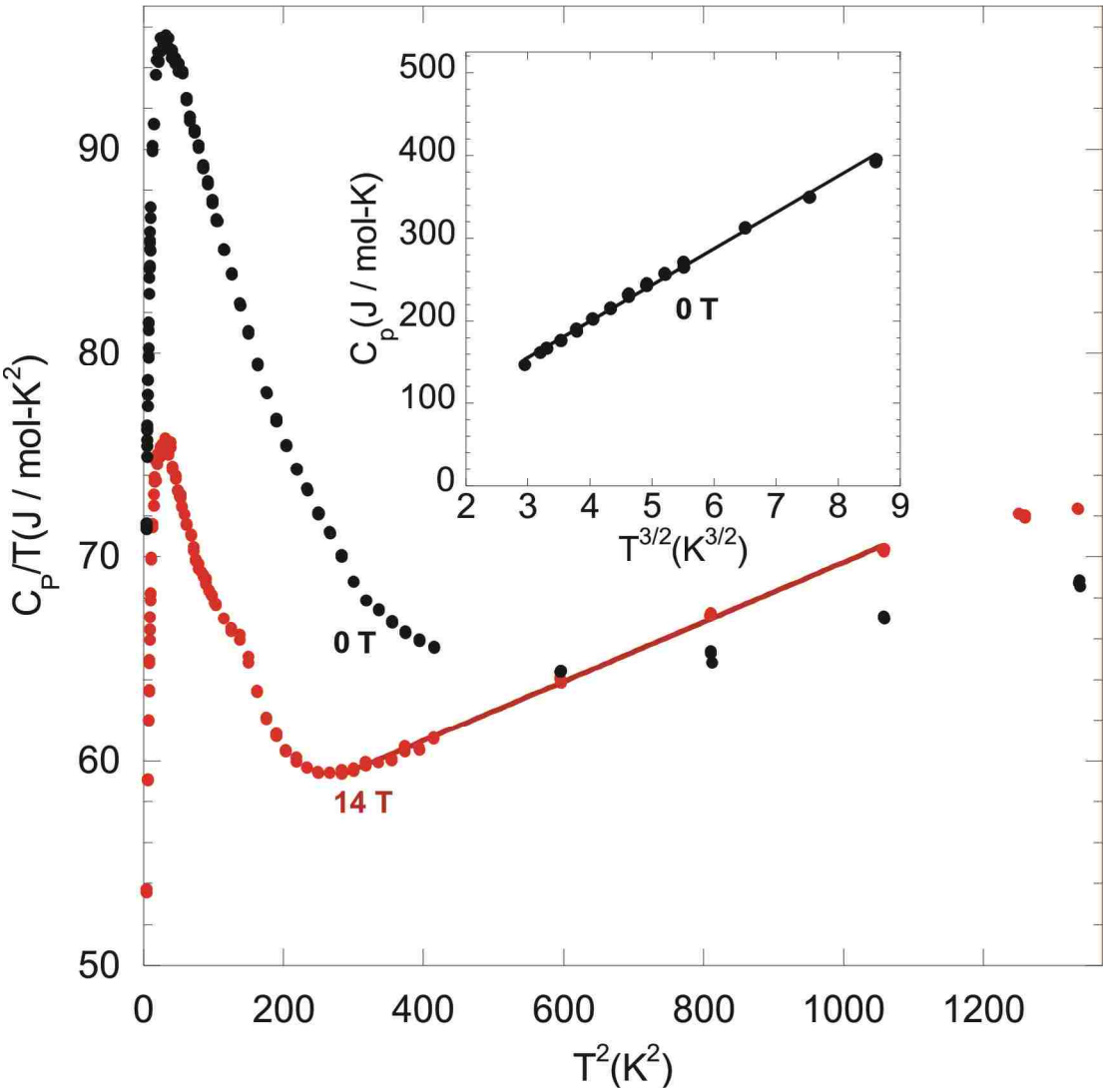

Appendix Figure A2.4. Heat capacity divided by temperature (C_p/T) as a function of temperature squared (T^2) for $Gd_{117}Co_{56}Sn_{112}$ at 0 T (black circles) and 14T (red circles). The red line represents a linear fit from 16–33 K. The inset shows a linear fit of C_p/T v $T^{3/2}$ from 2–5 K.

Appendix A3.[†] Supporting Information for Chapter 3: Structural Complexity Meets Transport and Magnetic Anisotropy in Single Crystalline $Ln_{30}Ru_4Sn_{31}$ (*Ln* = Gd–Dy)

A3.1 Atomic Disorder Refinement

An electron density peak (Q-peak) was found at ~ 2.3 Å from Gd11, which corresponded to a partially occupied (24(1) %) Ru2′ atom; however, the interatomic distance was too close to be considered realistic. Positive and negative Q-peaks were found adjacent to Gd11, suggesting positional disorder. The Gd11 site was found to split between Gd11 (74(2) %) and Gd11′ (26(2) %). The Sn12 site was refined to have a negative Q-peak in close proximity to the site, suggesting partial occupancy (87(1) %) or atomic mixing with a smaller atom (Ru). Site mixing of Ru was chosen for the final refinement due to statistical occupancy similarities (described below) and elemental analysis results. Additionally, the Sn12 (74(3) %) and Ru12′ (26(3) %) mixed site was found to be positionally disordered when atomic positions were allowed to refine freely. The investigation of positive and negative Q-peaks near Sn11, similar to Gd11, also led to site splitting of Sn11 (75(10) %) and Sn11′ (25(10) %) . The trend of positional disorder falls into two groups: **(1)** Gd11 (74(2) %), Sn11 (75(10) %), and Sn12 (74(3) %) and **(2)** Gd11′ (26(2) %), Ru12′ (26(3) %), Sn11′ (25(10) %), and Ru2′ (24(1) %). Figure 1a shows the modeled atomic disorder. The Gd–Ru2′ interatomic distances were 2.256(5) Å and 2.607(7) Å for Gd11 and Gd11′, respectively. Since the occupation difference between Ru2′ and Gd11′ were statistically insignificant and the short Gd11–Ru2′ interatomic distance was chemically unreasonable, the appearance of Gd11′ and Ru2′ were assumed to occur together, and the occupancies of the two atomic positions were linked. Furthermore, the interatomic distances of

[†]Schmitt, D. C.; Haldolaarachchige, N.; Prestigiacomo, J.; Karki, A.; Young, D. P.; Stadler, S.; Jin, R.; Chan, J. Y., *J. Am. Chem. Soc.* **2013,** *135*, 2748-2758.

the similarly occupied Ru12′–Sn11′ (2.76(4) Å), Ru2′–Sn11′ (2.72(3) Å), and Sn11–Sn12 (2.983(9) Å) fall within the range of Ru–Sn (2.57–2.78 Å) and Sn–Sn (2.89–3.14 Å) interatomic distances found in other *A*–Ru–Sn intermetallic compounds.[26-28] The interatomic distances of the non-similarly occupied site Ru12′–Sn11 (2.84(2) Å) falls outside the aforementioned range. Because of the more chemically reasonable interatomic distances and the statistically insignificant deviations in occupancy, the site occupancy factors of all the similarly occupied positions were linked for final refinements.

A3.2 Supporting Details of the Polyhedral Sn1, Sn7, Sn8, and Sn9 Structural Units

The alternating units described in the main text can be viewed as "zig" and "zag" units, which extend infinitely in the *a*-*c* plane. A shorthand $Y(X_1,X_2,\ldots)$, where Y is the atom type and X_x is the atomic site, is used for descriptions of shared polyhedral vertices. The "zig" set is composed of confacial Sn7 polyhedra which are triangular face sharing (× 8) by Gd(5,6,7) atoms with four Sn9 polyhedra in a square planar configuration along the confacial equatorial plane of the two Sn7 polyhedra. These "zig" units are connected along the *c*-direction with edge-sharing Sn9 polyhedra (× 4) by Gd(3,11) atoms from two adjacent "zig" units which form gaps shown in Figure 4f, allowing the Ru–Sn, Sn–Sn framework to penetrate between slabs. The "zag" set is constructed of confacial Sn1 polyhedra which are triangular face sharing (× 4) by Gd(8,8,10) atoms with two sets of axially oriented confacial Sn8 polyhedra. The confacial plane of the Sn1 polyhedral units connects "zag" units in the *c*-direction. The sheets are bridged by the "zag" Sn1 and Sn8 polyhedra. Confacial Sn1 polyhedra link the sheets with triangular face sharing (× 4) by Gd(3,8,10) atom with four Sn9 polyhedra and corner sharing (× 4) by Gd8 atoms with four Sn7 polyhedron. Sn8 confacial polyhedra bridge the sheets with triangular face sharing (× 4) by

Gd(6,8,10) atoms with four Sn9 polyhedra and triangular face sharing (× 2) by Gd(6,8,8) atoms with two sets of Sn7 confacial polyhedra.

A3.3 Supporting Figures

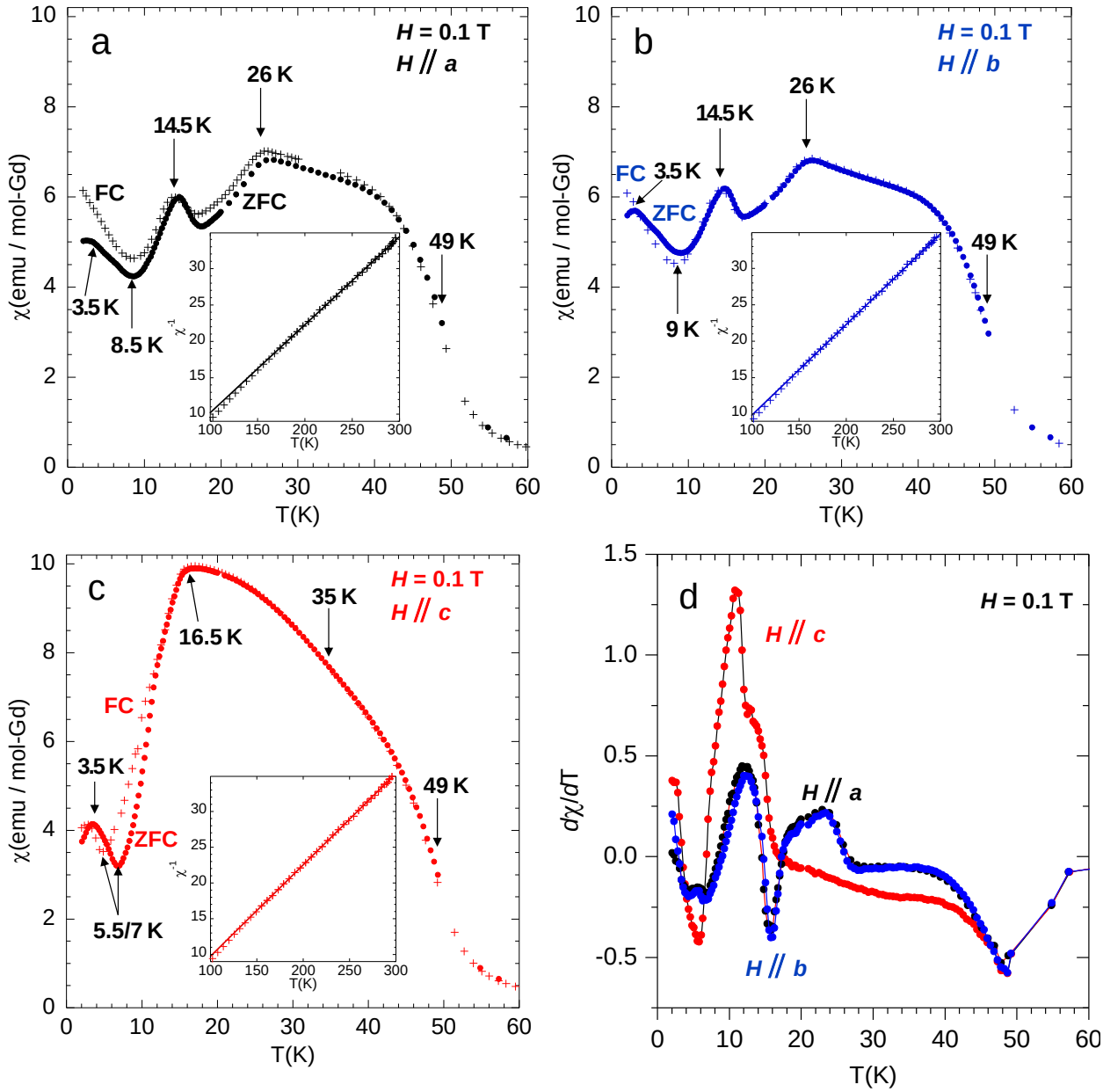

Appendix Figure A3.1. Temperature-dependent ZFC and FC magnetic susceptibility of $Gd_{30}Ru_{4.92}Sn_{30.54}$ from 2–70 K in an applied field of 0.1 T with (**a**) H //a, (**b**) H //b, and (**c**) H //c. Arrows show the magnetic transition temperatures, and insets show inverse susceptibility plots with extrapolated linear fits from the modified Curie-Weiss fit regions. (**d**) shows the temperature-dependent derivative of the ZFC magnetic susceptibility with H //a, b, and c.

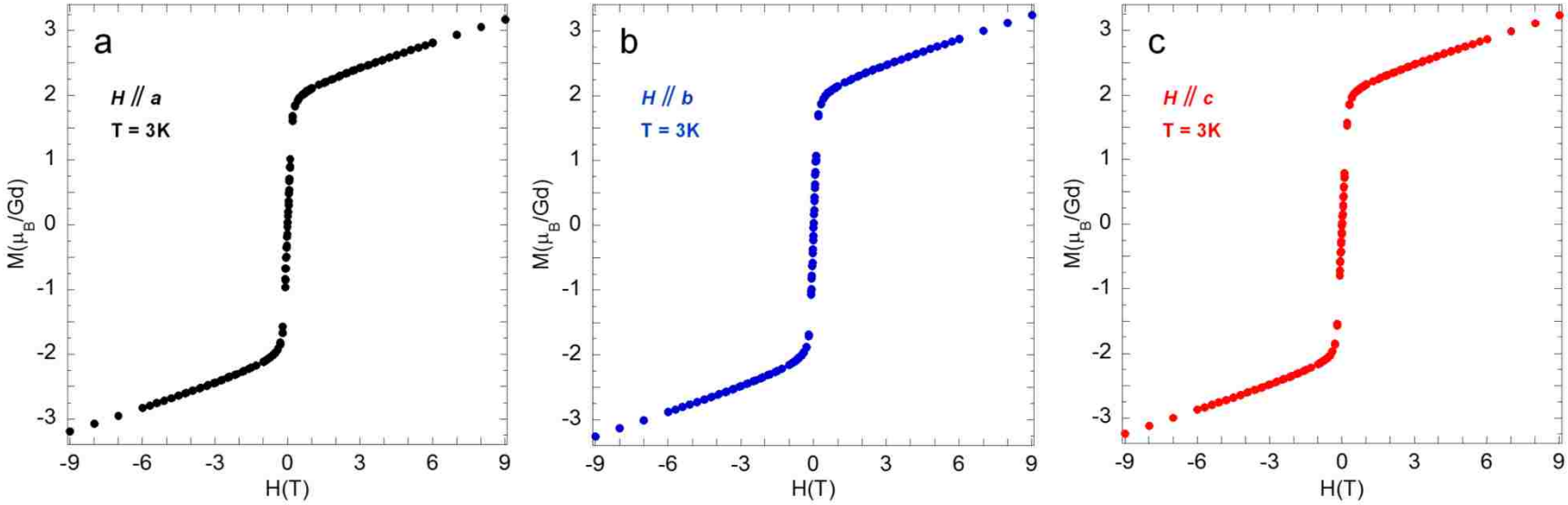

Appendix Figure A3.2. Field-dependent magnetization of $Gd_{30}Ru_{4.92}Sn_{30.54}$ at 3 K in applied fields up to 9 T with (**a**) H //a, (**b**) H //b, and (**c**) H //c shown in black, blue, and red, respectively.

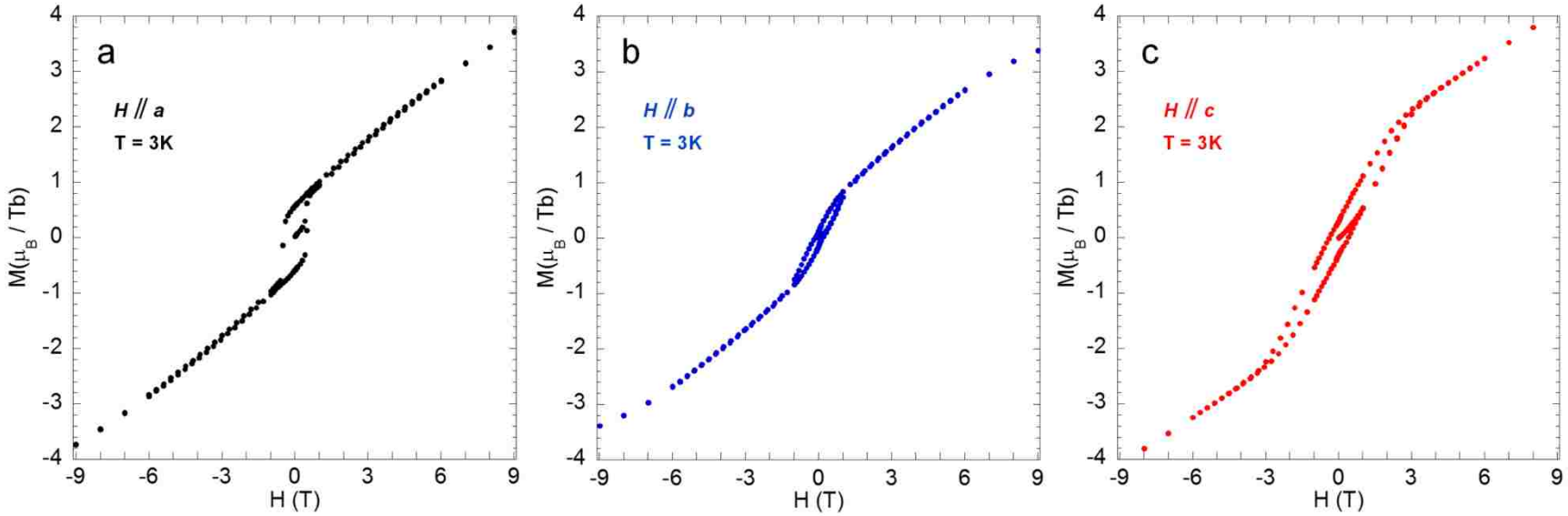

Appendix Figure A3.3. Field-dependent magnetization of $Tb_{30}Ru_6Sn_{29.5}$ at 3 K in applied fields up to 9 T with (**a**) H //a, (**b**) H //b, and (**c**) H //c shown in black, blue, and red, respectively.

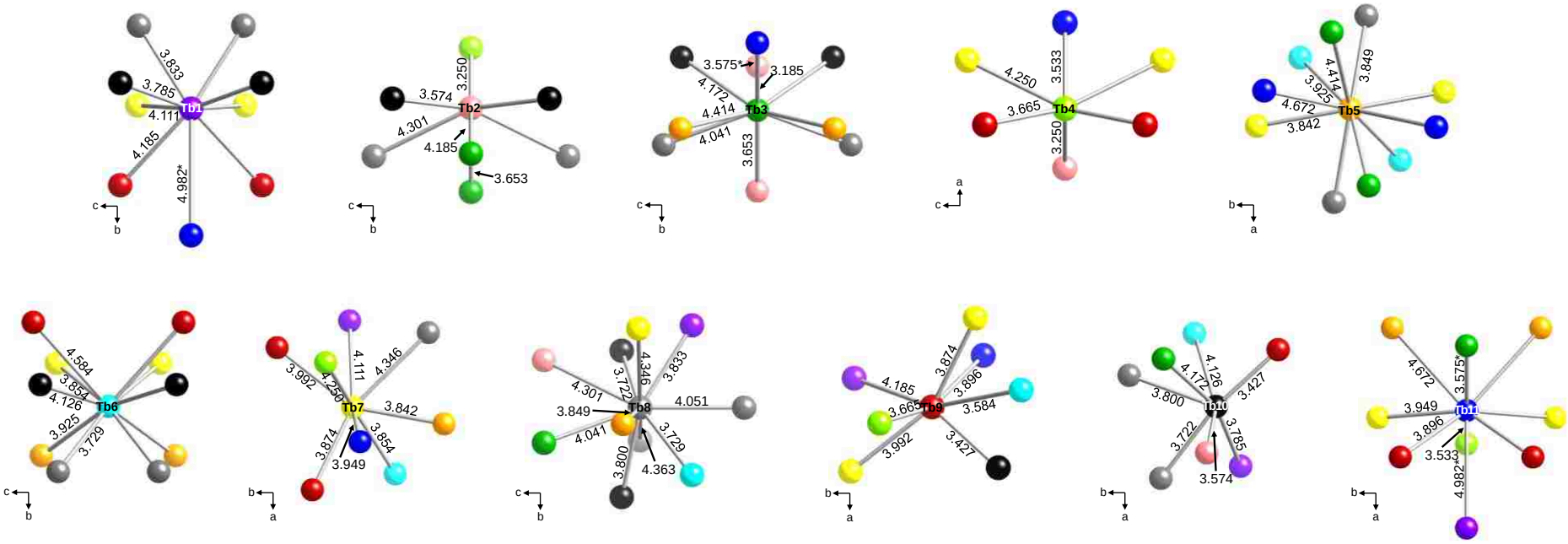

Appendix Figure A3.4. Tb1–Tb11 environments, showing Tb–Tb interatomic distances < 5 Å. Ru and Sn atoms are omitted for clarity.

A3.4 Supporting Tables

Appendix Table A3.1a. Positions, occupancies, and atomic displacement parameters for $Tb_{30}Ru_6Sn_{29.5}$

Atom	Site	*x*	*y*	*z*	Occ.	U_{eq} (Å^2) [a]
Tb1	4*g*	0.13793(4)	0.658250(17)	0	1	0.01038(8)
Tb2	4*g*	0.59003(3)	0.898000(17)	0	1	0.00943(8)
Tb3	4*g*	0.26482(3)	0.969769(17)	0	1	0.00933(8)
Tb4	4*g*	0.78423(4)	0.801697(17)	0	1	0.01106(9)
Tb5	4*e*	0	0	0.26695(3)	1	0.00881(8)
Tb6	4*g*	0.32487(4)	0.418402(18)	0	1	0.01350(9)
Tb7	8*h*	0.44070(2)	0.652902(12)	0.81881(3)	1	0.00996(6)
Tb8	8*h*	0.82086(2)	0.473606(12)	0.17554(2)	1	0.00891(6)
Tb9	8*h*	0.73165(3)	0.720418(12)	0.26150(3)	1	0.01129(6)
Tb10	8*h*	0.42996(2)	0.882974(12)	0.26191(3)	1	0.01087(6)
Tb11	4*g*	0.93699(9)	0.14084(5)	0	0.765(3)	0.01297(19)
Tb11'	4*g*	0.9344(4)	0.12428(15)	0	0.235(3)	0.01297(19)
Ru1	8*h*	0.51232(4)	0.78732(2)	0.12516(4)	1	0.00900(9)
Ru2'	4*g*	0.1275(3)	0.77376(12)	0	0.235(3)	0.0124(9)
Sn1	4*f*	0	0.5	0.36319(5)	1	0.00890(11)
Sn2	2*a*	0	0	0	1	0.01467(18)
Sn3	4*g*	0.35208(5)	0.84930(2)	0	1	0.01144(12)
Sn4	8*h*	0.83766(3)	0.921609(17)	0.12585(3)	1	0.00909(8)
Sn5	4*g*	0.34328(5)	0.73545(2)	0	1	0.01103(12)
Sn6	4*g*	0.61468(6)	0.70589(2)	0	1	0.01251(12)
Sn7	4*g*	0.62056(5)	0.44425(2)	0	1	0.01033(11)
Sn8	4*g*	0.95719(5)	0.55853(3)	0	1	0.01203(12)
Sn9	8*h*	0.67441(4)	0.591628(17)	0.26484(4)	1	0.01041(8)
Sn10	8*h*	0.67872(3)	0.844945(16)	0.23586(3)	1	0.00818(8)
Sn11	8*h*	0.9817(3)	0.74805(12)	0.8477(3)	0.765(3)	0.0100(3)
Sn11'	8*h*	0.9736(11)	0.7415(5)	0.8394(12)	0.235(3)	0.0100(3)
Sn12'	4*g*	0.85907(6)	0.67606(3)	0	0.235(3)	0.01065(13)
Ru12	4*g*	0.85907(6)	0.67606(3)	0	0.765(3)	0.01065(13)

[a] U_{eq} is defined as 1/3 of the trace of the orthogonalized U_{ij} tensor.

´Positional and/or occupational disorder of Tb11, Sn11, and Ru12 with Tb11′, Sn11′, and Sn12′, respectively. Ru2′ occurs at the same frequency as the disordered atoms.

Appendix Table A3.1b. Positions, occupancies, and atomic displacement parameters for $Dy_{30}Ru_{4.57}Sn_{30.72}$

Atom	Site	*x*	*y*	*z*	Occ.	U_{eq} (Å^2) [a]
Dy1	4*g*	0.13966(5)	0.65820(2)	0	1	0.01032(12)
Dy2	4*g*	0.58950(5)	0.89952(2)	0	1	0.00984(11)
Dy3	4*g*	0.26454(5)	0.96973(2)	0	1	0.00956(11)
Dy4	4*g*	0.78056(5)	0.80377(2)	0	1	0.01091(12)
Dy5	4*e*	0	0	0.26642(5)	1	0.00920(11)
Dy6	4*g*	0.32926(5)	0.41950(2)	0	1	0.01168(12)
Dy7	8*h*	0.43876(3)	0.652200(16)	0.81957(3)	1	0.01029(9)
Dy8	8*h*	0.82077(3)	0.474047(16)	0.17489(3)	1	0.00974(8)
Dy9	8*h*	0.73531(3)	0.720583(16)	0.25956(3)	1	0.01150(9)
Dy10	8*h*	0.43038(3)	0.884754(16)	0.25933(3)	1	0.00941(8)
Dy11	4*g*	0.93590(10)	0.14039(6)	0	0.858(4)	0.0123(2)
Dy11'	4*g*	0.9337(8)	0.1243(3)	0	0.142(4)	0.0123(2)
Ru1	8*h*	0.50942(6)	0.78866(3)	0.12626(6)	1	0.00937(13)
Ru2'	4*g*	0.1327(6)	0.7747(3)	0	0.142(4)	0.0089(19)
Sn1	4*f*	0	0.5	0.36117(7)	1	0.00929(15)
Sn2	2*a*	0	0	0	1	0.0122(2)
Sn3	4*g*	0.35143(7)	0.85057(3)	0	1	0.01095(17)
Sn4	8*h*	0.83729(5)	0.92181(2)	0.12630(5)	1	0.00947(11)
Sn5	4*g*	0.34128(7)	0.73608(3)	0	1	0.01109(17)
Sn6	4*g*	0.60542(7)	0.70708(3)	0	1	0.00976(16)
Sn7	4*g*	0.62087(7)	0.44478(3)	0	1	0.01059(16)
Sn8	4*g*	0.95902(7)	0.55662(3)	0	1	0.01022(16)
Sn9	8*h*	0.67345(5)	0.59240(2)	0.26343(5)	1	0.01059(12)
Sn10	8*h*	0.67730(5)	0.84531(2)	0.23683(5)	1	0.00861(11)
Sn11	8*h*	0.9851(4)	0.74859(18)	0.8467(4)	0.858(4)	0.0100(4)
Sn11'	8*h*	0.982(3)	0.7536(12)	0.836(2)	0.142(4)	0.0100(4)
Sn12	4*g*	0.8532(6)	0.6762(3)	0	0.858(4)	0.0103(6)
Ru12'	4*g*	0.864(5)	0.681(2)	0	0.142(4)	0.0103(6)

[a] U_{eq} is defined as 1/3 of the trace of the orthogonalized U_{ij} tensor.

´Positional and/or occupational disorder of Dy11, Sn11, and Sn12 with Dy11′, Sn11′, and Ru12′, respectively. Ru2′ occurs at the same frequency as the disordered atoms.

Appendix A4. Consent Policies

A4.1 American Chemical Society (Blanket Approval for Chapters 2 and 3)

American Chemical Society's Policy on Theses and Dissertations

If your university requires you to obtain permission, you must use the RightsLink permission system. See RightsLink instructions at http://pubs.acs.org/page/copyright/permissions.html.

This is regarding request for permission to include **your** paper(s) or portions of text from **your** paper(s) in your thesis. Permission is now automatically granted; please pay special attention to the **implications** paragraph below. The Copyright Subcommittee of the Joint Board/Council Committees on Publications approved the following:

> Copyright permission for published and submitted material from theses and dissertations
> ACS extends blanket permission to students to include in their theses and dissertations their own articles, or portions thereof, that have been published in ACS journals or submitted to ACS journals for publication, provided that the ACS copyright credit line is noted on the appropriate page(s).
>
> Publishing **implications** of electronic publication of theses and dissertation material
> Students and their mentors should be aware that posting of theses and dissertation material on the Web prior to submission of material from that thesis or dissertation to an ACS journal may affect publication in that journal. Whether Web posting is considered prior publication may be evaluated on a case-by-case basis by the journal's editor. If an ACS journal editor considers Web posting to be "prior publication", the paper will not be accepted for publication in that journal. If you intend to submit your unpublished paper to ACS for publication, check with the appropriate editor prior to posting your manuscript electronically.

Reuse/Republication of the Entire Work in Theses or Collections: Authors may reuse all or part of the Submitted, Accepted or Published Work in a thesis or dissertation that the author writes and is required to submit to satisfy the criteria of degree-granting institutions. Such reuse is permitted subject to the ACS' "Ethical Guidelines to Publication of Chemical Research" (http://pubs.acs.org/page/policy/ethics/index.html); the author should secure written confirmation (via letter or email) from the respective ACS journal editor(s) to avoid potential conflicts with journal prior publication*/embargo policies. Appropriate citation of the Published Work must be made. If the thesis or dissertation to be published is in electronic format, a direct link to the Published Work must also be included using the ACS Articles on Request author-directed link – see http://pubs.acs.org/page/policy/articlesonrequest/index.html

* Prior publication policies of ACS journals are posted on the ACS website at
http://pubs.acs.org/page/policy/prior/index.html

If your paper has **not** yet been published by ACS, please print the following credit line on the first page of your article: "Reproduced (or 'Reproduced in part') with permission from [JOURNAL NAME], in press (or 'submitted for publication'). Unpublished work copyright [CURRENT YEAR] American Chemical Society." Include appropriate information.

If your paper has already been published by ACS and you want to include the text or portions of the text in your thesis/dissertation, please print the ACS copyright credit line on the first page of your article: "Reproduced (or 'Reproduced in part') with permission from [FULL REFERENCE CITATION.] Copyright [YEAR] American Chemical Society." Include appropriate information.

Submission to a Dissertation Distributor: If you plan to submit your thesis to UMI or to another dissertation distributor, you should not include the unpublished ACS paper in your thesis if the thesis will be disseminated electronically, until ACS has published your paper. After publication of the paper by ACS, you may release the entire thesis (**not the individual ACS article by itself**) for electronic dissemination through the distributor; ACS's copyright credit line should be printed on the first page of the ACS paper.

10/10/03, 01/15/04, 06/07/06, 04/07/10, 08/24/10, 02/28/11

A4.2 Zeitschrift Für Anorganische und Allgemeine Chemie

JOHN WILEY AND SONS LICENSE TERMS AND CONDITIONS

Feb 20, 2013

This is a License Agreement between Devin C Schmitt ("You") and John Wiley and Sons ("John Wiley and Sons") provided by Copyright Clearance Center ("CCC"). The license consists of your order details, the terms and conditions provided by John Wiley and Sons, and the payment terms and conditions.

All payments must be made in full to CCC. For payment instructions, please see information listed at the bottom of this form.

License Number	3093100090447
License date	Feb 20, 2013
Licensed content publisher	John Wiley and Sons
Licensed content publication	Zeitschrift für anorganische und allgemeine Chemie
Licensed content title	Crystal Structure and Physical Properties of Yb3Co4−xRuxSn13 (x = 0, 0.38)
Licensed copyright line	Copyright © 2011 WILEY-VCH Verlag GmbH & Co. KGaA, Weinheim
Licensed content author	Devin C. Schmitt,Neel Haldolaarachchige,David P. Young,Rongying Jin,Julia Y. Chan
Licensed content date	Oct 19, 2011
Start page	2046
End page	2051
Type of use	Dissertation/Thesis
Requestor type	Author of this Wiley article
Format	Print and electronic
Portion	Full article
Will you be translating?	No
Total	0.00 USD
Terms and Conditions	

TERMS AND CONDITIONS

This copyrighted material is owned by or exclusively licensed to John Wiley & Sons, Inc. or one of its group companies (each a "Wiley Company") or a society for whom a Wiley Company has exclusive publishing rights in relation to a particular journal (collectively WILEY"). By clicking "accept" in connection with completing this licensing transaction, you agree that the following terms and conditions apply to this transaction (along with the billing and payment terms and conditions established by the Copyright Clearance Center Inc., ("CCC's Billing and Payment terms and conditions"), at the time that you opened your Rightslink account (these are available at any time at http://myaccount.copyright.com)

Terms and Conditions

1. The materials you have requested permission to reproduce (the "Materials") are protected by copyright.

2. You are hereby granted a personal, non-exclusive, non-sublicensable, non-transferable, worldwide, limited license to reproduce the Materials for the purpose specified in the licensing process. This license is for a one-time use only with a maximum distribution equal to the number that you identified in the licensing process. Any form of republication granted by this licence must be completed within two years of the date of the grant of this licence (although copies prepared before may be distributed thereafter). The Materials shall not be used in any other manner or for any other purpose. Permission is granted subject to an appropriate acknowledgement given to the author, title of the material/book/journal and the publisher. You shall also duplicate the copyright notice that appears in the Wiley publication in your use of the Material. Permission is also granted on the understanding that nowhere in the text is a previously published source acknowledged for all or part of this Material. Any third party material is expressly excluded from this permission.

3. With respect to the Materials, all rights are reserved. Except as expressly granted by the terms of the license, no part of the Materials may be copied, modified, adapted (except for minor reformatting required by the new Publication), translated, reproduced, transferred or distributed, in any form or by any means, and no derivative works may be made based on the Materials without the prior permission of the respective copyright owner. You may not alter, remove or suppress in any manner any copyright, trademark or other notices displayed by the Materials. You may not license, rent, sell, loan, lease, pledge, offer as security, transfer or assign the Materials, or any of the rights granted to you hereunder to any other person.

4. The Materials and all of the intellectual property rights therein shall at all times remain the exclusive property of John Wiley & Sons Inc or one of its related companies (WILEY) or their respective licensors, and your interest therein is only that of having possession of and the right to reproduce the Materials pursuant to Section 2 herein during the continuance of this Agreement. You agree that you own no right, title or interest in or to the Materials or any of the intellectual property rights therein. You shall have no rights hereunder other than the license as provided for above in Section 2. No right, license or interest to any trademark, trade name, service mark or other branding ("Marks") of WILEY or its licensors is granted hereunder, and you agree that you shall not assert any such right, license or interest with respect thereto.

5. NEITHER WILEY NOR ITS LICENSORS MAKES ANY WARRANTY OR REPRESENTATION OF ANY KIND TO YOU OR ANY THIRD PARTY, EXPRESS, IMPLIED OR STATUTORY, WITH RESPECT TO THE MATERIALS OR THE ACCURACY OF ANY INFORMATION CONTAINED IN THE MATERIALS, INCLUDING, WITHOUT LIMITATION, ANY IMPLIED WARRANTY OF MERCHANTABILITY, ACCURACY, SATISFACTORY QUALITY, FITNESS FOR A PARTICULAR PURPOSE, USABILITY, INTEGRATION OR NON-INFRINGEMENT AND ALL SUCH WARRANTIES ARE HEREBY EXCLUDED BY WILEY AND ITS LICENSORS AND WAIVED BY YOU.

6. WILEY shall have the right to terminate this Agreement immediately upon breach of this Agreement by you.

7. You shall indemnify, defend and hold harmless WILEY, its Licensors and their respective directors, officers, agents and employees, from and against any actual or threatened claims, demands, causes of action or proceedings arising from any breach of this Agreement by you.

8. IN NO EVENT SHALL WILEY OR ITS LICENSORS BE LIABLE TO YOU OR ANY OTHER PARTY OR ANY OTHER PERSON OR ENTITY FOR ANY SPECIAL, CONSEQUENTIAL, INCIDENTAL, INDIRECT, EXEMPLARY OR PUNITIVE DAMAGES, HOWEVER CAUSED, ARISING OUT OF OR IN CONNECTION WITH THE DOWNLOADING, PROVISIONING, VIEWING OR USE OF THE MATERIALS REGARDLESS OF THE FORM OF ACTION, WHETHER FOR BREACH OF CONTRACT, BREACH OF WARRANTY, TORT, NEGLIGENCE, INFRINGEMENT OR OTHERWISE (INCLUDING, WITHOUT LIMITATION, DAMAGES BASED ON LOSS OF PROFITS, DATA, FILES, USE, BUSINESS OPPORTUNITY OR CLAIMS OF THIRD PARTIES), AND WHETHER OR NOT THE PARTY HAS BEEN ADVISED OF THE POSSIBILITY OF SUCH DAMAGES. THIS LIMITATION SHALL APPLY NOTWITHSTANDING ANY FAILURE OF ESSENTIAL PURPOSE OF ANY LIMITED REMEDY PROVIDED HEREIN.

9. Should any provision of this Agreement be held by a court of competent jurisdiction to be illegal, invalid, or unenforceable, that provision shall be deemed amended to achieve as nearly

as possible the same economic effect as the original provision, and the legality, validity and enforceability of the remaining provisions of this Agreement shall not be affected or impaired thereby.

10. The failure of either party to enforce any term or condition of this Agreement shall not constitute a waiver of either party's right to enforce each and every term and condition of this Agreement. No breach under this agreement shall be deemed waived or excused by either party unless such waiver or consent is in writing signed by the party granting such waiver or consent. The waiver by or consent of a party to a breach of any provision of this Agreement shall not operate or be construed as a waiver of or consent to any other or subsequent breach by such other party.

11. This Agreement may not be assigned (including by operation of law or otherwise) by you without WILEY's prior written consent.

12. Any fee required for this permission shall be non-refundable after thirty (30) days from receipt.

13. These terms and conditions together with CCC's Billing and Payment terms and conditions (which are incorporated herein) form the entire agreement between you and WILEY concerning this licensing transaction and (in the absence of fraud) supersedes all prior agreements and representations of the parties, oral or written. This Agreement may not be amended except in writing signed by both parties. This Agreement shall be binding upon and inure to the benefit of the parties' successors, legal representatives, and authorized assigns.

14. In the event of any conflict between your obligations established by these terms and conditions and those established by CCC's Billing and Payment terms and conditions, these terms and conditions shall prevail.

15. WILEY expressly reserves all rights not specifically granted in the combination of (i) the license details provided by you and accepted in the course of this licensing transaction, (ii) these terms and conditions and (iii) CCC's Billing and Payment terms and conditions.

16. This Agreement will be void if the Type of Use, Format, Circulation, or Requestor Type was misrepresented during the licensing process.

17. This Agreement shall be governed by and construed in accordance with the laws of the State of New York, USA, without regards to such state's conflict of law rules. Any legal action, suit or proceeding arising out of or relating to these Terms and Conditions or the breach thereof shall be instituted in a court of competent jurisdiction in New York County in the State of New York in the United States of America and each party hereby consents and submits to the personal jurisdiction of such court, waives any objection to venue in such court and consents to service of process by registered or certified mail, return receipt requested, at the last known address of such party.

Wiley Open Access Terms and Conditions

All research articles published in Wiley Open Access journals are fully open access: immediately freely available to read, download and share. Articles are published under the terms of the Creative Commons Attribution Non Commercial License. which permits use, distribution and reproduction in any medium, provided the original work is properly cited and is not used for commercial purposes. The license is subject to the Wiley Open Access terms and conditions:
Wiley Open Access articles are protected by copyright and are posted to repositories and websites in accordance with the terms of the Creative Commons Attribution Non Commercial License. At the time of deposit, Wiley Open Access articles include all changes made during peer review, copyediting, and publishing. Repositories and websites that host the article are responsible for incorporating any publisher-supplied amendments or retractions issued subsequently.
Wiley Open Access articles are also available without charge on Wiley's publishing platform, **Wiley Online Library** or any successor sites.

Use by non-commercial users

For non-commercial and non-promotional purposes individual users may access, download,

copy, display and redistribute to colleagues Wiley Open Access articles, as well as adapt, translate, text- and data-mine the content subject to the following conditions:

- The authors' moral rights are not compromised. These rights include the right of "paternity" (also known as "attribution" - the right for the author to be identified as such) and "integrity" (the right for the author not to have the work altered in such a way that the author's reputation or integrity may be impugned).
- Where content in the article is identified as belonging to a third party, it is the obligation of the user to ensure that any reuse complies with the copyright policies of the owner of that content.
- If article content is copied, downloaded or otherwise reused for non-commercial research and education purposes, a link to the appropriate bibliographic citation (authors, journal, article title, volume, issue, page numbers, DOI and the link to the definitive published version on Wiley Online Library) should be maintained. Copyright notices and disclaimers must not be deleted.
- Any translations, for which a prior translation agreement with Wiley has not been agreed, must prominently display the statement: "This is an unofficial translation of an article that appeared in a Wiley publication. The publisher has not endorsed this translation."

Use by commercial "for-profit" organisations

Use of Wiley Open Access articles for commercial, promotional, or marketing purposes requires further explicit permission from Wiley and will be subject to a fee. Commercial purposes include:

- Copying or downloading of articles, or linking to such articles for further redistribution, sale or licensing;
- Copying, downloading or posting by a site or service that incorporates advertising with such content;
- The inclusion or incorporation of article content in other works or services (other than normal quotations with an appropriate citation) that is then available for sale or licensing, for a fee (for example, a compilation produced for marketing purposes, inclusion in a sales pack)
- Use of article content (other than normal quotations with appropriate citation) by for-profit organisations for promotional purposes
- Linking to article content in e-mails redistributed for promotional, marketing or educational purposes;
- Use for the purposes of monetary reward by means of sale, resale, licence, loan, transfer or other form of commercial exploitation such as marketing products
- Print reprints of Wiley Open Access articles can be purchased from: corporatesales@wiley.com

Other Terms and Conditions:

BY CLICKING ON THE "I AGREE..." BOX, YOU ACKNOWLEDGE THAT YOU HAVE READ AND FULLY UNDERSTAND EACH OF THE SECTIONS OF AND PROVISIONS SET FORTH IN THIS AGREEMENT AND THAT YOU ARE IN AGREEMENT WITH AND ARE WILLING TO ACCEPT ALL OF YOUR OBLIGATIONS AS SET FORTH IN THIS AGREEMENT.

v1.7

If you would like to pay for this license now, please remit this license along with your payment made payable to "COPYRIGHT CLEARANCE CENTER" otherwise you will be invoiced within 48 hours of the license date. Payment should be in the form of a check or money order referencing your account number and this invoice number RLNK500960969. Once you receive your invoice for this order, you may pay your invoice by credit card. Please follow instructions provided at that time.

Make Payment To:
Copyright Clearance Center
Dept 001
P.O. Box 843006
Boston, MA 02284-3006

For suggestions or comments regarding this order, contact RightsLink Customer Support: customercare@copyright.com or +1-877-622-5543 (toll free in the US) or +1-978-646-2777.

Gratis licenses (referencing $0 in the Total field) are free. Please retain this printable license for your reference. No payment is required.

VITA

Devin Schmitt received a bachelor of science in physics from Louisiana State University in May 2006. While completing his bachelor's degree from 2004–2006, he worked full-time as an IT analyst intern at the LSU Department of Experimental Statistics and the LSU Student Health Center. After graduating in 2006, Devin accepted a full-time position at the LSU Student Health Center as an IT analyst.

In 2008, Devin decided to pursue a Doctor of Philosophy of Chemistry under the guidance of Professor Julia Chan. He will be receiving his Doctor of Philosophy from Louisiana State University in May 2013.